

AD-A267 907

AFOSR-TR- 93 0099

2



ASPECTS OF HIGH TEMPERATURE DAMAGE IN FIBER REINFORCED TITANIUM METAL MATRIX COMPOSITES

DTIC
S **ELECTE** **D**
AUG 16 1993
C

Annual Report
July 1993

By

H. Ghonem, D. Zheng, et al

Department of Mechanical Engineering
University of Rhode Island
Kingston, RI 02881-0805

DISTRIBUTION STATEMENT A

Approved for public release
Distribution Unlimited

Prepared for

Department of Air Force
Air Force Office of Scientific Research
Bolling Air Force Base, DC 20332-6448

Grant AFOSR-92-F49620

AFOSR-TR-93-0099

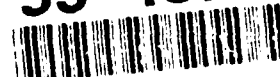
93

8

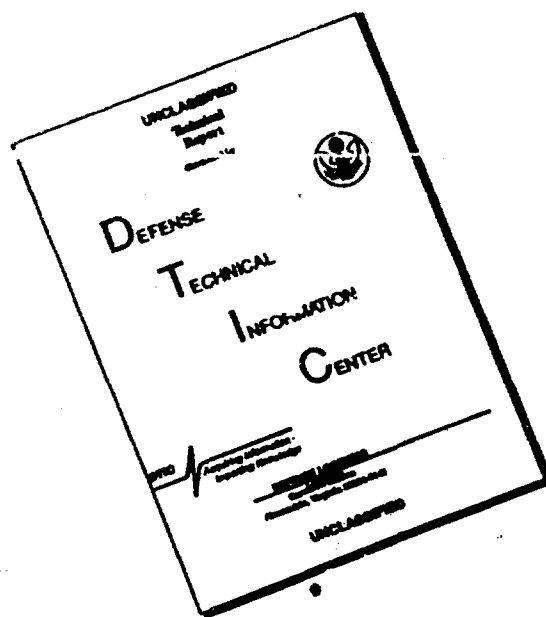
17

93 6

93-18793



DISCLAIMER NOTICE



THIS DOCUMENT IS BEST QUALITY AVAILABLE. THE COPY FURNISHED TO DTIC CONTAINED A SIGNIFICANT NUMBER OF PAGES WHICH DO NOT REPRODUCE LEGIBLY.

REPORT DOCUMENTATION PAGE

Form Approved
OMB No. 0704-0188

Public reporting burden for this collection of information is estimated to average 1 hour per response, including the time for reviewing instructions, searching existing data sources, gathering and maintaining the data needed, and completing and reviewing the collection of information. Send comments regarding this burden estimate or any other aspect of this collection of information, including suggestions for reducing this burden, to Washington Headquarters Services, Directorate for Information Operations and Reports, 1215 Jefferson Davis Highway, Suite 1204, Arlington, VA 22202-4302, and to the Office of Management and Budget, Paperwork Reduction Project (0704-0188), Washington, DC 20503.

1. AGENCY USE ONLY (Leave blank)		2. REPORT DATE July 1993		3. REPORT TYPE AND DATES COVERED Annual, June 92 - June 93	
4. TITLE AND SUBTITLE Aspects of High Temperature Damage in Fiber Reinforced Titanium Metal Matrix Composites (u)				5. FUNDING NUMBERS AFOSR-92-F49620 AFOSR-FR-93-0599 AFOSR-JF-93-0599	
6. AUTHOR(S) H. Ghonem, ¹ D. Zheng ¹ , M. Tamin ¹ , Y Win ¹ M. Thompson ² , J. Beals ² , and G. Linsey ²					
7. PERFORMING ORGANIZATION NAME(S) AND ADDRESS(ES) 1. University of Rhode Island, Kingston, R.I. 02881 2. United Technologies, East Hartford, CT 06108				8. PERFORMING ORGANIZATION REPORT NUMBER URI-MSL-93-10	
9. SPONSORING/MONITORING AGENCY NAME(S) AND ADDRESS(ES) USAF Office of Scientific Research Bolling Air Force Base Washington, DC 20332-6448 NH				10. SPONSORING/MONITORING AGENCY REPORT NUMBER	
11. SUPPLEMENTARY NOTES Dr. W. Jones, Program Manager					
12a. DISTRIBUTION / AVAILABILITY STATEMENT Approved for public release/distribution is unlimited				12b. DISTRIBUTION CODE	
13. ABSTRACT (Maximum 200 words) Aspects associated with high temperature damage in fiber reinforced Metal Matrix Composites were investigated and are presented in this report in the form of five separate sections. In the first section, the fatigue and fatigue crack growth characteristics in neat laminates made of Timetal 21S were studied in relation to both temperature and loading frequency effects. The second section deals with the evolution of the thermal residual stresses in the composite when cooling from consolidation temperature or subjecting the composite to thermal cycles. A new mechanical simulation method capable of measuring the induced residual stress on real time basis has been developed in this study. The third section extends this issue to the time-dependent internal stress and strain states of MMCs under the thermomechanical loading conditions. Here, a new micromechanical model employing the four-phase concentric cylinder configuration has been proposed. Based on this model, the time-dependent behavior of continuous fiber reinforced metal matrix composites has been evaluated for the SCS-6/Timetal 21S composite. These results are presented in the fourth section. The last section of this report deals with the high temperature fatigue crack growth characteristics of the continuous fiber reinforced titanium metal matrix composite σ 1240/Timetal 121S. The time-dependent features of the crack growth was examined in relation to the variation of both testing temperature and loading frequency. The principal damage mechanism of this composite under the load condition employed was identified to be the crack bridging and fiber/matrix debonding confined to regions near the crack surfaces.					
14. SUBJECT TERMS Crack Growth, Thermal Residual Stresses, Crack Bridging, Fiber Pullout length, Viscoplasticity, Composite Interface				15. NUMBER OF PAGES 150	
				16. PRICE CODE	
17. SECURITY CLASSIFICATION OF REPORT Unclassified	18. SECURITY CLASSIFICATION OF THIS PAGE Unclassified	19. SECURITY CLASSIFICATION OF ABSTRACT Unclassified	20. LIMITATION OF ABSTRACT UL		

ASPECTS OF HIGH TEMPERATURE DAMAGE IN FIBER REINFORCED TITANIUM METAL MATRIX COMPOSITES

**Annual Report
July 1993**

By

H. Ghonem, D. Zheng, et al

**Department of Mechanical Engineering
University of Rhode Island
Kingston, RI 02881-0805**

Prepared for

**Department of Air Force
Air Force Office of Scientific Research
Bolling Air Force Base, DC 20332-6448**

Grant AFOSR-92-F49620

DTIC QUALITY INSPECTED 3

Accession For	
NTIS CRA&I	<input checked="checked" type="checkbox"/>
DTIC TAB	<input type="checkbox"/>
Unannounced	<input type="checkbox"/>
Justification	
By	
Distribution /	
Availability Codes	
Dist	Avail and/or Special
A-1	

SUMMARY

The work described in this report is part of an ongoing research program conducted during the period June 1992 to June 1993. In this period, the work has focussed on the understanding of high temperature fatigue crack growth behavior of the titanium metal matrix composite (Timetal 21S reinforced by continuous σ 1240 fibers). Aspects associated with this main theme were investigated and are presented in this report in the form of five separate sections. In the first section, the fatigue and fatigue crack growth characteristics in neat laminates made of Timetal 21S were studied in relation to both temperature and loading frequency effects. The second section deals with the evolution of the thermal residual stresses in the composite when cooling from consolidation temperature or subjecting the composite to thermal cycles. A new mechanical simulation method capable of measuring the induced residual stress on real; time basis has been developed in this study. The third section extends this issue to the time-dependent internal stress and strain states of MMCs under the thermomechanical loading conditions. Here, a new micromechanical model employing the four-phase concentric cylinder configuration has been proposed. Based on this model, the time-dependent behavior of continuous fiber reinforced metal matrix composites has been evaluated for the SCS-6/Timetal 21S composite. These results are presented in the fourth section. The last section of this report deals with the high temperature fatigue crack growth characteristics of the continuous fiber reinforced titanium metal matrix composite σ 1240/Timetal 21S. The time-dependent features of the crack growth was examined in relation to the variation of both testing temperature and loading frequency. The principal damage mechanism of this composite under the load condition employed was identified to be the crack bridging and fiber/matrix debonding confined to regions near the crack surfaces.

The second phase of this research program will focus on damage aspects related to the kinetics of the interface reaction, the influences of aging, environment and hold time on the fatigue crack growth behavior.

ACKNOWLEDGEMENT

The Timetal 21S neat laminates and the Sigma1240/Timetal 21S composite needed for this research program were manufactured by United Technologies, Pratt & Whitney, East Hartford, CT, as part of a joint research program between P&W and the University of Rhode Island. The efforts Mr. J. Beals and Dr. M. Thompson of United Technologies Research Center and Mr. G. Linsey of P&W were critical in achieving optimum laminate and composite materials. Timet Corporation of Henderson, Nevada has supplied the Timetal 21S foils. Dr. P. Bania of Timet has been generous in his support and encouragement of the authors. The authors wish also to acknowledge Mr. J. Hill of the Engineering Division of P&W who was instrumental in establishing a cooperative research program between P&W and URI. The authors are indebted to Dr. T. Nicholas of Wright-Patterson AFB who has contributed his time and ideas towards all the research subjects reported here. This research is supported by USAF Office of Scientific Research under grant F49620. Dr. W. Jones is the program manager. His guidance and encouragement of the authors during the first phase of this program are very much appreciated.

LIST OF CONTENTS

Summary	i
Acknowledgement	ii
List of Content	iii
List of Tables	vi
List of Figures	vii
Section 1: Effects of Temperature and Frequency on Fatigue Crack Growth in Timetal 21S Monolithic Laminate	1
Abstract	1
1.1 Introduction	1
1.2 Material Description	2
1.3 Experimental Procedure	3
1.4 Results and Discussion	4
1.5 Summary and Conclusions	7
1.6 Appendix	8
1.7 References	10
Section 2: Thermal Residual Stress in Titanium Metal Matrix Composites	28
Abstract	28
2.1 Introduction	28
2.2 Theory	30
2.3 Mechanical Simulation Method	33
2.4 Material and Experimental Procedure	35

2.5 Results, Analysis and Discussion	36
2.6 Conclusions	39
2.7 References	40
Section 3: Micromechanical Modelling of Time-Dependent Behavior of Continuous-Fiber-Reinforced Metal Matrix Composites	54
Abstract	54
3.1 Introduction	54
3.2 Concepts of the Micromechanical Approach	55
3.3 Formulation	57
3.3.1 Elastic-Plastic Analysis	59
3.3.2 Creep Analysis	62
3.4 Solution Procedures	65
3.5 Summary and Conclusions	67
3.6 References	68
Section 4: Parametric Study of the Time-Dependent Behavior of Continuous-Fiber Reinforced Metal Matrix Composites Based on Micromechanical Model	75
Abstract	75
4.1 Introduction	75
4.2 Parametric Study	76
4.2.1 Thickness of the Equivalent Composite Media	77
4.2.2 Fiber Coating Material and Thickness of the Interfacial Region	78
4.2.3 Role of Creep Deformation in the Evolution of Thermal Stresses	79

4.2.4 Evolution of Thermal Stresses During Thermal Cycling	80
4.3 Conclusions	81
4.4 References	81
Section 5: High Temperature Fatigue Crack Growth of the Continuous Fiber Reinforced Titanium Metal Matrix Composite Sigma/Timetal 21S .	103
Abstract	103
5.1 Introduction	103
5.2 Material and Experimental Procedure	104
5.3 Results	106
5.4 Discussion	109
5.5 Conclusions	112
5.6 References	113

LIST OF TABLES

Table	Title	Page
1.1	Mechanical Properties of Timetal 21S	3
1.2	Test Matrix	4
2.1	Test Conditions	35
5.1	Mechanical Properties of the Fiber and the Matrix	105
5.2	Variations of τ and h_T with Temperatures and Frequencies	108

LIST OF FIGURES

Figure	Caption	Page
1-1	Microstructure of Timetal 21S monolithic laminate	12
1.2	Optical micrograph showing interface region in Timetal 21S monolithic laminate	13
1-3	Tensile stress-strain curve of Timetal 21S monolithic laminate at different temperatures	14
1-4	Degree of data scatter of several identical fatigue crack growth tests	15
1-5	Effects of specimen geometry on fatigue crack growth rates	16
1-6(a)	Temperature effects on fatigue crack growth rates	17
1-6(b)	Effects of variations in yield strength and elastic modulus due to test temperature on fatigue crack growth rate data	18
1-7	Isothermal fatigue life of Timetal 21S monolithic laminate at 482°C and 550°C	19
1-8(a)	' + (1 fracture surface features of Timetal 21S monolithic laminate at 23°C and 10 Hz	20
1-8(b)	Typical fracture surface features of Timetal 21S monolithic laminate at 650°C and 10 Hz	21
1-8(a)	Typical fracture surface features of Timetal 21S monolithic laminate at 760°C and 10 Hz	22
1-9	Effects of loading frequency on fatigue crack growth rates in Timetal 21S monolithic laminate at 650°C	23
1-10	Relationship between Paris law exponent and loading frequency . . .	24
1-11	Relationship between crack growth rate and loading cycle duration as a function of ΔK	25

1-12	Transition time from small scale yielding to secondary creep as a function of ΔK at 650°C	26
1-13	Typical fracture surface features of Timetal 21S monolithic laminate at 650°C and 0.05 Hz	27
2-1	Schematic of simplifying the composite major constituents, fiber and matrix, into two bar composite model	44
2-2	Discretization of the cooling path from consolidation temperature to room temperature (no externally applied mechanical load)	45
2-3	Two bar model showing fiber and matrix responses during the first cool down step	46
2-4	Schematic of the idealization of fiber and matrix components in relation to a neat laminate (matrix material) loaded in a testing frame: (a) two bar composite model; (b) equivalent composite specimen where the matrix is restricted by a higher stiffness boundary; (c) equivalent composite system where a fiberless laminate specimen acts as a matrix while the restriction between matrix and fibers is imposed through adjustable loading system	47
2-5	Schematic of the simulation logic applied in the present study to estimate residual stress in the matrix component of a unidirectional reinforced metal matrix composite. A: heating unit; B: extensometer; C: fiberless laminate specimen; D: loading system; D: testing frame	48
2-6	Evolution of the thermal residual stress in Ti-15-3 matrix during cool-down from consolidation temperature using a cooling rate of 0.5°C/sec	49
2-7	Evolution of the thermal residual stress in Timetal 21S matrix during cool-down from consolidation temperature and subsequent thermal cycling between 100°C and 550°C using a cooling rate of 0.5°C/sec	50
2-8	Evolution of the thermal residual stress in Timetal 21S matrix during cool-down from consolidation temperature and reheating to 575°C using a cooling rate of 0.05°C/sec	51
2-9	Relationship between thermal residual stress in the matrix of SCS-6/Timetal 21S composite and corresponding inelastic strain as function of testing temperature	52

2-10	Relationship between the strain hardening parameter of the matrix material of SCS-6/Timetal 21S and the number of thermal cycles . .	53
3-1(a)	Selected configuration of a unit cell with surrounding composite material	69
3-1(b)	Cut-out section of the four-phase model	70
3-2	Discretization of the cooling/heating path (no externally applied mechanical load)	71
3-3	(a) Reference state at consolidation. (b) Constraint-free thermal deformation. (c) Equilibrium conditions due to boundary constraints. (d) Constraint-free creep deformation. (e) Final equilibrium conditions at the end of the first temperature-time step loading	72
3-4	Flow charts for elastic-plastic-creep algorithm	73
3-5	Strain history prediction for the first two load steps from strain hardening method	74
4-1(a)	Physical properties of the constituents: CTE	83
4-1(b)	Physical properties of the constituents: Young's modulus	84
4-1(c)	Physical properties of the constituents: Yield strength of Timetal 21S	85
4-2(a)	Variation of stress field in the matrix layer with size of the equivalent composite: Radial Component.. . . .	86
4-2(b)	Variation of stress field in the matrix layer with size of the equivalent composite: Hoop Component.. . . .	87
4-2(c)	Variation of stress field in the matrix layer with size of the equivalent composite: Axial Component.	88
4-3	Frequency distribution of center-to-center spacings between fibers in Ti-15-3 composite with 35% fiber volume fraction	89
4-4	Idealized array of fibers in MMC with 35 % fiber volume fraction .	90
4-5(a)	Variation of radial stress field in the matrix with thickness of fiber coating for different coating materials.	91

4-5(b)	Variation of hoop stress field in the matrix with thickness of fiber coating for different coating materials.	92
4-5(c)	Variation of axial stress field in the matrix with thickness of fiber coating for different coating materials.	93
4-5(d)	Variation of radial stress field in the interface region with thickness of fiber coating for different coating materials.	94
4-5(e)	Variation of hoop stress field in the interface region with thickness of fiber coating for different coating materials.	95
4-5(f)	Variation of axoial stress field in the interface region with thickness of fiber coating for different coating materials.	96
4-6(a)	Physical properties of the composite constituents at room temperature: CTE	97
4-6(b)	Physical properties of the composite constituents at room temperature: Young's modulus	98
4-7	Evolution of axial thermal stress in the matrix during initial cool-down at 0.5 °C/sec.	99
4-8	Amount of stress reduction due to creep in the matrix at various cooling rates	100
4-9	Evolution of axial thermal stress during initial cool-down at 0.5 °C/sec.	101
4-10	Evolution of axial thermal stress in the matrix during initial cool-down and thermal cycle between 100 - 550°C at 0.5°C/sec.	102
5-1(a)	A polished and etched cross section of the as-fabricated σ 1240/Timetal 21S composite specimen(observe the hexagonal fiber arrangements)	117
5-1(b)	Microstructure details of the Timetal 21S matrix in the fiber surrounding region. Note the fine grains around the area of the fiber/matrix interface	118
5-2(a)	Polished surfaces of test specimens showing crack bridging and positions of fiber fracture for 24 °C/10 Hz test stopped after the crack growth retardation stage	119

5-2(b)	Polished surfaces of test specimens showing crack bridging and positions of fiber fracture for 650 °C/ 0.1 Hz test stopped at the instable fracture stage. This figure shows the fracture of all bridged fibers	120
5-3	Variation of the crack length, 2a, with the number of fatigue cycles, N, for different test conditions. (a) 24 °C/10 Hz; (b) 500°C/10 Hz; (c) 650°C/10Hz; (d) 650°C/0.1Hz; (e) 650°C/0.02Hz	121
5-4(a)	Fatigue crack growth rate, da/dN, versus crack length, 2a, for different test temperatures	122
5-4(b)	Fatigue crack growth rate, da/dN, versus crack length, 2a, for different loading frequencies	123
5-5	General view of the fracture surface obtained from 650 °C/10 Hz test showing the crack retardation stage and the crack growth acceleration stage	124
5-6(a)	Severe fiber core damage in the crack growth retardation stage at low magnification (650 °C/10 Hz)	125
5-6(b)	Severe fiber core damage in the crack growth retardation stage at high magnification (650 °C/ 0.1 Hz)	126
5-7(a)	View of the instable fracture region at low magnification (650 °C/0.1 Hz, arrow indicates the crack growth direction and the lower left part of the fracture surface is the instable fracture region)	127
5-7(b)	View of the instable fracture region at high magnification (650 °C/0.02 Hz), observe the degree of the matrix viscoplastic flow surrounding the pullout fibers	128
5-8	Distributions of the fiber pullout length for various test conditions. The dashed line is a regression fitting of data corresponding to be the crack growth retardation stage. (a) 24°C/10Hz; (b) 500°C/10Hz; (c) 650°C/10Hz; (d) 650°C/0.1Hz; (e) 650°C/0.02Hz	129
5-9(a)	Typical matrix transgranular fracture features due to the high frequency tests is transgranular	130
5-9(b)	Typical matrix features due to the low frequency loadings (650°C/0.02 Hz). The fracture mode is a mixture of intergranular and transgranular	131

5-10	Typical radial cracks in the interfacial region and severe oxidation damage of the fiber coating layers in the low frequency tests (650°C/0.02 Hz)	132
5-11	Local viscoplastic flow around fiber regions indicating matrix stress relaxation	133
5-12(a)	Fatigue crack growth rate, da/dN , in the composite versus the nominal applied stress intensity factor range, ΔK_{app} , for various temperatures	134
5-12(b)	Fatigue crack growth rate, da/dN , in the composite versus the nominal applied stress intensity factor range, ΔK_{app} , for various loading frequencies	135
5-12(c)	Fatigue crack growth rate, da/dN , in the composite versus the effective applied stress intensity factor range, ΔK_{eff} , for the crack growth retardation stage only	136
5-13	Comparison between the fatigue crack growth rates in the composite and the laminate matrix material	137

SECTION 1

EFFECTS OF TEMPERATURE AND FREQUENCY ON FATIGUE CRACK GROWTH IN TIMETAL 21S MONOLITHIC LAMINATE¹

ABSTRACT

This section describes the high temperature fatigue crack growth behavior in the titanium β 21S monolithic laminates. Effects of laminate consolidation procedure as well as the test specimen geometry on the reliability of the experimental crack growth data were first investigated. The influence of temperature and both high and low frequency loadings on the crack growth rate in this laminate material were then determined. In addition to room temperature three other temperature levels were used in this study: 482°C, 650°C and 760°C. The test frequencies encompassed the range 10 to 8×10^{-3} Hz. Results of this study demonstrate that temperature effects could be interpreted in terms of the yield strength and elastic modulus variations as function of the testing temperature. Furthermore, it was determined that crack growth rate in these laminates is influenced by viscoplastic related effects at frequencies as low as 1 Hz. This was supported by an analytical solution determining the transition time required for the crack tip to experience extensive creep behavior. Fractographic analysis carried out on fracture surfaces showed that the dominant fracture mechanism is transgranular cleavage with the appearance of intergranular facets in tests corresponding to 760°C at 10 Hz and 650°C at 5×10^{-2} Hz.

1.1 INTRODUCTION

With rapid advances in titanium alloys, extending their operating temperature to 593°C [1,2], fiber-reinforced titanium-based metal matrix composites have emerged as a class of composites with a potential for use in advanced high temperature applications. The target operation temperature range of 650-800°C in these applications would overlap that of superalloys.

Four basic titanium alloys are available for metal matrix composite applications [3,4]. These are: the α alloys, the α - β alloys, the metastable β alloys and the stable β alloys. In these types of alloys the α class is avoided as a matrix material due to its low alloy content and the inherent low strength. On the other hand, the stable β materials suffer generally from problems related to both processing [5] and the fabrication into the required thin-gage foils [6]. The α + β and metastable β alloys thus remain as the only candidates for use in matrix development; they can be fabricated with relative ease and can be aged to high strengths. One of the approaches that has been investigated in conditioning the metastable β alloys toward

¹ based on "Effects of temperature and frequency on fatigue crack growth in Ti- β 21S monolithic laminate", H. Ghonem, Y. Wen, D. Zheng, M Thompson and G. Linsey, *Materials Science and Engineering*, Vol. A161, pp.45-53, 1993.

titanium-based MMC applications is through alloying with slower diffusing elements in order to reduce the reaction zone width at the consolidation temperature, thus limiting the complications ensuing from matrix-to-filament load transfer which takes place across the reaction zone. In this regard, it was proposed by Schmitz et al [7] that the optimum titanium matrix, for a boron type filament, would be attained through the addition of enough diboride modifier, such as, vanadium or chromium, to reduce boron transport to a minimum as well as by the addition of aluminum or molybdenum to reduce the reactivity of the titanium. These two modifier requirements have been achieved with the development of a new metastable β alloy Timetal 21S. This alloy, when combined with a fiber with a boron-rich surface, should yield a composite that could prove to be thermally and mechanically stable at operating temperatures of up to the 700°C range.

Since applications of high temperature MMC involve in many cases cyclic loading due to thermal and or mechanical service conditions. The understanding of high temperature fatigue crack growth in the matrix material therefore becomes an important factor since it defines the limits of the composite response and identifies the nature and parameters governing the damage evolution in the intended composite structure. The purpose of this section is to evaluate the high temperature fatigue crack growth behavior in Timetal 21S laminate. The first part of the paper describes the material characteristics and basic properties and the experimental procedure used in this study. This will be followed by a discussion of experimental results, in particular temperature and frequency effects and their significance in relation to the use of the Timetal 21S as a matrix material for fiber-reinforced composites.

1.2 MATERIAL DESCRIPTION

The basic material used here is the metastable Timetal 21S alloy supplied in the form of foils with a thickness of 112 μm . The chemical composition of this alloy in wt% is 0.1 Fe, 16.0 Mo, 3.0 Al, 0.9 Nb, 0.2 Si, 0.22 C, 0.12 O, 0.005 N with the balance being Ti. The microstructure of the heat treated alloy consists of distinctive β grains containing widmanstätten acicular α phase and continuous grain boundary α layer with the thickness of about 0.8 μm , shown in Fig. 1-1. The average grain size is about 80 μm . The room temperature tensile properties of these foils are: ultimate tensile stress $\sigma_{\text{UTS}} = 1089 \text{ MPa}$, elastic modulus $E = 98 \text{ GPa}$ and elongation $\delta = 5.6\%$. Laminates were fabricated by consolidating eight foils using vacuum hot pressing employing pre-established critical processing parameters. This process produced monolithic laminate plates with dimensions 25.4 mm x 0.8 mm x 150 mm. Prior to consolidation, the foils surface oxide was removed using a combined vapor hone and a mechanical oxide removal technique. Typical microstructure of the consolidated laminates is shown in Fig. 1-2. It is observed that while no changes have occurred in the basic microstructure of the foil, the microstructure of the interfaces displays a decrease in grain size. This was interpreted here as being related to strain bands formed along the foils interfaces during consolidation. These bands could result in heterogeneous nucleation of grains which are restricted by the foil interface resulting in smaller grain size than those in the foil interior.

As will be discussed later, no damage or partial separation was encountered along these interfaces during the early parts of the crack growth process. All laminates were heat treated (621°C/8 hrs) in a dynamic vacuum furnace prior to machining the required test specimens.

Preliminary tensile tests were performed on heat treated specimens made of the optimized laminates in order to determine their basic mechanical properties at five different temperatures: 24°C, 204°C, 316°C, 482°C and 649°C. Tensile stress-strain curves were recorded and ultimate tensile strength, 0.2% yield strength and elastic modulus were measured. Quartz rod axial extensometry was utilized to measure strain. Results of these measurements in the form of stress-strain curves are shown in Fig. 1-3, while the different related properties are listed in Table 1.1.

Table 1.1 Mechanical Properties of Timetal 21S

Temperature (°C)	σ_{UTS} (MPa)	0.2% Yield Stress (MPa)	E (GPa)	Strain at Failure (%)
24	1089	1043	98.2	>3.9
204	877	779	90.3	8.7
316	843	696	84.8	6.8
482	684	589	76.0	>10.1
649	289	245	47.6	50-55

1.3 EXPERIMENTAL PROCEDURE

Three specimen configurations were investigated in order to identify the effect of geometry on crack growth behavior. These geometries include Compact Tension (width=25.4 mm, thickness = 0.87 mm), Single Edge Notch (SEN) and Middle Cracked Tension (MT) specimens. The latter two geometries had a gage section of 30 mm. All specimens were precracked at room temperature using a stress intensity factor shedding technique. In the case of the MT configuration, a small cut was introduced on both sides of the center hole in order to direct the initial precracks. These cuts were made using a silicon-carbide coated chromel wire with a diameter of 76 μm .

All tests were carried out on an automated servo-hydraulic test frame. Test specimens were gripped using a hydraulic flat grip with self aligning capabilities and heated with an open furnace utilizing infrared radiation lamps. The testing temperatures employed here were 23°C, 482°C, 650°C and 760°C. The variation of the temperature along the gage length during all tests was $\pm 5^\circ\text{C}$. Crack length increments were measured continuously using a direct current potential drop method based on optically derived calibration curves. All fatigue crack growth tests, summarized in Table 1.2, were carried out under load range control with loading frequencies of 1, 10, 5×10^{-2} and 8×10^{-3} Hz applied at a stress ratio of 0.1.

It was not possible to obtain crack opening displacement during either room or elevated temperature testings and therefore crack closure data are lacking here. Fracture specimens were examined using optical and scanning electron microscopy in order to identify fracture features

and determine related cracking mechanisms as functions of both temperature and loading frequency.

1.4 RESULTS AND DISCUSSION

This section will focus on analyses of test results pertaining to effects of temperature and loading frequency on crack growth behavior in the laminate understudy. This will be preceded by a description of efforts to determine the reliability of data obtained from specimens made of the laminates under study.

Table 1.2 Test Matrix*

Test Case	Specimen Configuration	Temperature (°C)	Frequency (Hz)
1	MT	760	10
2	SEN	650	8×10^{-3}
3	SEN	650	5×10^{-2}
4	SEN	650	1
5	SEN	650	10
6	MT	482	10
7	SEN	23	1
8	CT	23	1
9	MT	23	1
10	SEN	23	1
11	SEN	23	10
12	SEN	23	10
13	SEN	23	10

* All tests were carried out in laboratory air environment.

Since monolithic laminate material is a product of a consolidation process which involves the optimization of parameters such as temperature, pressure and environment, variations in any of these parameters could produce changes in the microstructure uniformity of the test specimens which in turn could influence the crack growth behavior in these specimens. Therefore, prior to carrying out any major crack growth characterization, two aspects of the laminate material reliability have been investigated: the degree of data scatter and the influence of specimen

geometry. Results relating to each of these aspects and their significance in relation to the laminate performance will be discussed here.

The degree of crack growth data scatter has been investigated by carrying out several identical crack growth tests using different SEN specimens at room temperature under the same loading frequency of 10 Hz. This high level of frequency was selected in order not to introduce time-dependent related effects in the experimental outcome. Results in the form of da/dN versus ΔK are compared in Fig. 1-4. While the size of this data set is small and does not permit performing a quantitative statistical analysis, qualitative estimate of the scatter in these data in relation to that observed in other high temperature titanium alloys [8,9], indicates that the crack growth response of a single experiment could be taken as representative of the laminate response under the particular test conditions.

The second reliability test carried out here was related to the effect of the specimen geometry and its inherent bending characteristics on the crack growth process of the laminate. Three geometries have been utilized: CT, SEN and MT configurations. Crack growth increments in these specimens were measured at room temperature under, again, a high loading frequency of 10 Hz. By utilizing the applicable ΔK expression for each of these specimen configurations, the da/dN versus ΔK results for test cases 7, 8 and 9 in Table 1.2 are plotted in Fig. 1-5. They show that the crack growth response is identical in all of the specimen geometries in the range of ΔK up to $30 \text{ MPa}\sqrt{\text{m}}$, which is the crack growth region of concern in this study. On the basis of these results, the SEN and MT configuration, due to the simplicity of their preparations and precracking procedures, have been adopted in the rest of this study.

The influence of temperature on crack growth was explored by carrying out tests labeled as cases 1, 5, 6 and 10 in Table 1.2, which were performed at temperatures of 760°C , 650°C , 482°C and 23°C , respectively, under a loading frequency of 10 Hz. Results of these tests which are plotted in Fig. 1-6(a), show that the increase in the test temperature from 23°C to 482°C has not produced any noticeable variations in the crack growth rate. The increase of the test temperature to 650°C and 760°C have however produced an increase in the crack growth rate along the entire range of ΔK and in particular in the low ΔK region. This difference could be interpreted in terms of time-dependent oxidation and or creep related effects. It could also result from variations in mechanical properties of the laminate due to temperature changes. In order to isolate these effects, the values of the stress intensity factor range, ΔK , were modified by accounting for the temperature induced changes in both the yield strength, σ_y , and elastic modulus, E . The normalized values of ΔK calculated as $(\Delta K^2/\sigma_y E)$ is plotted versus da/dN in Fig. 1-6(b). It shows that the crack growth curves corresponding to the three temperature levels: 23°C , 482°C and 650°C are almost identical. Since the loading frequency in these three cases was confined to the high frequency level of 10 Hz, thus ruling out the existence of creep effects, one would assume that crack tip oxidation is a major damage mechanism at these temperature levels. The absence of crack growth enhancement as function of temperature, however, could therefore be viewed as a measure of the material high resistance to oxidation effects over this temperature range. This conclusion, in fact, is supported by results obtained by Khobaib [10] who analyzed the weight gain during the thermal exposure of Timetal 21S laminates at different temperature levels in a 10 torr atmosphere. His work showed that little environment effects occurred in these laminates up to 650°C .

The exclusion of the 760°C test data from comparisons in Fig. 1-6(b) is due to the fact

that the validity of this test was limited to the ΔK range 4-7 MPa \sqrt{m} . Beyond this ΔK level the corresponding test specimen experienced extensive delamination. This phenomenon of delamination was apparent in all the elevated temperature test specimens at ΔK above 25 MPa \sqrt{m} . This ΔK value was found to increase with decreasing testing temperature and increasing loading frequency. The existence of delamination is speculated here to be a result of extensive viscoplastic flow taking place at high ΔK , which causes the material ligament ahead of the crack tip to experience bending effects during the rising part of the loading cycle. This bending, which is exaggerated in the case of the SEN geometry, will consequently result in compressive stresses acting in the normal-to-loading direction. These stresses could cause delamination along the foil interfaces since they are expected to be weak boundaries of the laminate structure. This speculative view relies on the fact that the laminate material undergoes a transition to large scale yielding at high ΔK values in less than 10 seconds of thermal exposure at 650°C; this will be discussed later in this section. It should be mentioned here that delamination was not observed in tests carried out at room temperature.

While the results shown in Fig. 1-6(b) demonstrates the absence of extrinsic temperature effects on crack growth behavior, life to failure of this laminate material was found to be temperature dependent. This was evident from load versus life curves obtained at different temperature levels. These curves are plotted in Fig. 1-7 in the form of maximum stress normalized by ultimate tensile stress ($\sigma_{max}/\sigma_{UST}$) versus number of cycles to failure. They show that a decrease of life occurs as temperature increases from 482°C to 650°C. This was interpreted as due to the effect of the decrease in yield strength on the crack initiation life and increasing environmental effects [11,12]. Numerous surface crack initiation sites were found in the 650°C test specimen while no surface cracks were observed in the 482°C test.

Fractographic analysis of the high frequency fractured specimens showed that the cracking mechanisms in those specimens tested in the range of 23 °C to 650 °C are transgranular with cleavage-like fracture covering the fracture surfaces in regions extending from $\Delta K = 4$ to 20 MPa \sqrt{m} . Unlike other titanium alloys [7], no transition in fracture mode was found in this β 21S monolithic laminate and the commonly observed striations were absent even at high ΔK values. Sheared facets were found to be more defined in the 650°C case than those observed in the room temperature tests, compare Figs. 1-8(a) and 1-8(b). At 760°C, however, the fracture mode becomes intergranular with distinct ledges on grain boundary facets, see Fig. 1-8(c).

The second aspect studied here was the influence of loading frequency on crack growth behavior. Generally, the change in the crack growth rate due to variations in time durations of the applied loading cycle is used as a measure of the crack tip material response to time dependent parameters which consist of creep and /or oxidation related effects [13-15]. This is particularly important in the low ΔK region where stress-controlled crack growth rate is generally small thus permitting the time dependent effects to be observed and evaluated. Two different frequencies were employed at the temperature of 650°C, 5×10^{-2} and 8×10^{-3} Hz. Crack growth rates due to these frequencies, in addition to those corresponding to 1 and 10 Hz used as references, are plotted in Fig. 1-9. Similar to most high temperature alloys, these results show that a decrease in the loading frequency leads to crack growth rate acceleration. In order to identify the nature of this acceleration, the following form of the Paris-type equation has been utilized in an analysis similar to that developed by Foerch et al [8] in their work on the Ti-1100 alloy:

$$\frac{da}{dN} = C(650^\circ, \text{freq}, \text{envir}) \Delta K^{m(650^\circ, \text{freq}, \text{envir})} \quad (1)$$

In the case of cycle dependent crack growth processes which involve damage criteria related to crack opening displacement or strain accumulation, the exponent m could vary between 2 and 4, respectively. The steady state regions of the crack growth curves corresponding to 650°C have been fitted into the form of the above equation. The exponents of the resulting equations were then plotted versus the loading frequency as shown in Fig. 1-10. They indicate that at loading frequencies above 0.1 Hz the cracking mechanism is a cyclic dependent, while below this frequency the damage is a mixed cycle- and time-dependent process. This results in an exponent m which varies inversely as a function of frequency. At the frequency level of 10^{-3} Hz the crack tip damage process becomes fully time dependent. This contention is further supported by results obtained in Fig. 1-11, where the crack growth rate at 650°C is plotted versus cycle duration for ΔK values of 5, 7, 9, 15 and 20 MPa \sqrt{m} . Here, on the basis of similar analyses made by other workers in their studies of crack growth in high temperature alloys [13-16], the slopes of these ΔK versus time lines are considered a measure of the time dependent contributions to the crack tip damage process. If the dotted curve in Fig. 1-11 is taken as a boundary at which transition to time-dependent behavior occurs (the slopes of curves approach to the unity), it could be seen that as ΔK increases the transition frequency increases; for ΔK of 20 MPa \sqrt{m} , the transition frequency is about 1 Hz. An attempt was then made to probe the nature of the time dependent effects by estimating the time required for the crack tip to experience extensive creep. This was achieved by employing an approach based on Riedel-Rice analysis for creeping materials [17]. In this approach, the time necessary for transition from small scale yielding to large scale secondary creep is estimated as function of the applied load and ΔK . Details of this calculation is given in an appendix at the end of this section. The results in the form of time required for extensive creep versus ΔK for the applied load level used in this study is shown in Fig. 1-12. It clearly shows that the crack tip undergoes large scale yielding in less than 10 seconds of thermal exposure at 650°C and ΔK of 17 MPa \sqrt{m} .

The influence of creep is in fact evident when viewing the fracture surface of specimens corresponding to test case 3, 650°C at 5×10^{-2} Hz, which shows distinctive intergranular failure with multiple grain boundary triple-point cracks (see Fig. 1-13). However, the intergranular fracture associated with the specimen tested at 760°C and 10 Hz is assumed here to be due to environmental degradation since the testing temperature is high enough to cause severe oxidation [10], while cycle duration is not long enough to produce creep flow effects. This conclusion is supported by comparing Figs. 1-8(c) and 1-11. They show that intergranular features associated with the 760°C, 10 Hz test condition are more brittle in appearance than those associated with the 650°C, 5×10^{-2} Hz test condition.

1.5 SUMMARY AND CONCLUSIONS

In this study, an experimental program has been carried out to characterize the high temperature fatigue crack growth behavior of the Timetal 21S monolithic laminate. In this, the influence of consolidation and specimen geometry on the reliability of crack growth data in this

laminated material have been examined. It was concluded that the crack growth rate versus ΔK relationship at room temperature in laboratory air environment is repeatable and to a great extent insensitive to specimen geometry.

Effects of increase in testing temperature on the acceleration of crack growth rate was studied for temperatures 23°C, 482°C, 650°C and 760°C at the high frequency loadings of 1 and 10 Hz. The observed increase in the crack growth rate in this temperature range was interpreted in terms of variations in basic material properties, particularly yield strength and elastic modulus as function of testing temperature. Laminated delamination was shown to exist when exceeding certain ΔK levels that decrease as the temperature level increases and loading frequency decreases. It is speculated that the delamination in these laminates is a product of high viscoplastic flow acting in the specimen ligament in front of the crack tip. The bending of this ligament, particularly in the case of the edge notch specimen configuration, leads to normal-to-load direction compressive stresses which would result in the delamination of the test specimens.

Furthermore, the role of low loading frequency was investigated at the temperature level of 650°C. The increase in growth rate as frequency decreases was interpreted in terms of increasing viscoplastic effects as cycle duration increases. This was supported by an analytical analysis involving the determination of the time required for the crack tip to experience large scale yielding. It was concluded that the time-dependency of fatigue crack growth could be due to the extensive creep deformation. The fact that the oxidation effects may be limited and creep processes can be dominant in Timetal 21S laminated material may make this material attractive for the use as a matrix in high temperature composites in selected applications.

1.6 APPENDIX

The transition time from small scale yielding to large scale creep can be estimated following Riedel-Rice approach [17]. In this approach, an elastic-secondary creeping material in which the strain rate tensor, $\dot{\epsilon}_{ij}$, in the crack tip region is assumed to be expressed as

$$\dot{\epsilon}_{ij} = \frac{1+\nu}{E} S_{ij} + \frac{1-2\nu}{3E} \dot{\sigma} \delta_{ij} + \frac{3}{2} B \bar{\sigma}^{n-1} S_{ij} \quad (2)$$

where the S_{ij} is the deviatoric stress tensor, $\bar{\sigma}$ is the effective stress, δ_{ij} is the Kronecker delta, E is the elastic modulus, ν is the Poisson's ratio, B is temperature-dependent coefficient and n is the Norton's exponent. The asymptotic stress fields in this case can be written as

$$\sigma_{ij} = \left(\frac{C(t)}{B I_n r} \right)^{\frac{1}{n+1}} \bar{\sigma}_{ij}(\theta) \quad (3)$$

where $\bar{\sigma}_{ij}(\theta)$ is the angular function, I_n is a dimensionless factor which is related to n and stress states, r is the distance measured from the crack tip, and the time-dependent loading parameter $C(t)$ is defined as

$$C(t) = \lim_{\Gamma \rightarrow 0} \int_{\Gamma} \frac{n}{n+1} \sigma_{ij} \dot{\epsilon}_{ij} dy - \sigma_{ij} n_j \frac{\partial \dot{u}_i}{\partial x} ds \quad (4)$$

where u_i is a component of the displacement vector. The contour Γ is a vanishingly small loop enclosing the crack tip and is traversed in a counter-clockwise direction.

For short times after application of the load, the near-tip stress field is a function of the independent variables r , θ and t and the parameters K , E , B , ν and n . The Mode I stress intensity factor K is used for the load parameter in small-scale yielding. In this condition, the relationship between $C(t)$ and K can be established as

$$C(t) = \frac{(1-\nu^2)K^2}{(n+1)Et} \quad (5)$$

thus, eq.(3) becomes

$$\sigma_{ij} = \left(\frac{(1-\nu^2)K^2}{(n+1)EBI_n r t} \right)^{\frac{1}{n+1}} \bar{\sigma}_{ij}(\theta) \quad (6)$$

As $t \rightarrow \infty$, the secondary creep extends throughout the body, and $C(t) \rightarrow C^*$ as $t \rightarrow \infty$, where C^* is the path-independent integral defined as

$$C^* = \int_{\Gamma} W dy - \sigma_{ij} n_j \frac{\partial \dot{u}_i}{\partial x} ds \quad (7)$$

in which

$$W = \int_0^{\dot{\epsilon}_{ij}} \sigma_{ij} d\dot{\epsilon}_{ij}$$

is the strain energy rate density and the contour Γ is an arbitrary loop enclosing the crack tip and no other defect. Under this condition, the near-tip stress fields become

$$\sigma_{ij} = \left(\frac{C^*}{BI_n r} \right)^{\frac{1}{n+1}} \bar{\sigma}_{ij}(\theta) \quad (8)$$

The characteristic time for transition from small-scale yielding to extensive creep can be estimated by equating the near-tip fields for short times (eq.(3)) and long times (eq.(8)), and is given as

$$t_T = \frac{(1-\nu^2)K^2}{(n+1)EC^*} \quad (9)$$

where the values of n and B at 650°C are estimated as 5.72 and 2.75×10^{-18} , respectively, see Ref.[10]. C^* can now be calculated using the following expression [18]:

$$C^* = h_1(W-a) B \left(\frac{a}{W} \right) \left(\frac{\sigma_{net}}{1.072\eta} \right)^{n+1} \quad (10)$$

where σ_{net} is the net section stress, and function $h_1(W-a)$ can be determined numerically from the table made by Kumar et al [19], while $\eta = (1 + \alpha^2) - \alpha$ and $\alpha = a/(W-a)$.

The transition time t_T versus ΔK for the applied load level is illustrated in Fig. 1-12. It clearly shows that the transition from small scale yielding which is controlled by K to large scale creep which is determined by C^* would occur as short as about 10 seconds when ΔK level exceeds 15 MPa \sqrt{m} . This transition time is smaller than low frequency cyclic durations in most cases, which implies that severe creep deformation will be expected to occur when this monolithic laminate is subjected to the low frequency and high ΔK loadings.

1.7 REFERENCES

- 1 E. W. Collings, the Physical Metallurgy of Titanium Alloys, American Society for Metals, Metals Park, OH, 1984
- 2 W. Brentnall and I. Toth, High Temp. Ti Compo, TWR, Inc., Cleveland, 1974
- 3 P. R. Smith and F. H. Froes, Developments in Titanium Metal Matrix Composites, Journal of Metals, March, Vol. 36, (1984) pp.19-26
- 4 Titanium: A Technical Guide, ed. by M. J. Donachie, Jr., ASM International, Metals Park, OH 44073, 1989
- 5 I. Weiss and F. H. Froes, "Grain Size Control in the Metastable Beta Titanium Alloy Ti-10V-2Fe-3Al", in Fifth Inter Titanium Conf, Munich, Germany, September, 1984
- 6 P. R. Smith and F. H. Froes and T. Cammet, "Correlation of Fracture Characteristics and Mechanical Properties for Titanium Composites", in Failure Modes in Composites VI, J. A. Cornie and F. W. Crossmann (eds.), the Metallurgical Society of AIME, Warrendale, PA, 1977
- 7 G. K. Schmitz, M. J. Klein, M. L. Reid and A. G. Metcalfe, "Compatibility Studies for Variable Titanium Matrix Composites", AFML-TR-70-237, September, 1970
- 8 H. Ghonem and R. Foerch, "Environmental Effects on Elevated Temp. Fatigue Crack Growth in A Near- α Ti-1100 Alloy", Mat. Sc. and Eng., V. 138A, (1991) pp.69-81
- 9 R. Foerch, A. Madsen and H. Ghonem, "Environmental Influence on the Fatigue Crack Growth Performance of Ti-1100", in 7th World Conference on Titanium, San Diego, CA, June, 1992
- 10 M. Khobaib and N. Ashbaugh, "Mechanical Behavior of β 21S", Technique Report, University of Dayton Research Institute, Dayton, Ohio, 1991

- 11 W. S. Johnson, "Fatigue Testing and Damage Development in Continuous Fiber Reinforced Metal Matrix Composites", in Metal Matrix Composites: Testing Analysis and Failure Modes, ASTM STP 1032, W. S. Johnson (ed.), American Society of Testing and Materials, PA, (1989) pp.194-221
- 12 T. P. Gabb, J. Gayda and R. A. MacKay, "Isothermal and Nonisothermal Fatigue Behavior of A Metal Matrix Composite", J Comp Mat, V. 24, (1990) pp.667-686
- 13 T. Weerasooriya and S. Venkataraman, "Frequency and Environment Effect on Crack Growth in Inconel 718," in Effects of Load and Thermal Histories, P. K. Liaw and T. Nicholas (eds.), the Metallurgical Soc. of AIME, Warrendale, PA, (1987) pp.101-108
- 14 T. Weerasooriya, "Effect of Frequency on Fatigue Crack Growth Rate of Inconel 718 at High Temperature", in Fracture Mechanics: Nineteenth Symposium, ASTM STP 969, T. A. Cruse (ed.), American Society for Testing and Materials, Philadelphia, PA, (1988) pp.907-923
- 15 H. Ghonem and D. Zheng, "Depth of Intergranular Oxygen Diffusion during Environment-Dependent Fatigue Crack Growth in Alloy 718", Materials Science and Engineering, Vol.150, (1992) pp.151-160
- 16 A. Pineau, "Intergranular Creep-Fatigue Crack Growth in Ni-Base Alloys", in Flow and Fracture at Elevated Temperature, R. Raj (ed.), Am Soc for Metals, (1985) pp.317-348
- 17 H. Riedel and J. R. Rice, "Tensile Cracks in Creeping Solids", in Fracture Mechanics: Twelfth Conference, ASTM STP 700, American Society for Testing and Materials, Philadelphia, PA, (1980) pp.112-130
- 18 C. F. Shih and J. W. Hutchinson, "Fully Plastic and Large Scale Yielding Estimates for Plane Stress Crack Problems", Journal of Engineering Materials and Technology, Vol. 98, (1976) pp.289-295
- 19 V. Kumar, M. D. German and C. F Shih, "An Engineering Approach for Elastic-Plastic Fracture Analysis", EPRI NP-1931, Project 1287-1, July, 1981

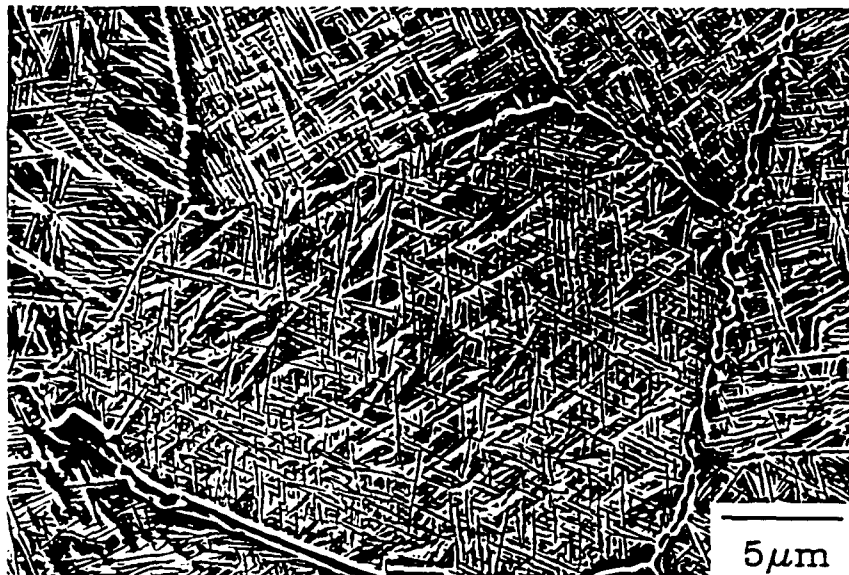


Fig. 1-1 Microstructure of Timetal®21S monolithic laminate.

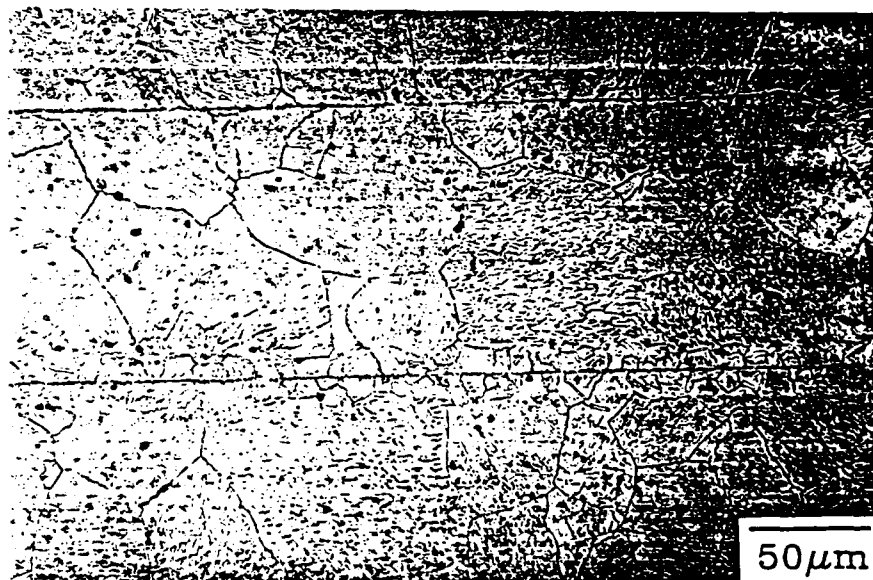


Fig. 1-2 Optical micrograph showing interface region in Timetal®21S monolithic laminate.

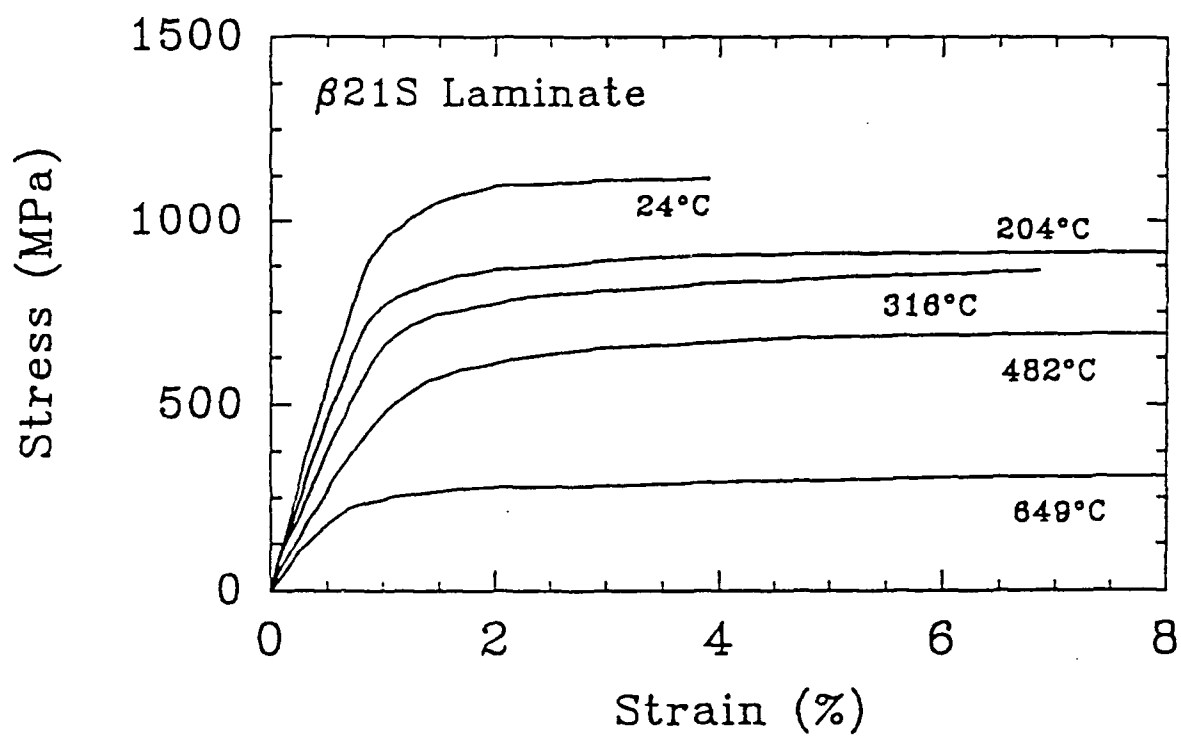


Fig. 1-3 Tensile stress-strain curve of Timetal®21S monolithic laminate at different temperatures.

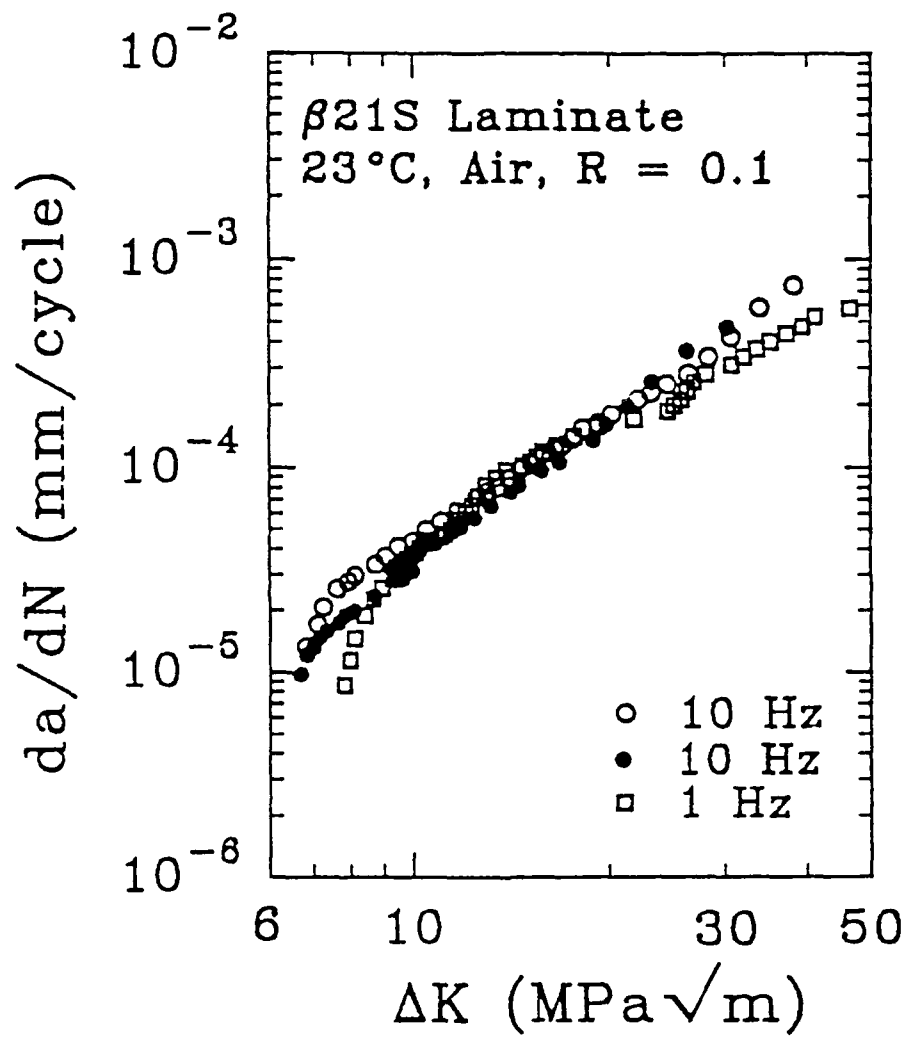


Fig. 1-4 Degree of data scatter of several identical fatigue crack growth tests.

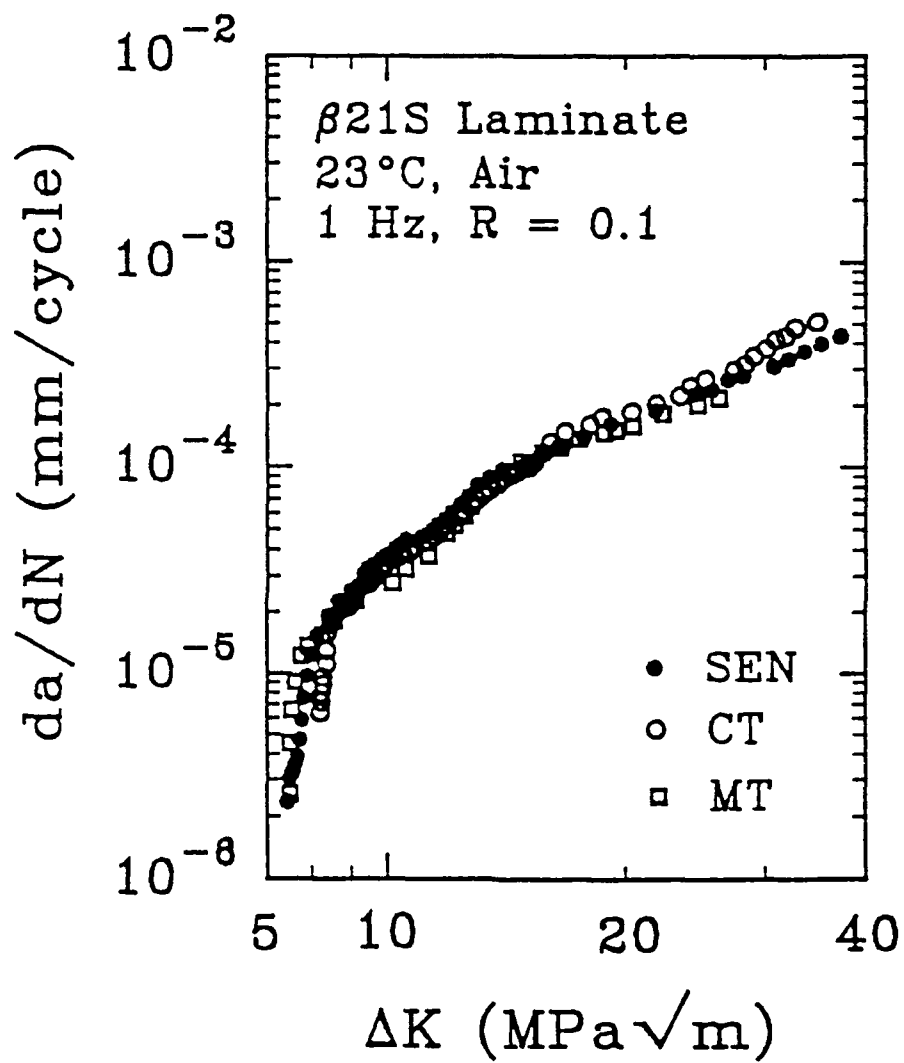


Fig. 1-5 Effects of specimen geometry on fatigue crack growth rates.

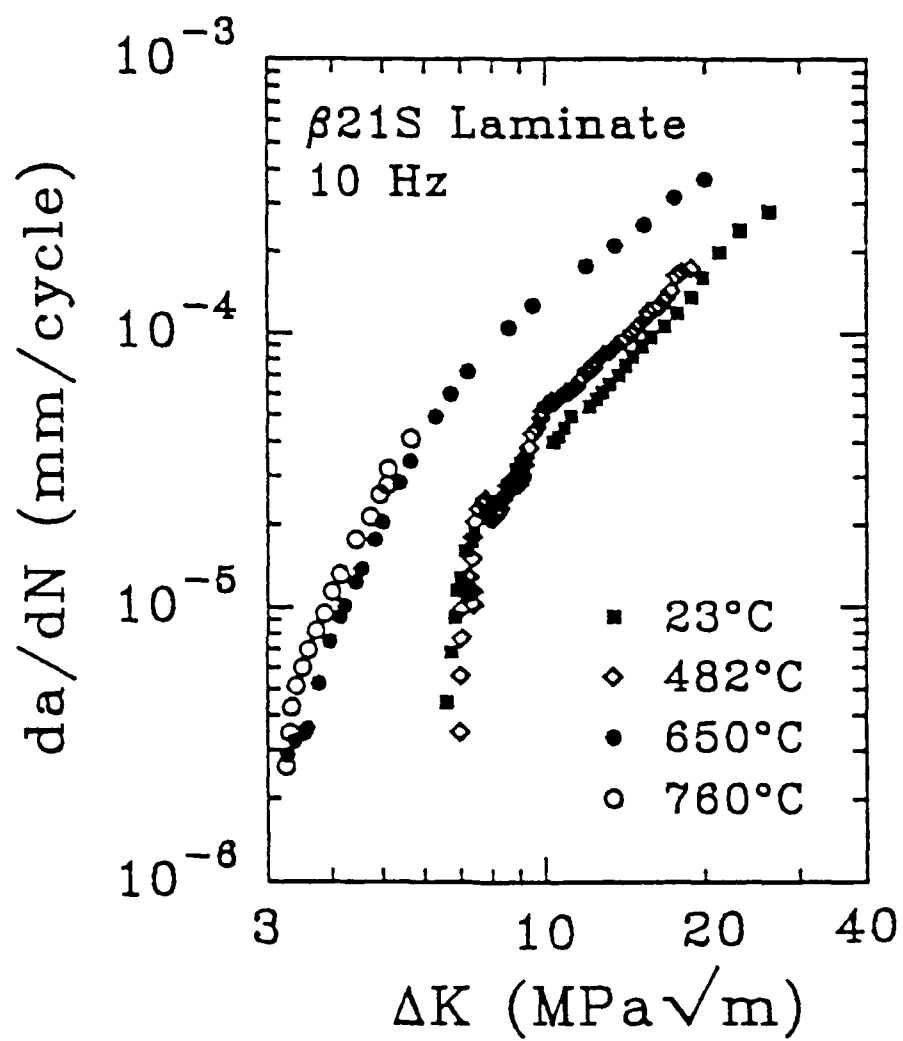


Fig. 1-6(a) Temperature effects on fatigue crack growth rates.

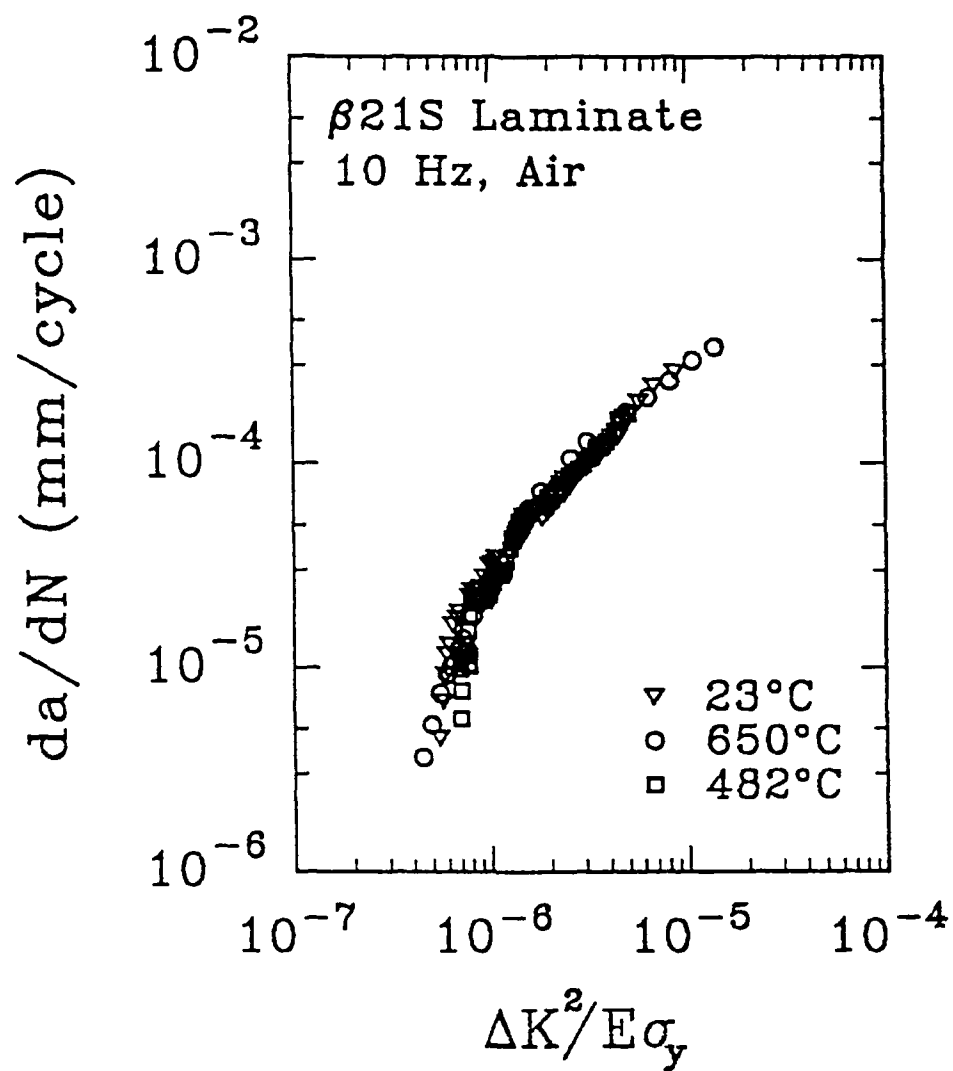


Fig. 1-6(b) Effects of variations in yield strength and elastic modulus due to test temperature on fatigue crack growth rate data.

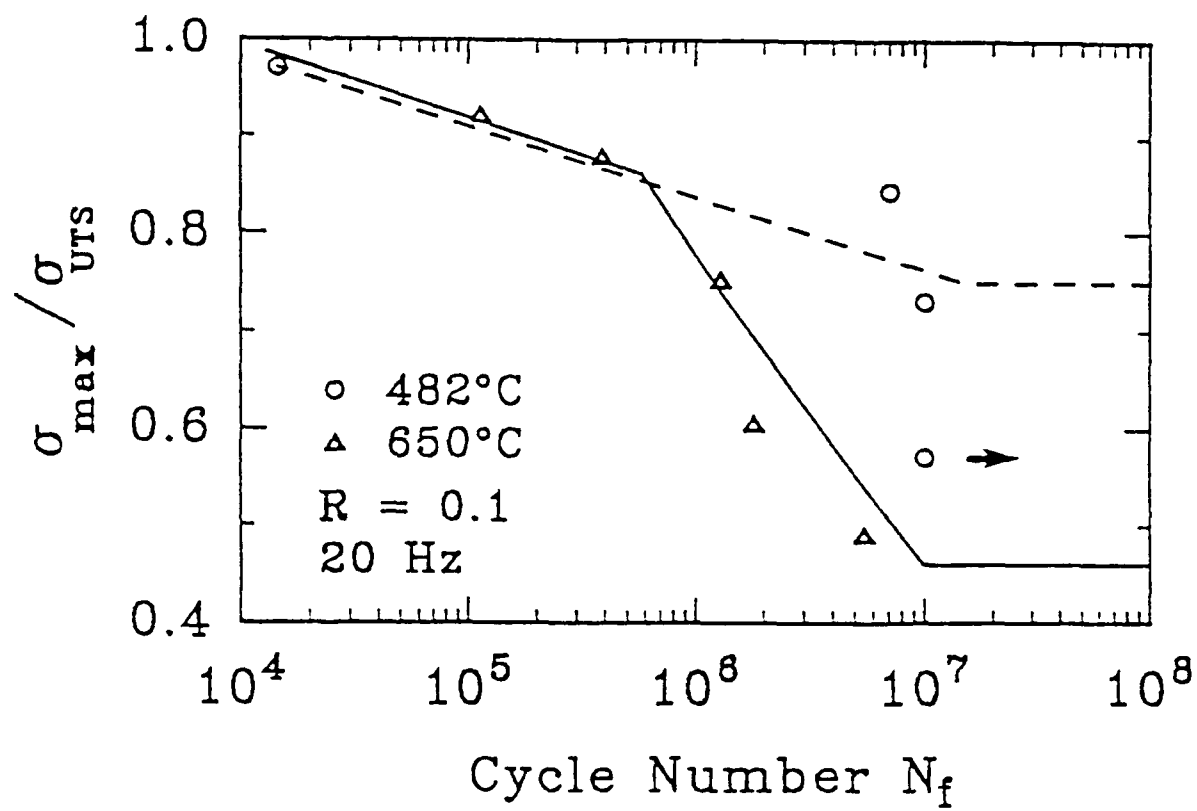


Fig. 1-7 Isothermal fatigue life of Timetal@21S monolithic laminate at 482°C and 650°C.



Fig. 1-8(a) Typical fracture surface features of Timetal®21S monolithic laminate at 23°C, 10 Hz.



Fig. 1-8(b)

Typical fracture surface features of Timetal®21S monolithic laminate at 650°C, 10 Hz.



Fig. 1-8(c)

Typical fracture surface features of Timetal®21S monolithic laminate at 760°C, 10 Hz.

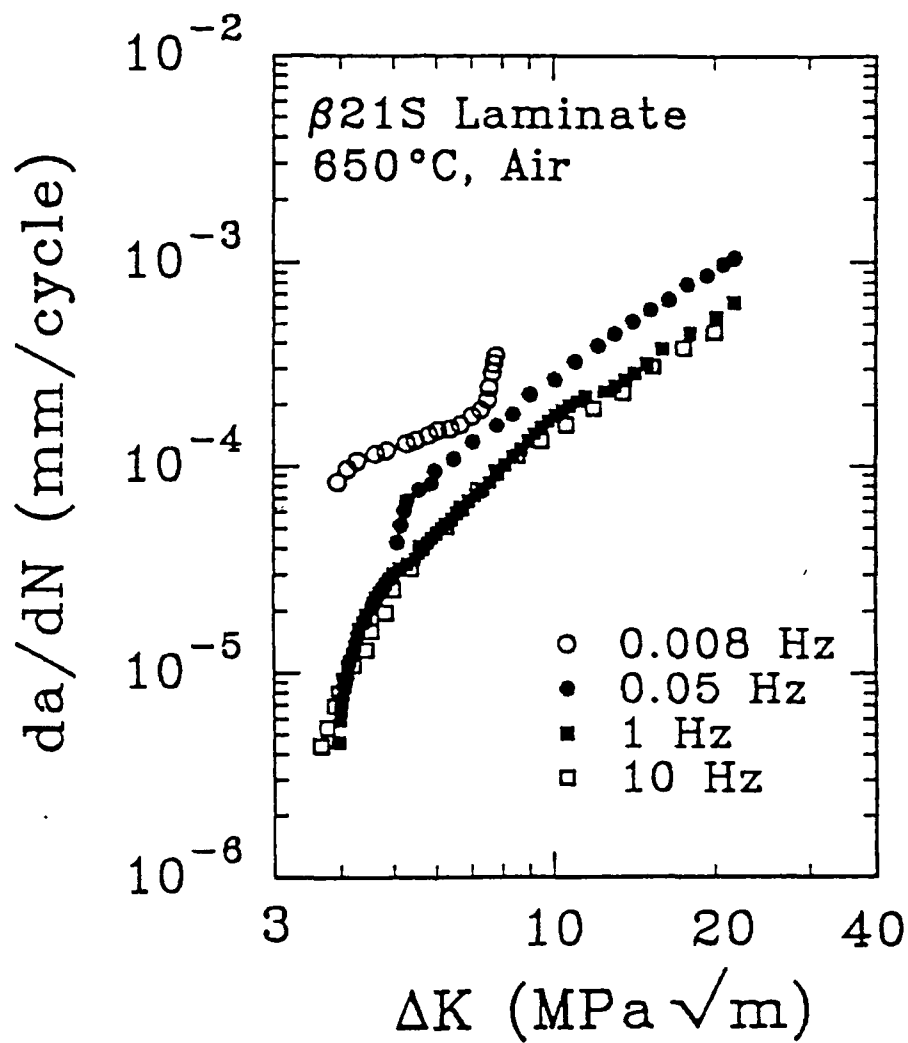


Fig. 1-9

Effects of loading frequency on fatigue crack growth rates in Timetal®21S monolithic laminate at 650°C.

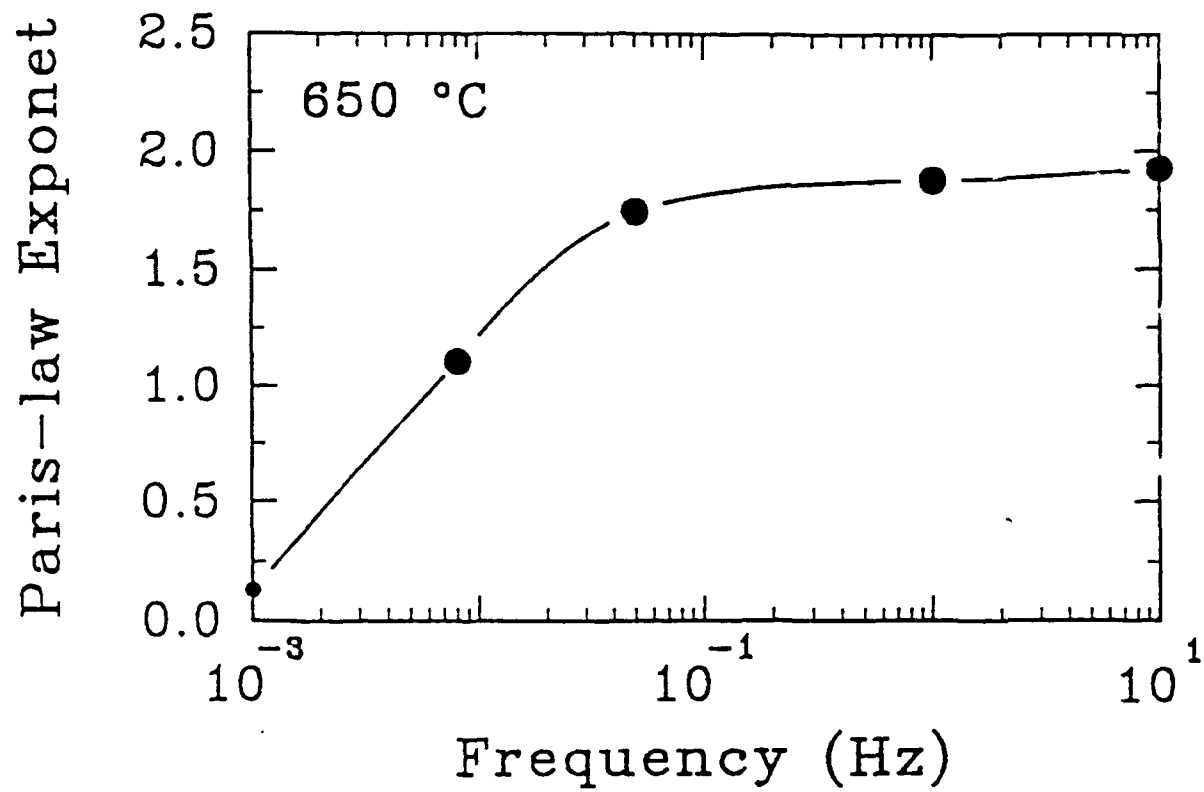


Fig. 1-10

Relationship between Paris law exponent and loading frequency.

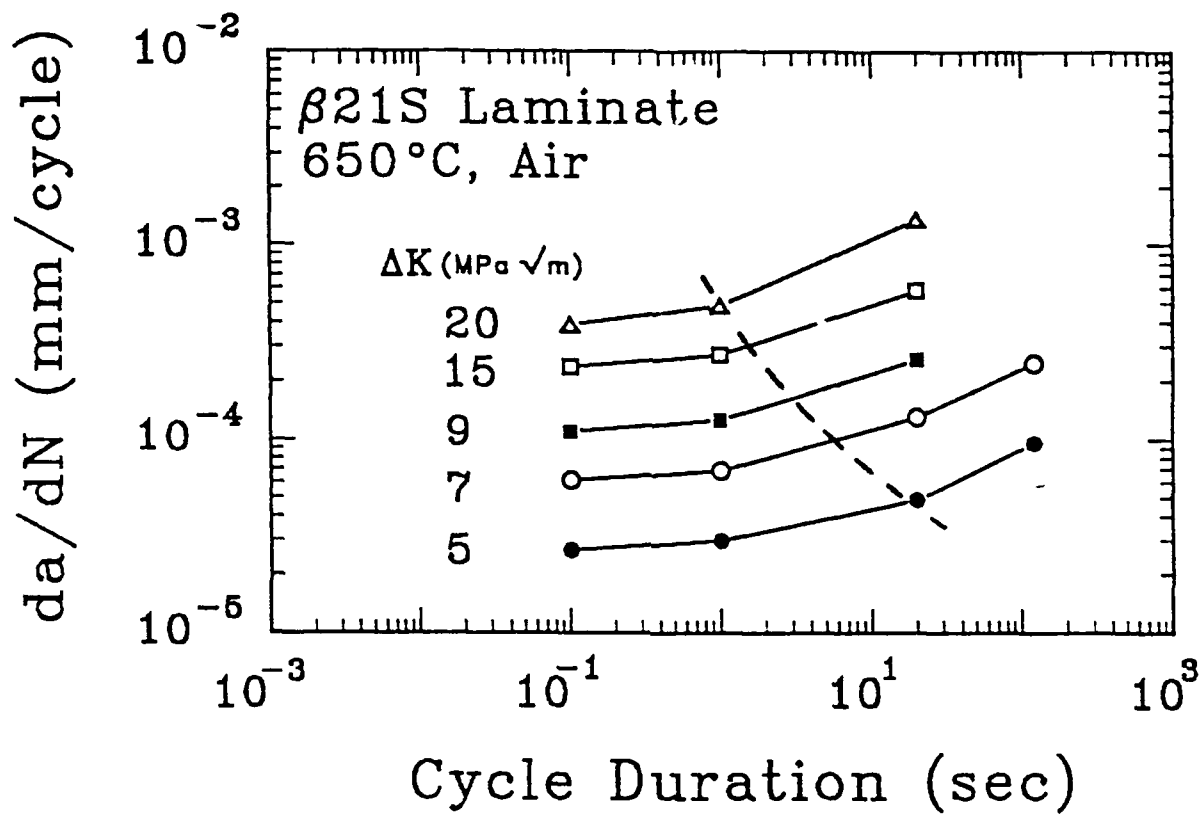


Fig. 1-11 Relationship between crack growth rate and loading cycle duration as function of ΔK .

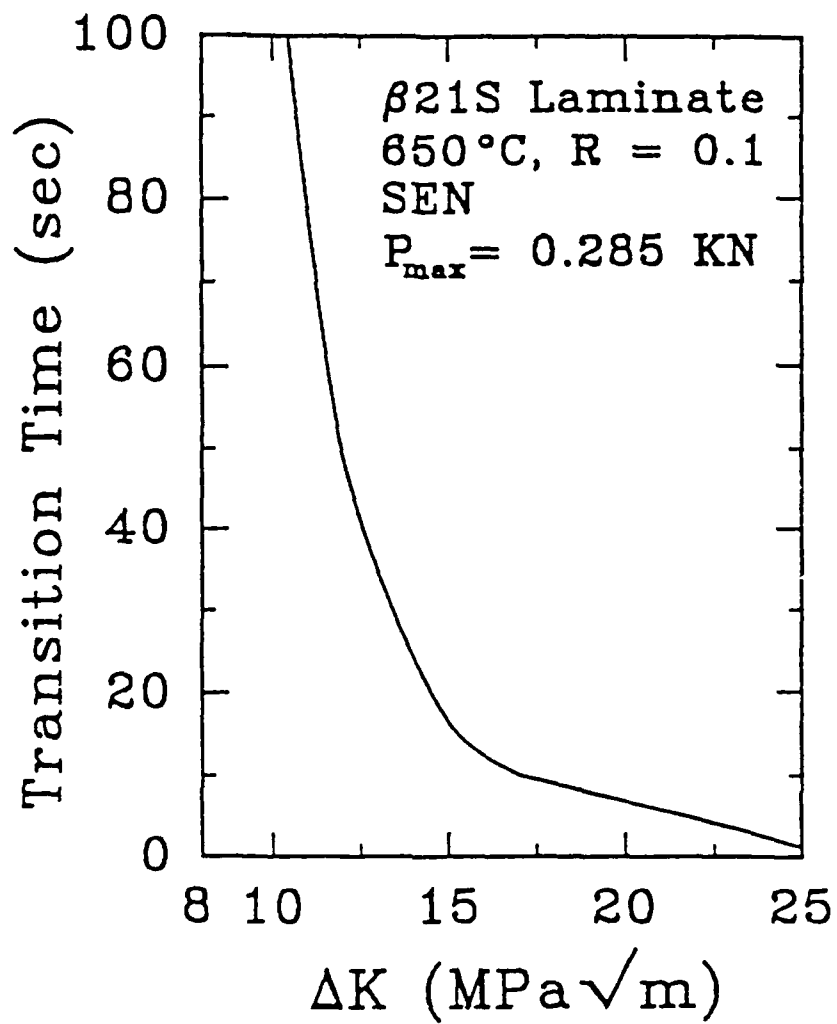


Fig. 1-12 Transition time from small scale yielding to secondary creep as a function of ΔK level at 650°C.



Fig. 1-13 Typical fracture surface features of Timetal®21S monolithic laminate at 650°C, 0.05 Hz.

SECTION 2

THERMAL RESIDUAL STRESS IN TITANIUM METAL MATRIX COMPOSITES²

ABSTRACT

A new experimental approach designed to determine the axial thermal residual stress in the matrix of the continuously reinforced metal matrix composite is described in this section. This approach is based on the stress-strain expression in terms of the fiber thermal and mechanical properties as well as the volume fractions of the composite constituents. This expression is then incorporated into an experimental procedure in which a composite specimen is simulated by a fiberless titanium laminate plate gripped under load control across the frame of a hydraulic material testing system. The strain developed in the laminate specimen during heating or cooling is governed by the strain compatibility requirement imposed by the fiber phase which is represented by the testing frame. This restricted matrix strain is converted through a feedback logic into a matrix residual stress that could be followed on real time basis. The magnitude of the thermal residual stress measured at room temperature for SCS-6/Ti-15-3 composite after the cool-down from consolidation temperature has been compared with that obtained by the X-ray diffraction technique. The proposed technique was then applied to SCS-6/Timetal 21S composite yielding measurements of the matrix thermal residual stress as a function of several testing variables such as temperature, heating/cooling rate, thermal cycle upper limit and number of thermal cycles. Important features of the matrix axial thermal residual stress have been analyzed. The major conclusion of this analysis is that the development of the thermal residual stress is a cooling rate dependent while the relaxation of this stress depends on the magnitude of the viscoplastic strain generated in the matrix material at a particular testing condition.

2.1 INTRODUCTION

Fiber reinforced metal matrix composites (FRMMCs) generally consist of materials with different coefficients of thermal expansion (CTE) between the matrix and the reinforcing phase. Because of this difference, upon consolidation at high temperature, which may exceed 1000°C in the case of Ti-base MMC fabrication, and during cool-down from this strain-free temperature to room temperature, appreciable locked-in residual thermal stresses are formed in both the matrix and the reinforcing phase. These residual stresses can be detrimental as well as beneficial. The detrimental aspects are associated with a variety of damage types produced in the matrix material. For example, in the case of SCS-6/Ti-24Al-11Nb (at%) composite, the thermally induced effective residual stress exceeds the matrix yield stress at temperatures below 500°C and

² based on "Thermal residual stress in titanium metal matrix composites", H. Ghonem, Y. Wen and D. Zheng, Materials Science and Engineering, in press, 1993.

as such the matrix undergoes plastic deformation [1]. While in the case of SCS-6/Ti-24Al-11Nb [2] and SCS-6/Ti-15-3 [3] composites the residual hoop stresses are reported to be large enough to generate radial cracks at the fiber/matrix interface during cooling from the consolidation temperature. For the SCS-6/Ti-25-10-3-1Mo composite during cool-down from 927°C, multiple circumferential cracks were observed in matrix near fiber/matrix interfacial region [4]. From the beneficial viewpoint, the compressive radial stress at the interface acts to clamp the matrix around the fiber. This clamping effect plays a significant role in the fiber/matrix load transfer process. This is particularly important for the situation where debonding and slippage occurred between the matrix and fibers. In fact, for some composite systems, such as SCS-6/Ti-15-3, where the fiber/matrix chemical bonding is weak [5,6], the compressive residual radial stress friction provides the frictional force which is the critical means of achieving load transfer. For the axial residual stress, it is generally believed that this kind of residual stress superimpose directly on the applied stress in both the fiber and matrix material. However, recent studies showed that the axial residual stress has definite influences on debonding and fiber bridging processes [7-11]. For a bonded interface, the applied axial stress on the fiber required to debond the interface is modified by the presence of the residual axial stress. When the interfacial shear stresses induced by the residual axial stress and by the applied axial stress are in the same direction, the existence of the axial residual stress facilitates debonding process. When they are in opposite directions, interfacial debonding is inhibited by the axial residual stress. While for a partially debonded interface the axial residual stress influences the boundary condition at the end of debonding which, in turn, modifies the stress distribution in the debonded region [7,8]. In this region, the axial residual stress also influences the opening of matrix cracks [9,12], which will decrease or increase the bridging traction in the fiber thus modifies the driving force at crack tip. In this sense, axial residual stress can also affect the damage mode of the composite and plays a role as important as the radial residual stress.

Thus, the study of the residual stress distribution and its evolution in composite systems is important in the understanding of its role in the load transfer efficiency within the composite as well as in its influence on the damage mode and the damage location in relation to the composite constituents. These aspects are crucial in the process development and the structural design of composites. Many investigations have been made to calculate and/or measure these thermal residual stresses, see [1,4,13-22]. On the experimental side, the two frequently used nondestructive techniques for measuring residual stresses in composites are the X-ray diffraction method [15,23-25] and the neutron powder diffraction method [1,18,20,26,27]. The X-ray techniques have a wider application since the equipment is easier to access and well developed. However, the shallow beam penetration (a few microns) precludes clear volume sampling and thus X-ray measurement can only provide a near-surface residual stress field. While neutron diffraction techniques require a radiation source that is only available in a small number of laboratories, they offer unique advantages in determining the residual stresses within the cross section of the specimen owing to the deep penetration of the neutron beam; about 1000 times deeper than that of X-rays [18,20]. This deeper penetration provides an excellent volume sample thus providing a relative true bulk measurement of residual strains independent from surface-related effects. Furthermore, deeper penetration produces the ability to simultaneously measure the residual strains parallel and perpendicular to the fiber in both fiber and matrix. The important common feature between X-ray and neutron diffraction techniques is the time required for each

point of stress measurement. For X-rays, the sampling time at each measurement varies from 5 to 40 minutes [28,29] while for neutrons it requires about 2 hours [28,30]. This time requirement while acceptable for measurements at room temperature, represents a problem for those to be obtained at elevated temperature conditions or during cooling from consolidation temperature. This is due to the fact that a rapid stress relaxation could take place when attempts are made to hold the temperature for long durations while diffraction count is being made. This basic difficulty in tracing the evolution of residual stresses without introducing time dependent alteration in their magnitudes is the motivation to develop a real-time mechanical simulation technique which will be described in this section. This technique is a one-dimensional approach which focuses on the determination of the axial thermal stress in the matrix material during temperature variation in processes such as cool-down from fabrication temperature to room temperature or thermal cycling with or without externally applied load. As mentioned above, the axial thermal residual stress plays an important role in influencing the damage process of continuous fiber composites. Thus, the comprehensive knowledge of the axial thermal stress evolution will be expected to shed light on the understanding of the damage mechanisms and the corresponding mechanical behavior of the composite systems. Although the proposed technique can not provide direct estimation of the hoop and radial stresses, it could, however, since uniqueness exists between axial, hoop and radial stresses in the matrix and fiber components of the FRMMC, when combined with a numerical method tuned by the data from this technique, provide enough information to establish the required three-dimensional stress state. The theory and the concepts of this mechanical simulation method will be presented in the next two sections. This will be followed by a description of material and experimental procedure as well as a discussion of experimental results.

2.2 THEORY

In this section, the equations required to estimate the matrix thermal stresses on the basis of the knowledge of the total matrix strain and the thermal characteristics of the fiber will be derived. A simplification will then be made so that the three-dimensional analysis reduces to the case where the axial component of the stress vector is determined through a one-dimensional equation. This equation is related to the total matrix strain and the CTE of the fiber and, as will be discussed later, is the key for the mechanical simulation method proposed in this section.

For a unidirectional fiber reinforced metal matrix composite under the axial loading conditions, the composite is assumed to undergo axisymmetric deformation. Based on a representative unit cell analysis the stresses in the composite constituents are described by the following equilibrium equations:

$$\sigma_r^c = \frac{r_f}{2r_m} \sigma_r^f + \frac{r}{2r_m} \sigma_r^m \quad (12)$$

$$\sigma_r^c = V_f \sigma_\theta^f + V_m \sigma_\theta^m$$

$$\sigma_z^c = V_f \sigma_z^f + V_m \sigma_z^m$$

where the superscripts c, f and m represent composite, fiber and matrix, respectively, and the subscripts r, θ and z represent radial, hoop and axial directions, respectively. V_f is the volume fractions of the fiber and V_m is the volume fraction of the matrix. r_f is the radius of the fiber, r_m is a radius of the representative unit cell. By defining the overall composite stress vector $\bar{\sigma}^c$, the fiber stress vector $\bar{\sigma}^f$ and the matrix stress vector $\bar{\sigma}^m$, eq. (1) can then be written as the following matrix form:

$$\bar{\sigma}^c = A_f \bar{\sigma}^f + A_m \bar{\sigma}^m \quad (13)$$

In the axisymmetric deformation condition, the strains within the constituent of the composite must satisfy the following compatibility relationships

$$\begin{aligned} \epsilon_r^c &= V_f \epsilon_r^f + V_m \epsilon_r^m \\ \epsilon_\theta^c &= \epsilon_\theta^f = \epsilon_\theta^m \\ \epsilon_z^c &= \epsilon_z^f = \epsilon_z^m \end{aligned} \quad (14)$$

here, the superscripts and the subscripts have the same meanings as in eq. (1). If ϵ_θ^c and ϵ_z^c are expressed as $\epsilon_\theta^c = (\epsilon_\theta^f + \epsilon_\theta^m) / 2$ and $\epsilon_z^c = (\epsilon_z^f + \epsilon_z^m) / 2$, respectively, and defining the overall strain vectors $\bar{\epsilon}^c$, the fiber strain vector $\bar{\epsilon}^f$ and the matrix strain vector $\bar{\epsilon}^m$ then eq. (3) can be written in the following form:

$$\bar{\epsilon}^c = B_f \bar{\epsilon}^f + B_m \bar{\epsilon}^m \quad (15)$$

In the matrix, the total strain, $\bar{\epsilon}^m$, can be considered as the sum of the mechanical strain, $\bar{\epsilon}^{m,me}$, and the thermal strain, $\bar{\epsilon}^{m,th}$ of the matrix, i.e.

$$\bar{\epsilon}^m = \bar{\epsilon}^{m,me} + \bar{\epsilon}^{m,th} \quad (16)$$

the matrix thermal strain, $\bar{\epsilon}^{m,th}$, can be calculated as

$$\bar{\epsilon}^{m,th} = \int_{T_0}^T \bar{\alpha}^m(T') dT' \quad (17)$$

where T_0 is the reference temperature, T is the temperature, $\bar{\alpha}^m(T)$ is the CTE vector of the matrix; $\bar{\alpha}^m(T) = (\alpha_r^m(T), \alpha_\theta^m(T), \alpha_z^m(T))^T$. The mechanical strain, $\bar{\epsilon}^{m,me}$, consists of an elastic component, $\bar{\epsilon}^{m,e}$, and an inelastic component, $\bar{\epsilon}^{m,in}$, summed as follows:

$$\bar{\epsilon}^{m,me} = \bar{\epsilon}^{m,e} + \bar{\epsilon}^{m,in} \quad (18)$$

the elastic component, $\bar{\epsilon}^{m,e}$, can be obtained from the the following relationship:

$$\bar{\epsilon}^{m,e} = S_m \bar{\sigma}^m \quad (19)$$

where S_m is the compliance matrix of the matrix material. The inelastic component, $\bar{\epsilon}^{m,in}$, generally consists of a time-independent plastic part, $\bar{\epsilon}^{m,p}$, and a time-dependent viscous flow part, $\bar{\epsilon}^{m,vis}(t)$:

$$\bar{\epsilon}^{m,in} = \bar{\epsilon}^{m,p} + \bar{\epsilon}^{m,vis}(t) \quad (20)$$

$\bar{\epsilon}^{m,vis}(t)$, is, generally, composed of an anelastic recoverable component, $\bar{\epsilon}^{m,visa}(t)$, and a viscoplastic component, $\bar{\epsilon}^{m,visp}(t)$:

$$\bar{\epsilon}^{m,vis}(t) = \bar{\epsilon}^{m,visa}(t) + \bar{\epsilon}^{m,visp}(t) \quad (21)$$

Thus, the total strain of the matrix could be written in the terms of its individual components as:

$$\bar{\epsilon}^m = \bar{\epsilon}^{m,e} + \bar{\epsilon}^{m,p} + \bar{\epsilon}^{m,visa}(t) + \bar{\epsilon}^{m,visp}(t) + \bar{\epsilon}^{m,th} \quad (22)$$

Turning attention to the fiber, it is assumed to be made of a noncreeping material and undergoes elastic deformation only. This assumption is suitable to most of SiC/Ti MMC composites at operating temperatures below 1000°C. In this case, the mechanical strain of the fiber, $\bar{\epsilon}^{f,me}$, equals the elastic strain of the fiber, $\bar{\epsilon}^{f,e}$, thus, the total strain of the fiber, $\bar{\epsilon}^f$, can be expressed as a sum of elastic and thermal components as follows:

$$\bar{\epsilon}^f = \bar{\epsilon}^{f,e} + \bar{\epsilon}^{f,th} \quad (23)$$

where the elastic strain, $\bar{\epsilon}^{f,e}$, and the thermal strain, $\bar{\epsilon}^{f,th}$, can be evaluated as follows:

$$\bar{\epsilon}^{f,e} = S_f \bar{\sigma}^f \quad (24)$$

and

$$\bar{\epsilon}^{f,th} = \int_{T_0}^T \bar{\alpha}^f(T') dT' \quad (25)$$

where S_f is the compliance matrix of the fiber, $\bar{\sigma}^f$ is the fiber stress and $\bar{\alpha}^f(T)$ is the CTE vector of the fiber, $\bar{\alpha}^f(T) = (\alpha_1(T), \alpha_2(T), \alpha_3(T))^T$. Now, by combining eqs. (4), (12)-(14), $\bar{\sigma}^f$, can be expressed as

$$\bar{\sigma}^f = C_f \left[B_f^{-1} (\bar{\epsilon}^c - B_m \bar{\epsilon}^m) - \int_{T_0}^T \bar{\alpha}^f(T') dT' \right] \quad (26)$$

where C_f is the stiffness matrix of the fiber. Furthermore, substituting (15) in (2), the matrix stress, $\bar{\sigma}^m$, is obtained as

$$\bar{\sigma}^m = A_m^{-1} \left\{ \bar{\sigma}^c - A_f C_f \left[\bar{\epsilon}^f - \int_{T_0}^T \bar{\alpha}^f(T') dT' \right] \right\} \quad (27)$$

For thermal loadings where no external mechanical load is applied, i.e. $\bar{\sigma}^c = 0$, eq. (14) can be reduced to

$$\bar{\sigma}^m = H \left[\int_{T_c}^T \bar{\alpha}^f(T') dT' - \bar{\epsilon}^f \right] \quad (28)$$

where $H = A_m^{-1} A_f C_f$.

Eq. (17) indicates that the matrix stress state at certain temperature can be determined as long as the fiber strain state at same temperature is known. It should be noticed that the matrix stress state obtained from eq. (17) corresponds to the situation where the matrix could undergo any combinations of elastic, plastic and viscous deformation. While in the usual diffraction methods (X-ray or neutron diffractions), the stress analysis basically relies on the Hook's law which only corresponds to the elastic deformation [27,31]. If, for the first approximation, the Poisson effect of the fiber is neglected, eq. (17) could then be decoupled and the z-component of the matrix stress vector, $\bar{\sigma}^m$, can be written as

$$\sigma_z^m = \frac{V_f E_f}{V_m} \left(\int_{T_c}^T \alpha_z^f(T') dT' - \epsilon_z^m \right) \quad (29)$$

The mechanical simulation method developed in this study to examine the evolution of the thermal axial stress in matrix is based on the use of eq. (18).

2.3 MECHANICAL SIMULATION METHOD

It is known that as the temperature of a portion of composite material changes, both fiber and matrix materials tend to deform according to their respective CTE. However, the existence of the significant CTE difference and the fiber/matrix bond require the strain compatibility between the two composite phases, consequently the stress and the strain will be developed in the matrix and the fibers in order to accommodate the thermal mismatch. In order to illustrate the concept of the proposed approach, the composite is idealized as a one dimensional two-bar model representing the fiber and the matrix constituents, as schematically detailed in Fig. 2-1. Also, during post-fabrication cool down and subsequent thermal cycling, the cooling/heating path is viewed as being piecewise discretized into steps consisting of an instantaneous temperature increment, ΔT , followed by a time increment, Δt , as illustrated in Fig. 2-2. For a particular time/temperature step, the elastic-plastic response and creep response are considered as a summation of the elastic-plastic response due to ΔT and the creep response occurring during Δt .

The stress-state of the composite is assumed to be stress-free at the consolidation temperature, T_c , as shown in Fig. 2-3(a). When the composite cools down an increment of ΔT from the consolidation temperature, the matrix and fiber will attempt to contract freely by a strain amount of $\Delta \epsilon_z^{i,0}$ ($i = f$ for fiber and $i = m$ for matrix), as if no constraint or bond existed between the fiber and the matrix. In reality, however, constraint does exist (assuming a perfect fiber/matrix bonding) and the requirement for isostrain must be satisfied across the fiber/matrix interface. In response to this restriction, the matrix will act as if it is elongated from its constraint-free length with a tensile mechanical strain, $\Delta \epsilon_z^{m,me}$, and the fiber will be as if compressed from its constraint-free length, with a compressive mechanical strain, $\Delta \epsilon_z^{f,me}$, see Fig. 2-3(b). Accompanying these strains, a residual tensile stress, $\Delta \sigma_z^m$, is induced in the matrix while

a residual compressive stress, $\Delta\sigma_z^f$, is induced in the fiber, as illustrated in Fig. 2-3(c). The significance of $\Delta\sigma_z^m$ is in its ability to generate a tensile inelastic strain component in the matrix. It is assumed here that the fiber does not develop significant plastic or creep strain. Therefore, the net axial stress developed in the matrix, $\Delta\sigma_z^m$, is the sum of a tensile stress component generated by the restriction imposed on the thermal contraction of the matrix and the stress relaxation due to the restricted creep flow in the matrix. Similarly, the matrix total strain, $\Delta\epsilon_z^m$, at the end of the first cool-down step is calculated as the sum of the thermal strain component (due to ΔT) and an inelastic strain component (due to Δt). At the end of the first cool-down step, a unique correlation can be established between the matrix total axial strain, $\Delta\epsilon_z^m$, and the matrix axial stress, $\Delta\sigma_z^m$, via the thermal and elastic properties of the reinforced fiber. This relationship takes the form of eq. (18) which is rewritten as:

$$\Delta\sigma_z^m = \frac{V_f E_f}{V_m} \left(\int_{T_c}^{T_c - \Delta T} \alpha_z^f(T') dT' - \Delta\epsilon_z^m \right) \quad (30)$$

where T_c represents the consolidation temperature and all other parameters are as previously defined.

The concepts discussed above are identical for subsequent cool-down steps and hence the values of $\Delta\epsilon_z^m$ and $\Delta\sigma_z^m$ at the end of each ΔT step can be determined. The thermal residual stress and strain evolution in the matrix phase of a composite during cool-down from consolidation and/or subsequent thermal cycling, can then be fully traced and described.

This notion can be exploited experimentally as follows: a fiberless (neat) titanium laminate specimen is gripped under load-control in a hydraulic testing frame with data acquisition and feedback capabilities. In this arrangement, the laminate specimen assumes the role of the composite matrix, while the actuator of the testing frame assumes the role of the composite fiber, as schematically illustrated in Fig. 2-4. The initial stress-free condition is then simulated by raising the temperature of the laminate specimen to the consolidation temperature with zero applied load, so that both the specimen (matrix) and the loading frame (fiber) are stress-free. A high-temperature strain extensometer attached to the specimen gage length is also set to zero strain level. On reducing the temperature from T_c for a finite temperature step ΔT , thermal strain is induced in the laminate specimen (at this moment, the system is still stress-free, since the test machine is at zero load-control). This thermal strain, $(\Delta\epsilon_z^m)_1$, measured by the extensometer, is fed into eq. (19) in order to estimate the corresponding $(\Delta\sigma_z^m)_1$ which would exist in the matrix if it were constrained by the fiber/matrix bond. This calculated matrix stress is then applied to the specimen via the load frame (fiber). However, the strain in the specimen (as measured by the extensometer) will change to $(\Delta\epsilon_z^m)_2$ in response to this applied stress, and the new matrix strain, being a combination of thermal and mechanical strains, is input back to eq. (19) and a new matrix stress is calculated and then applied to the specimen. This iterative process continues until the convergence occurs during the period Δt (Δt duration defines the cooling rate for this specific cool down process) as illustrated in Fig 5. The converged values of $(\Delta\epsilon_z^m)_n$ and $(\Delta\sigma_z^m)_n$ are therefore considered to be the thermal residual stress and strain states corresponding to the temperature $T_c - \Delta T$ and the certain cooling rate. It should be emphasized that the measured matrix strain, $(\Delta\epsilon_z^m)_i$; $i = 1, 2, \dots, n$, includes any creep strain component that may develop due to the

loading of the matrix. As this process is repeated for additional decrements in temperature, the matrix thermal residual stress and strain history as a function of temperature could be established.

2.4 MATERIAL AND EXPERIMENTAL PROCEDURE

Two metastable β titanium alloys were used as matrix materials, Timetal 21S and Ti-15-3. The chemical composition of β 21S (in wt%) is: 0.1 Fe, 16.0 Mo, 3.06 Al, 2.9 Nb, 0.2 Si, 0.22 C, 0.12 O, 0.005 N with the balance being Ti. The microstructure of the heat treated alloy consists of distinctive β grains with an average size of 80 μm containing Widmanstätten acicular α phase and continuous grain boundary α material with the thickness of about 0.8 μm . Laminates were fabricated by consolidating eight foils using vacuum hot pressing employing pre-established critical processing parameters. The Ti-15-3 alloy has the following nominal composition (in wt%): 14-16 V, 2.5-3.5 Cr, 2.5-3.5 Al, 2.5-3.5 Sn, < 0.05 C, < 0.05 Ni, < 0.15 O and < 0.015 H with the balance being Ti. The Ti-15-3 matrix was also supplied in 8 ply monolithic laminate. The fiber mechanical and thermal properties simulated in this study were those of the SCS-6 fiber. The fiber volume fraction utilized here for both Ti-15-3 and Timetal 21S composites was assumed to be 35%.

Table 2.1 Test Conditions

Test Condition	Cooling/Heating Rate ($^{\circ}\text{C}$)	Thermal Cyclic Range ($^{\circ}\text{C}$)	Material
A	0.5	100-550	Timetal 21S
B	0.5	100-650	Timetal 21S
C	0.05	100-575	Timetal 21S
D	0.05	—	Ti-15-3

Four Timetal 21S and one Ti-15-3 laminate strips were used in this study. The dimension of the test specimens were 76.5mm x 7.25mm x 0.85mm with the gage length measuring 40mm. All tests were carried out using an automated servo-hydraulic test frame. Test specimens were gripped using a hydraulic flat grip with self aligning capabilities and heated with an open furnace utilizing infrared radiation lamps. In all tests, heating from room temperature to the consolidation level was achieved using a heating rate of 0.05 $^{\circ}\text{C}/\text{sec}$ under the stress-free condition. The consolidation temperature was taken as 871 $^{\circ}\text{C}$, and 900 $^{\circ}\text{C}$ for the Timetal 21S and Ti-15-3 matrices, respectively. Tests after that were conducted using two different cooling/heating rates 0.5 $^{\circ}\text{C}/\text{sec}$ and 0.05 $^{\circ}\text{C}/\text{sec}$. Several specimens of the Timetal 21S material were subjected to thermal reversals between 100 $^{\circ}\text{C}$ and three different upper temperatures; 525 $^{\circ}\text{C}$, 575 $^{\circ}\text{C}$ and 650 $^{\circ}\text{C}$. The variation of the temperature along the gage length during all tests was $\pm 3^{\circ}\text{C}$. All

test conditions are listed in Table 2.1.

2.5 RESULTS, ANALYSIS AND DISCUSSION

As mentioned before, the focus of this study is the evolution characteristics of the axial thermal residual stress in the Timetal 21S matrix material. However, for the absence of data in literature regarding the Timetal 21S material, the Ti-15-3 laminate was also used in order to compare the results using the proposed simulation technique with the limited Ti-15-3 data available in literature (e.g. see [32]).

The axial thermal residual stress profiles in Ti-15-3 and Timetal 21S matrix materials are shown in Figs. 2-6 ~ 2-8 for different cooling rates. These profiles were obtained by simulating the thermal response of composite systems in which the properties of SCS-6 fiber were used. Fig. 2-6 shows the stress profile corresponding to the Ti-15-3 during cool-down from consolidation temperature to room temperature with a cooling rate of $0.05^{\circ}\text{C}/\text{sec}$. From this figure, the stress level achieved at room temperature is 198 MPa. This result could be compared with that obtained by Cox et al [32] using the X-ray diffraction technique. Their work showed that the axial residual stress at room temperature in SCS-6/Ti-15-3 composite has the value of 130 ± 30 . While the results of the two studies are close, the difference could be due to the fact that the work of Cox et al [32] may have been carried out on as received specimens that are generally cooled from the consolidation temperature using a natural cooling rate which is lower than any of the rates used in this study. In addition, while the X-ray diffraction provides surface stress measurements, the proposed technique provides an average bulk stress. It should be mentioned here that the calculated results by Mall et al [33] for the axial residual stress in the Ti-15-3 matrix is 81 MPa which is lower than the experimental result discussed above. The possible reason for this lower value is that the viscoplastic response of the matrix material which dominates the final stress state is too complex to be described accurately in constitutive laws used in the current numerical models.

Turning attention to the Timetal 21S matrix material, the axial thermal residual stresses, σ_z^m , generated in the SCS-6/Timetal 21S composite system during the cool-down from the consolidation temperature to room temperature are shown in Figs. 2-7 and 2-8 for two different cooling rates: a fast cooling rate, $0.5^{\circ}\text{C}/\text{sec}$, and an equivalent to a natural cooling rate, $0.05^{\circ}\text{C}/\text{sec}$. For all those tests, neither surface cracks nor interior damage were found. These figures also show the residual stress during subsequent thermal cycles reversing between 100°C and two high temperature levels: 550°C and 575°C . The analysis will focus first on the thermal residual stress developed during the first cool-down. Here, it is observed that σ_z^m is cooling-rate dependent: the higher the cooling rate, the lower the thermal residual stress. This is valid for the entire cool-down range. Furthermore, the stress build-up as a function of the decreasing temperature rate is also cool-rate dependent. It is also observed that two distinct stages exist during the cool-down duration. In the first stage, the built-up stress is small and rises with a small $d\sigma/dT$ value. This trend ends at a certain transition temperature and a new stage begins where both the magnitude of the thermal residual stress and $d\sigma/dT$ show higher values than those in the previous stage. The transition between these two stages in the case of the $0.5^{\circ}\text{C}/\text{sec}$ testing occurred at about 750°C while in the case of $0.05^{\circ}\text{C}/\text{sec}$, this transition is delayed and occurred

at about 600°C. It is important to notice here that the $d\sigma/dT$ in the second stage is higher in the 0.05°C/sec case than that of the 0.5°C/sec case.

Two important points should be mentioned here. The first is the fact that σ_z^m during the cool-down process of the two simulated composites used in this study has always been lower than the yield stress, σ_{ys}^m of the matrix material. If one assumes that σ_r^m , σ_θ^m and σ_z^m are related as follows [1]: $|\sigma_r^m| \leq \sigma_z^m$ and $|\sigma_\theta^m - \sigma_z^m| = \sigma_z^m / 2$, the corresponding equivalent stress, σ_{eq}^m , could then be calculated. In this case σ_{eq}^m is found to be always less than the yield stress levels [34,35] of the Ti-15-3 and Timetal 21S monolithic laminates. This indicates that no plastic deformation took place in the matrix material during the cool-down process. The second point to be addressed is that all specimens have been subjected to post test optical microscope analysis which showed that no surface microcracking has developed during the cool-down process in both material. Recognizing these two facts, an attempt will be made here to interpret the observations described above on the basis of the inelastic behavior of the matrix material and the deformation constraints imposed by the matrix/fiber strain compatibility requirement. First, we will deal with the existence of two distinctive stages in the σ -T relationship. At the onset of the cool-down process, the inelastic strain of the matrix material, $\epsilon_z^{m,in}$, for a particular net stress level, σ_z^m , and during a time interval, t , can be described using the Bailey-Norton type equation which is written as

$$\epsilon_z^{m,in} = B(\sigma_z^m)^n t^\alpha \quad (31)$$

where n and α are material constants, and B takes the Arrhenius form:

$$B = A \exp\left(-\frac{Q}{RT}\right) \quad (32)$$

A is a constant, R is the gas constant and T is the temperature in Kelvin. Q is the thermal activation energy of the stressed material, it is written as a function of the inelastic strain accumulated in the material $f(\epsilon_z^{m,in})$ [36]:

$$Q = Q_0 - f(\epsilon_z^{m,in}) \quad (33)$$

where Q_0 is the thermal activation energy of the unstressed material. Since the magnitude of residual stress is small in the early stage of the cool-down, it could then be suggested that the development of the inelastic strain and the corresponding compressive stress component, which leads to the decrease in the net axial residual stress, is primarily governed by temperature through the parameter B . In the second stage of cool-down below the transition temperature, where B is small, the development of the inelastic strain becomes more sensitive to the magnitude of σ_z^m . In this stage therefore, at a certain temperature and for the same time duration, the net inelastic strain in the 0.5 C°/sec test should be higher than that occurring in the 0.05C°/sec case. Consequently, the net residual stress corresponding to the former condition should, as experimentally observed, be lower than that of the later condition. Furthermore, the existence of a difference in the transition temperature between the two stages for the two different cooling rates could be explained on the basis that the function $f(\epsilon_z^{m,in})$ in eq.(22) should have a higher value in the case of the lower cooling rate testing due to the higher accumulated inelastic strain. Therefore, the thermal activation energy, Q , in the case of the lower cooling rate would maintain

a relatively lower value (thus higher creep strain) at lower temperature levels, which signifies a transition temperature lower than that corresponding to the high cooling rate testing.

The second part of the analysis focuses on the evolution of the axial residual stress profile during the thermal cycles following the first cool-down process. These profiles obtained for different temperature ranges and different heating/cooling rates are shown in Figs. 2-7 and 2-8. The general observation here is that at any temperature within the cycle range, thermal reversals tend to reduce the axial thermal residual stress. Furthermore, the stress relaxation towards the zero level seems to increase as both the upper limit of the cycle temperature range and the cooling/heating rate increase. It is also observed that the decrease in the axial thermal residual stress follows an almost linear path parallel to its increase during the cool-down part of the preceding cycle. On reaching a transitional temperature, this path deviates from linearity with an increasing negative $d\sigma/dT$ slope as temperature increases. This behavior could be interpreted in terms of the relative influence of temperature on the development of viscous flow in the matrix material. At low temperature levels the magnitude of viscous flow is negligible and the thermal elastic unloading of the stress dominates. As the temperature increases, the influence of viscous flow becomes important resulting in a higher compressive stress component which leads to a rapid decrease of the matrix residual stress. The temperature at which this acceleration in the stress reduction takes place was found to decrease as the number of thermal reversals increases, see dotted lines in Fig. 2-7. This temperature was also observed to depend on the heating-rate. This may be due to the fact that lower heating rate permit sufficient time for the development of viscous flow which in turn leads to a drop in the stress level at temperatures lower than that required to achieve the same drop in the case of high heating rate.

The role of the matrix viscous flow can further be examined by exploring the relationship between the inelastic strain, $\epsilon_z^{m, in}$ and the axial thermal residual stress, σ_z^m . Since no matrix plastic deformation is realized during the thermal history of all tests carried out on the SCS-6/Timetal 21S composite, the inelastic strain $\epsilon_z^{m, in}$ could be written as

$$\begin{aligned}\epsilon_z^{m, in} &= \epsilon_z^{m, visa}(t) + \epsilon_z^{m, visp}(t) \\ &= \epsilon_z^m - \int_{T_0}^T \alpha_z^m(T') dT' - \epsilon_z^{m, e}\end{aligned}\quad (34)$$

All terms being identified previously. ϵ_z^m could be replaced using eq.(18) and the relationship between $\epsilon_z^{m, in}$ and σ_z^m is established as:

$$\epsilon_z^{m, in} = \int_{T_0}^T (\alpha_z^f(T') - \alpha_z^m(T')) dT' - \frac{V_m}{V_f E_f} \sigma_z^m - \epsilon_z^{m, e} \quad (35)$$

This relationship between $\epsilon_z^{m, in}$ and σ_z^m for the test condition A is plotted in Fig. 2-9. It is seen here that for the same temperature level and at a particular thermal cycle, the value of $d\sigma/d\epsilon$ increases as the temperature range of the thermal reversal increases. The increase in the slope $d\sigma/d\epsilon$ means that the viscoplastic part of the inelastic strain in this particular cycle has increased thus permitting, opposite to the role of anelastic recoverable strain, unrecoverable drop in the residual stress level. Higher upper temperature limit of the thermal cycle and lower cooling/heating rates are favorable conditions for the promotion of viscoplastic strain.

Additionally, the ability to accumulate inelastic strains during thermal cycles could be determined by defining a strain hardening parameter, κ , as:

$$\kappa = \frac{d\sigma_z^m}{d\epsilon_z^{m,in}} \quad (36)$$

This parameter was measured along isothermal lines (slanted lines in Fig. 2-9) for different temperature levels. The strain hardening parameter, κ , in terms of number of thermal cycles is shown in Fig. 2-10. It is apparent that κ decreases as number of cycles increases. This softening characteristic is proportional to both the increase in the upper temperature limit of the thermal cycle and the decrease in heating/cooling rates.

2.6 CONCLUSIONS

A new experimental approach designed to determine the axial thermal residual stress in the matrix of the continuously reinforced metal matrix composite is described in this section. Using this technique, the magnitude of the thermal residual stress measured at room temperature for SCS-6/Ti-15-3 composite after the cool-down from consolidation temperature has compared well with that obtained by the X-ray diffraction technique, taking into consideration the difference in the fundamental nature between the two techniques. The proposed technique was then applied to SCS-6/Timetal 21S composite yielding measurements of the matrix thermal residual stress as a function of several testing variables such as temperature, heating/cooling rate, thermal cycle upper limit and number of thermal cycles. Important features of the matrix axial thermal residual stress can be summarized as follows:

1. The level of the axial thermal residual stress in both the SCS-6/Timetal 21S and SCS-6/Ti-15-3 composites is always lower than the yield stress of the corresponding matrix material.
2. The level of the thermal residual stress at room temperature is proportional to the cooling rate.
3. At any temperature level, the axial thermal residual stress decreases as the number of thermal cycles increases. The magnitude of this decrease is proportional to the upper limit of the thermal cycle and inversely proportional to the cooling rate.
4. The relaxation of the thermal residual stress during a thermal cycle is governed by the amount of nonrecoverable viscous flow developed in the matrix during this cycle.
5. An important feature of the proposed technique is its ability to be extended to the study of thermomechanical responses of MMCs. In this case the experimental procedure would be executed with the inclusion of an externally applied load into the feedback governing equation. This technique is currently being utilized by the authors to study cases where the external load is constant (creep case) or time dependent (thermal mechanical fatigue cases).

2.7 REFERENCES

- [1] A. Saigal, D. S. Kupperman and S. Majumdar, Residual Strain in Titanium Matrix High-Temperature Composites. *Materials Science and Engineering*, Vol. 150A, 1992, pp.59-66
- [2] P. K. Brindley, S. L. Draper, J. I. Eldridge, M. V. Nathal and S. M. Arnold, The Effect of Temperature on the Deformation and Fracture of SiC/Ti-24Al-11Nb. *Metallurgical Transactions*, Vol. 23A, 1992, pp. 2527-2540
- [3] R. A. MacKay, *Scripta Metall. et Mater.* 24, 1990, pp.167-172
- [4] M. Sohi, J. Adams and R. Mahapatra, Transverse Constitutive Response of Titanium-Aluminum, Metal-Matrix Composites. In *Constitutive Law for Engineering Materials*, Eds. by C. D. Desai et al, ASME Press, New York, 1991, pp.617-626
- [5] W. S. Johnson, S. J. Lubowinski, A. L. Highsmith, W. D. Brewer and C. A. Hoogstraten, Mechanical Characterization of SCS₂/Ti-15-3 Metal Matrix Composites at Room Temperature, NASP TM-1014, 1988
- [6] W. S. Johnson, Mechanisms Controlling Fatigue Damage Development in Continuous Fiber Reinforced Metal Matrix Composites. In *Advances in Fracture Research*, eds. by K. Salama, K. Ravi-Chandar, D. M. R. Taplin and P. R. Rao, Vol. 2, Pergamon Press, New York, 1989, pp.897-905
- [7] C. -H. Hsueh, Interfacial Debonding and Fiber Pull-Out Stresses of Fiber-Reinforced Composites, III: With Residual Radial and Axial Stresses, *Materials Science and Engineering*, Vol. A145, 1991, pp.135-142
- [8] R. J. Kerans, Theoretical Analysis of the Fiber Pullout and Pushout Tests, *J. Am. Ceram. Soc.*, Vol. 74, 1991, pp.1585-1596
- [9] Davidson, D. L., The Micromechanics of Fatigue Crack Growth at 25°C in Ti-6Al-4V Reinforced with SCS-6 Fibers, *Metallurgical Transactions*, Vol. 23A, 1992, pp.865-879
- [10] D. B. Marshall and B. N. Cox, A J-Integral Method for Calculating Steady-State Matrix Cracking Stresses in Composites, *Mechanics of Materials*, Vol. 7, 1988, pp.127-133
- [11] L. S. Sigl and A. G. Evans, Effects of Residual Stress and Frictional Sliding on Cracking and Pull-out in Brittle Matrix Composites, *Mechanics of Materials*, Vol. 8, 1989, pp.1-12
- [12] D. B. Marshall and A. G. Evans, Failure Mechanisms in Ceramic-Fiber/Ceramic-Matrix Composite, *Journal of the American Ceramic Society*, Vol. 68, 1985, pp.225-231

- [13] S. M. Arnold and T. E. Wilt, Influence of Engineered Interfaces on Residual Stresses and Mechanical Response in Metal Matrix Composites, NASA TM-105438, March, 1992
- [14] Y. Mikata and M. Taya, Stress Field in a Coated Continuous Fiber Composite Subjected to Thermo-Mechanical Loadings, Journal of Composite Materials, Vol. 19, 1985, pp.554-578
- [15] B. N. Cox, M. R. James, D. B. Marshall and R. C. Addison, Jr., Determination of Residual Stresses in Thin Sheet Titanium Aluminide Composites, Metallurgical Transactions, Vol. 21A, 1990b, pp.2701-2707
- [16] S. S. Hecker, C. H. Hamilton and L. J. Ebert, Elastoplastic Analysis of Residual Stresses and Axial Loading in Composite Cylinders, Journal of Materials, Vol. 5, No. 4, 1970, pp.868-900
- [17] E. E. Gdoutos, D. Karalekas and I. M. Daniel, Thermal Stress Analysis of a Silicon Carbide/Aluminum Composite, Experimental Mechanics, Vol. 31, 1991, pp.202-208
- [18] A. D. Krawitz, D. G. Reichel and R. L. Hitterman, Residual Stress and Stress Distribution in a WC-Ni Composite, Materials Science and Engineering, Vol. A119, 1989, pp.127-134
- [19] M. Uemura, H. Iyama and Y. Yamaguchi, Thermal Residual Stresses in Filament-Wound Carbon-Fiber-Reinforced Composite, Journal of Thermal Stresses, Vol. 2, 1979, pp.393-412
- [20] S. Majumdar, J. P. Singh, D. Kupperman and A. D. Krawits, Application of Neutron Diffraction to Measure Residual Strains in Various Engineering Composite Materials, Journal of Engineering Materials and technology, Vol. 113, 1991, pp.51-59
- [21] K. Jayaraman and K. L. Reifsnider, Residual Stresses in a Composite with Continuously Varying Young's Modulus in the Fiber/Matrix Interphase, Journal of Composite Materials, Vol. 26, 1992, pp.770-791
- [22] D. A. Koss and S. M. Copley, Thermally Induced Residual Stresses in Eutectic Composites, Metallurgical transactions, Vol. 2, 1971, pp.1557-1560
- [23] H. M. Ledbetter and M. W. Austin, Thermal Stress in a Silicon-Carbide/Aluminum Composite, in Residual Stresses in Science and Technology, eds. by E. Macherauch and V. Hauk, Vol. 1, Deutsche Gesellschaft für Metallkunde Informationsgesellschaft, Verla, Germany, 1987, pp. 517-521
- [24] Y. Ikeuchi, Measurements of Thermal Stress Behavior on Tungsten Fiber-Copper Composites, in Residual Stresses in Science and Technology, eds. by E. Macherauch and V. Hauk, Vol. 1, Deutsche Gesellschaft für Metallkunde Informationsgesellschaft, Verla, Germany, 1987, pp. 523-530

- [25] W. Grellner and K. A. Schwetz, Investigations of Residual Stresses in Ceramic Components, in Residual Stresses in Science and Technology, eds. by E. Macherauch and V. Hauk, Vol. 1, Deutsche Gesellschaft für Metallkunde Informationsgesellschaft, Verla, Germany, 1987, pp. 531-537
- [26] S. Majumdar, D. Kupperman and J. Singh, Determinations of residual Thermal Stresses in a SiC-Al₂O₃ Composite Using Neutron Diffraction, 1988, Journal of the American Ceramic Society, Vol. 71, pp.858-863
- [27] A. J. Allen, M. Bourke, M. T. Hutchings, A. D. Krawitz and C. G. Windsor, Neutron Diffraction Measurement of Internal Stress in Bulk Materials: Metal-Matrix Composites, in Residual Stresses in Science and Technology, eds. by E. Macherauch and V. Hauk, Vol. 1, Deutsche Gesellschaft für Metallkunde Informationsgesellschaft, Verla, Germany, 1987, pp.151-157
- [28] V. Hauk, Measuring Techniques of Residual Stresses — Present Situation and Future Aimes, in Residual Stresses in Science and Technology, eds. by E. Macherauch and V. Hauk, Vol. 1, Deutsche Gesellschaft für Metallkunde Informationsgesellschaft, Verla, Germany, 1987, pp.231-242
- [29] N. E. Dowling, R. W. Hendricks and K. Ranganthan, X-Ray Residual Stress Measurements in Notched Test Specimens, Journal of Testing and Evaluation, Vol. 16, 1988, pp.456-460
- [30] A. Saigal, private communication, 1992
- [31] M. R. James and J. B. Cohen, The Measurement of Residual Stresses by X-Ray Diffraction Techniques, Treatise on Materials Science and Technology, ed. by H. Herman, Vol. 19, 1-62
- [32] B. N. Cox, M. S. Dadkhah, M. R. James, D. B. Marshall, W. L. Morris and M. Shaw, On Determining Temperature Dependent Interfacial Shear Properties and Bulk Residual Stresses in Fibrous Composites, Acta Metall. Mater. Vol 38, No 12, 1990a, pp. 2425-2433
- [33] S. Mall and P. G. Ermer, Thermal Fatigue behavior of a Unidirectional SCS6/Ti-15-3 Metal Matrix Composite. Journal of Composite Materials, Vol. 25, 1991, pp. 1668-1686
- [34] H. W. Rosenberg, Ti-15-3 Property Data, in Beta Titanium Alloys in the 80's, eds. by R. R. Boyer and H. W. Rosenberg, The Metallurgical Society of AIME, Warrendal, PA, 1984, pp.409-432
- [35] H. Ghonem, Y. Wen, D. Zheng, M. Thompson and G. Linsey, Effects of Temperature and Frequency on Fatigue Crack Growth in Timetal 21S Monolithic Laminate, to be published in Materials Science and Engineering, 1992
- [36] H. Ghonem and D. Zheng, The Depth of Intergranular Oxygen Diffusion during

Environment-Dependent Fatigue Crack Growth in Alloy 718, Materials Science and Engineering, Vol. 150A, 1992, pp.151-160

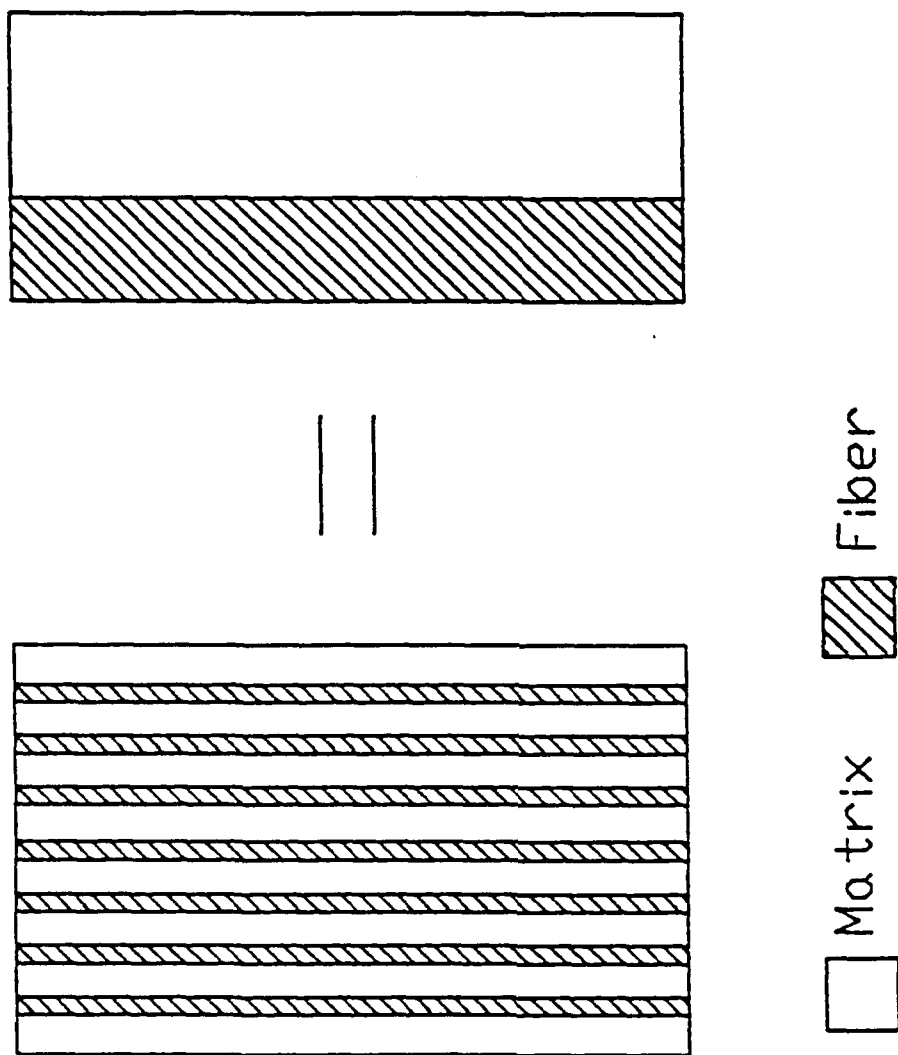


Fig. 2-1 Schematic of simplifying the composite major constituents, fiber and matrix, into two bar composite model.

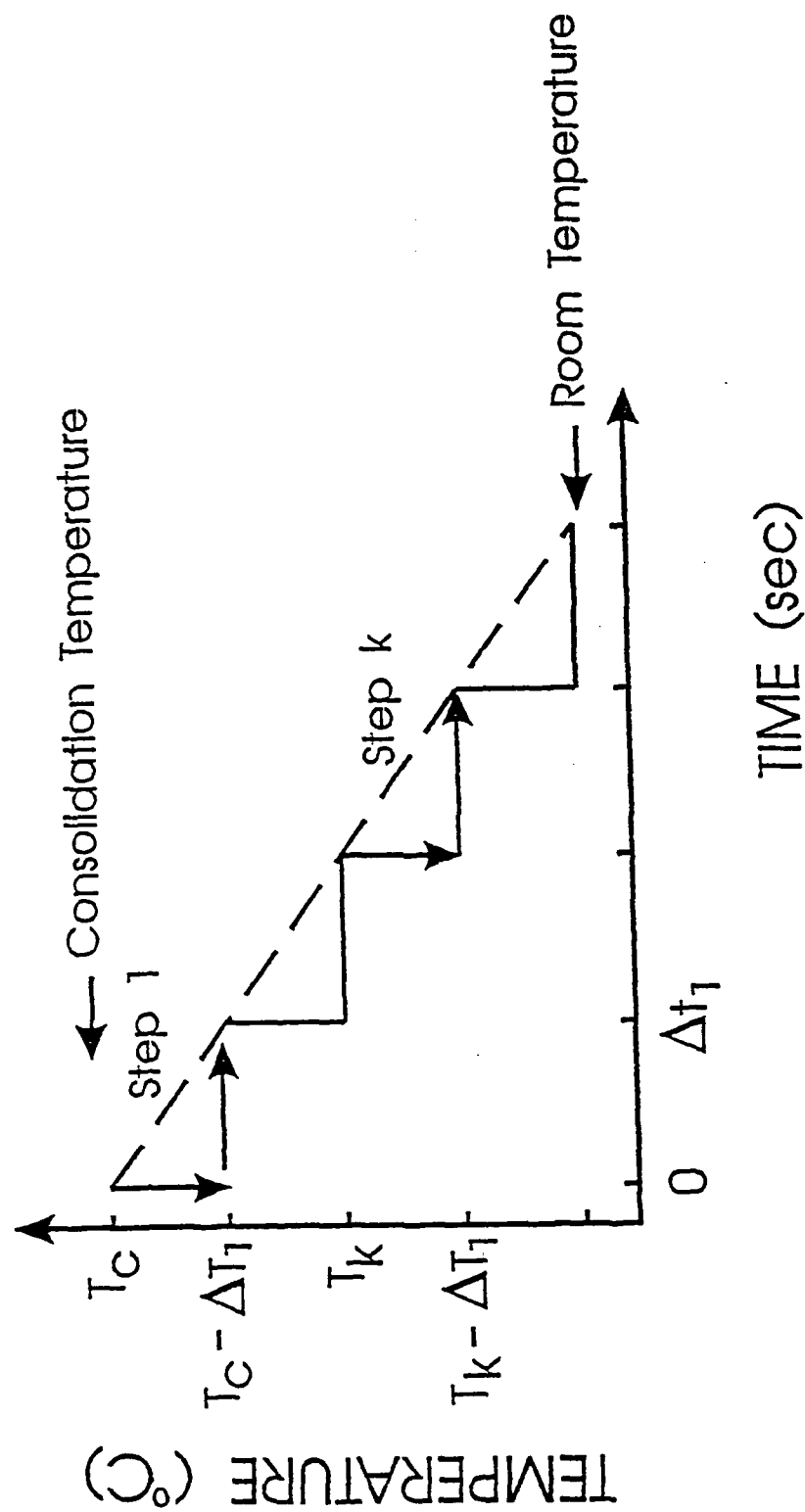


Fig. 2-2 Discretization of the cooling path from consolidation temperature to room temperature (no externally applied mechanical load).

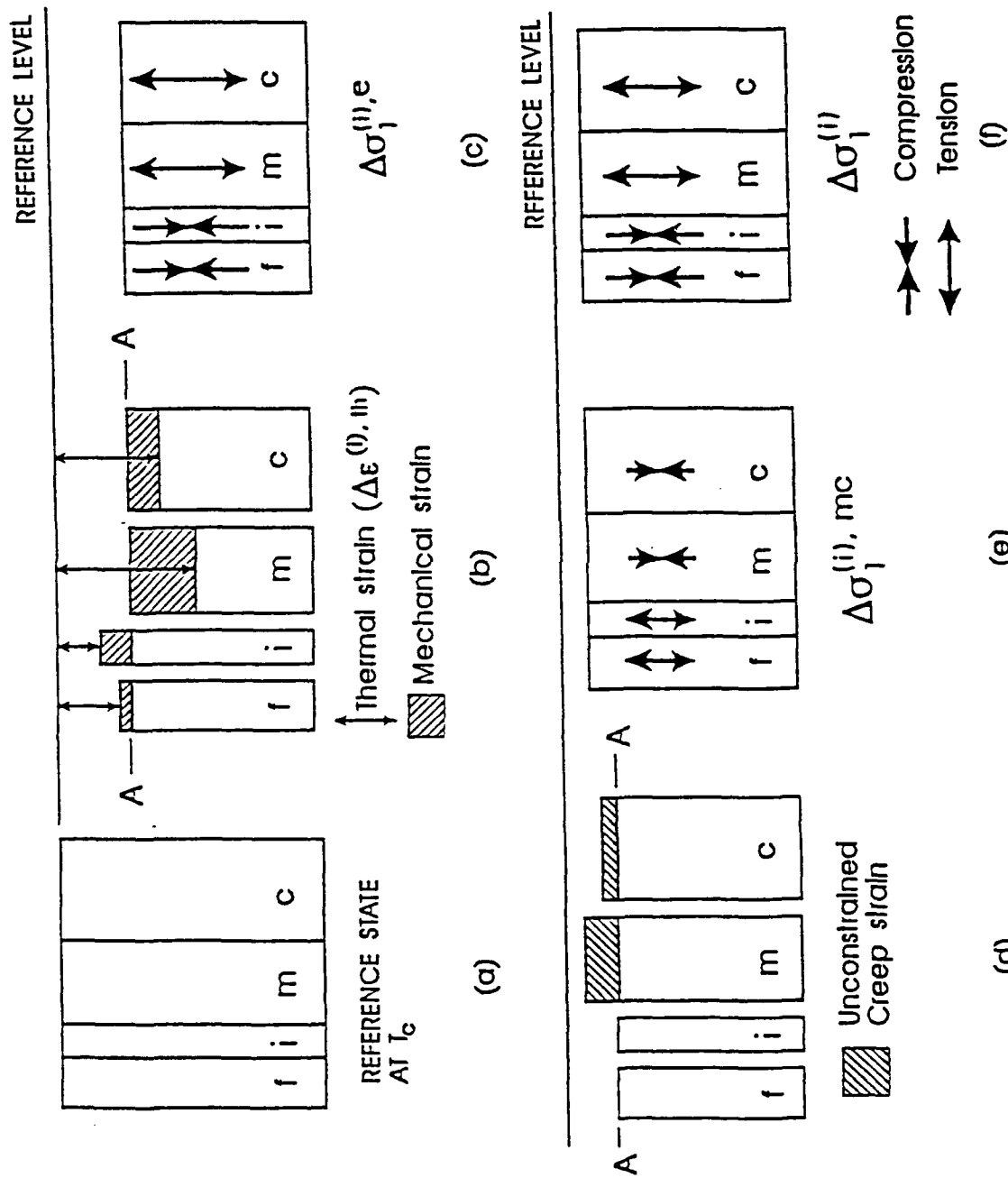


Fig. 2-3 Two bar model showing fiber and matrix responses during the first cool down step.

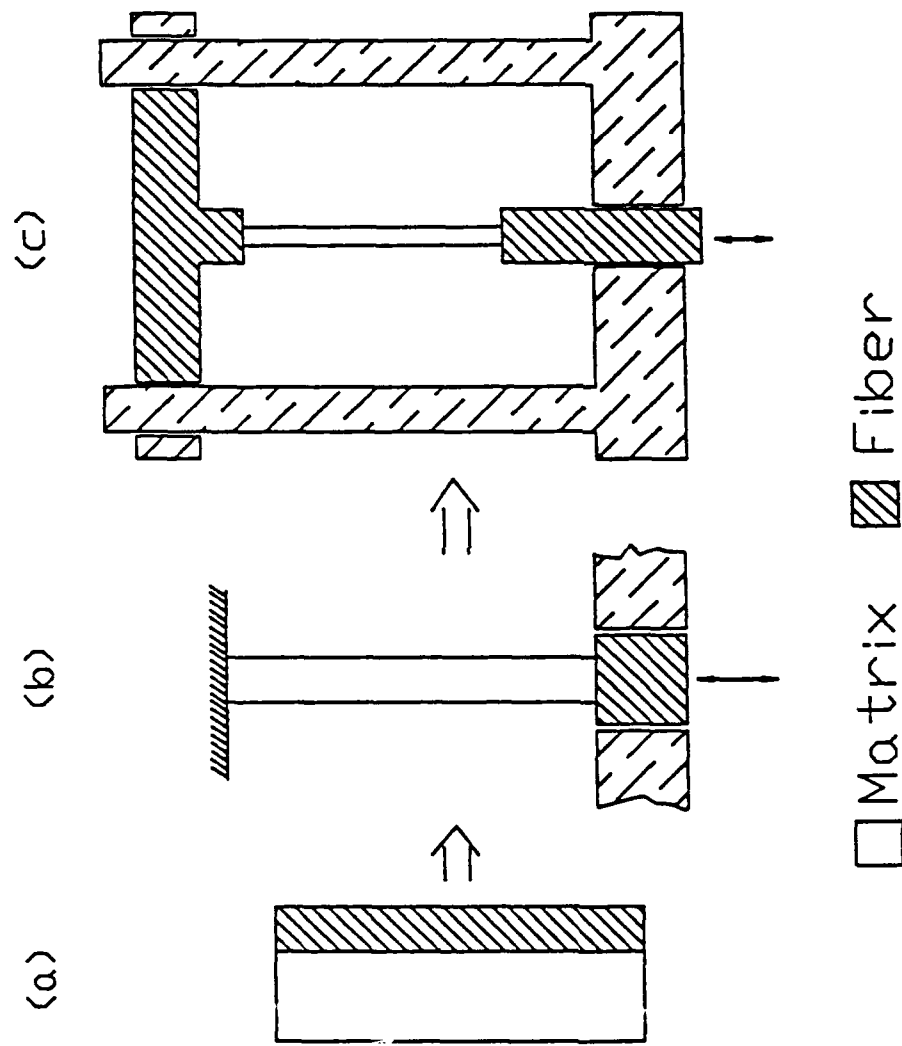


Fig. 2-4 Schematic of the idealization of fiber and matrix components in relation to a neat laminate (matrix material) loaded in a testing frame: (a) two bar composite model; (b) equivalent composite specimen where the matrix is restricted by a higher stiffness boundary; (c) equivalent composite system where a fiberless laminate specimen acts as a matrix while the restriction between matrix and fibers is imposed through adjustable loading system.

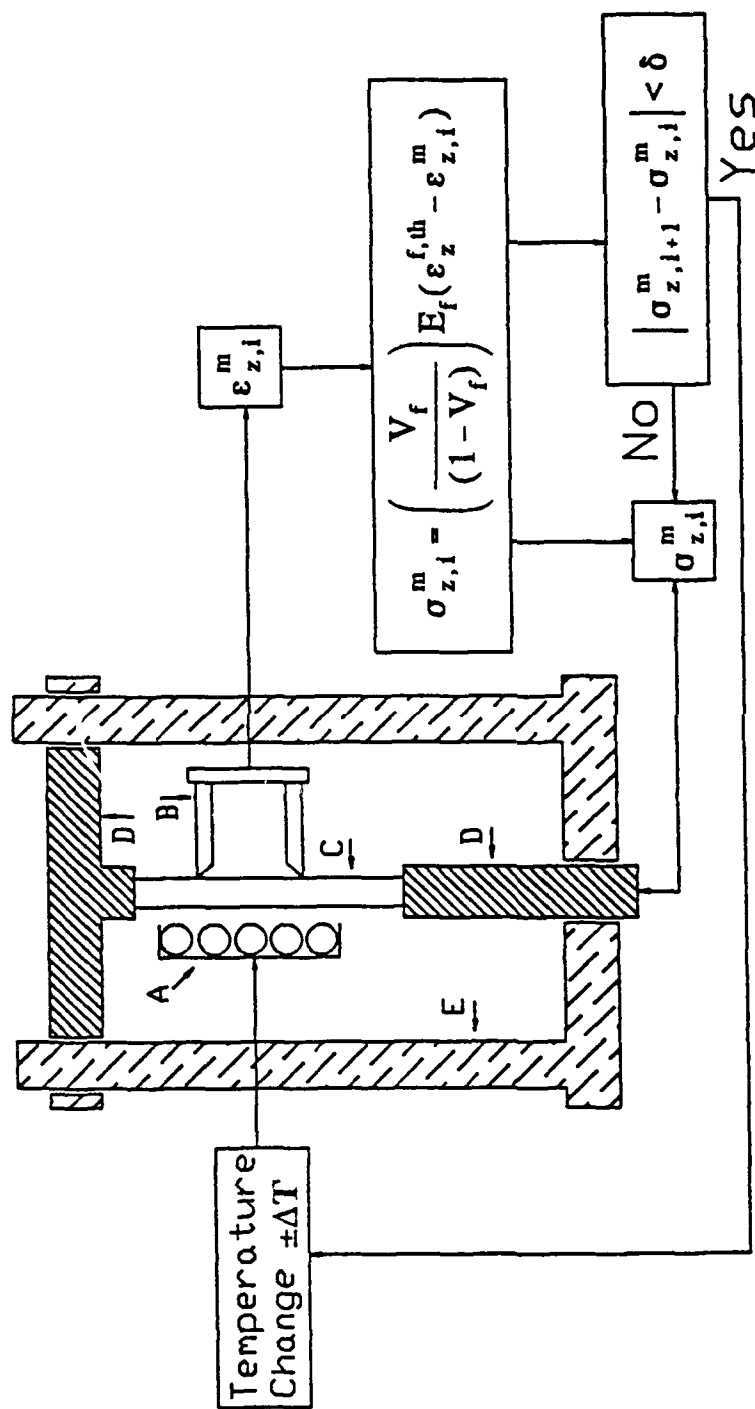


Fig. 2-5

Schematic of the simulation logic applied in the present study to estimate residual stress in the matrix component of a unidirectional reinforced metal matrix composite. A: heating unit; B: extensometer; C: fiberless laminate specimen; D: loading system; E: testing frame.

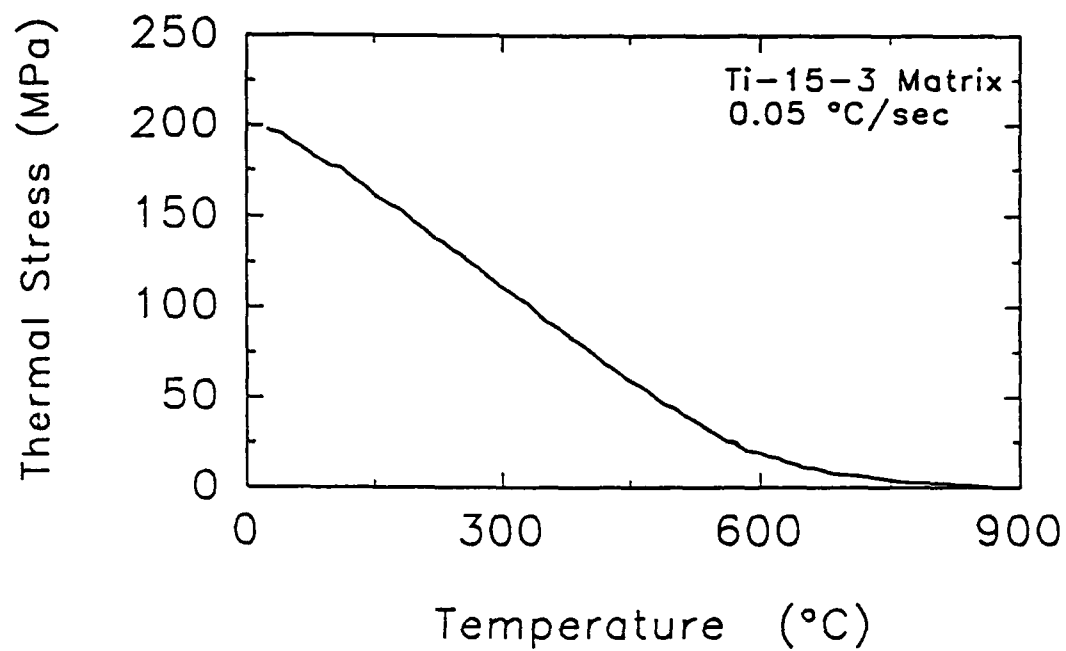


Fig. 2-6 Evolution of the thermal residual stress in Ti-15-3 matrix during cool-down from consolidation temperature using a cooling rate of 0.5°C/sec.

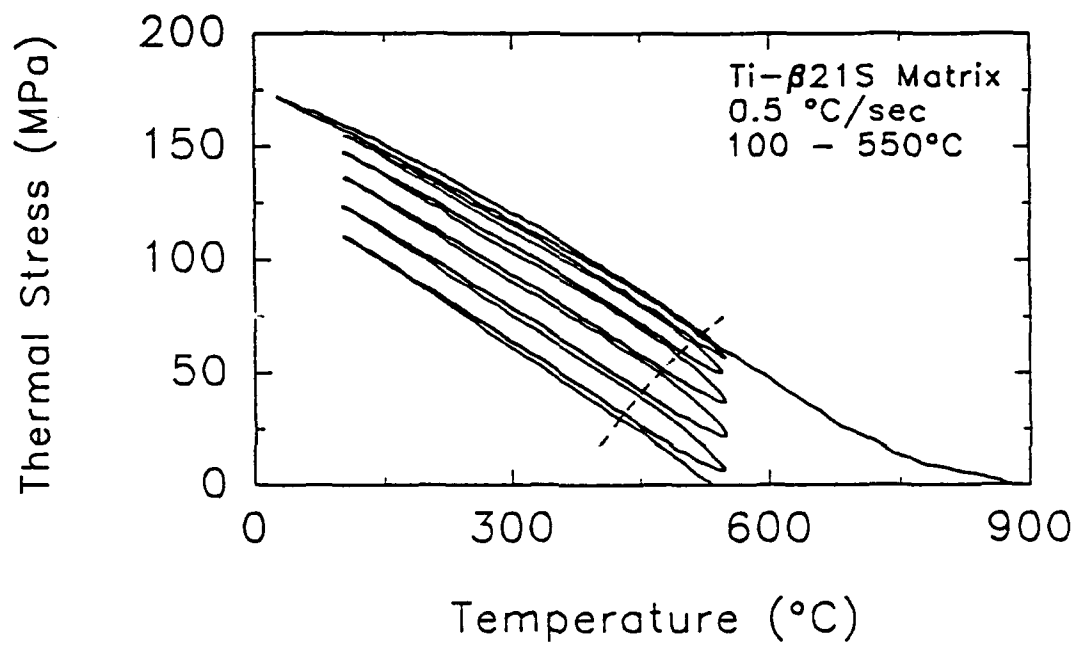


Fig. 2-7 Evolution of the thermal residual stress in Timetal®21S matrix during cool-down from consolidation temperature and subsequent thermal cycling between 100°C and 550°C using a cooling rate of 0.5°C/sec.

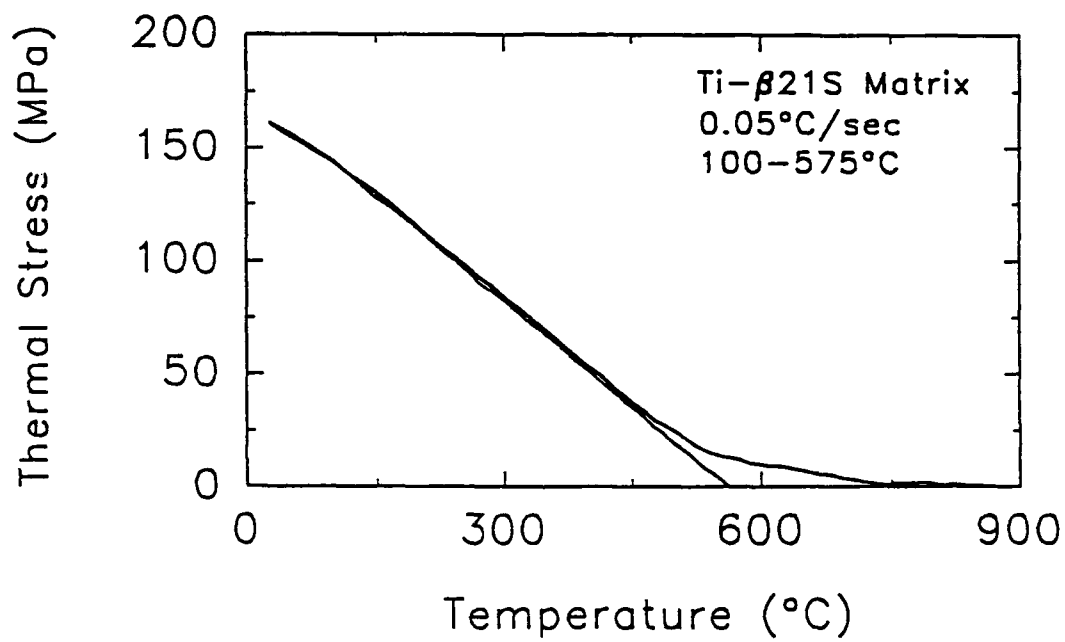


Fig. 2-8 Evolution of the thermal residual stress in Timetal®21S matrix during cool-down from consolidation temperature and reheating to 575°C using a cooling rate of 0.05°C/sec.

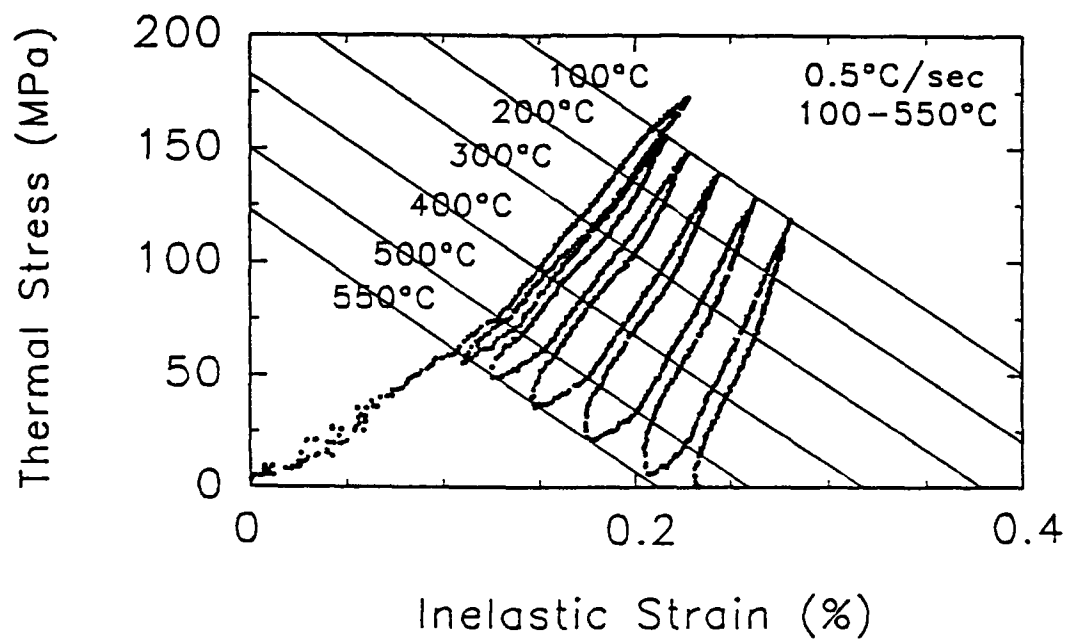


Fig. 2-9 Relationship between thermal residual stress in the matrix of SCS-6/Timetal®21S composite and corresponding inelastic strain as function of testing temperature.

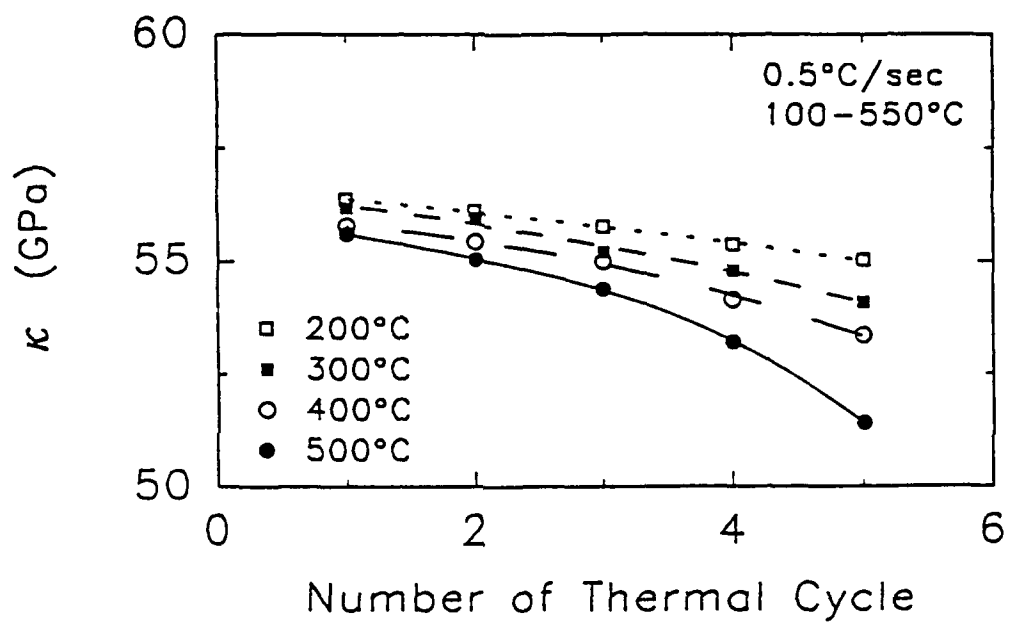


Fig. 2-10 Relationship between the strain hardening parameter of the matrix material of SCS-6/Timetal®21S and the number of thermal cycles.

SECTION 3

MICROMECHANICAL MODELLING OF TIME-DEPENDENT BEHAVIOR OF CONTINUOUS-FIBER-REINFORCED METAL MATRIX COMPOSITES³

ABSTRACT

A new time-dependent model has been developed in order to predict the response of metal matrix composites subjected to thermal loadings. In this model, elastic, plastic and creep behavior have been considered. The model consists of a fiber and an interphase zone which behave elastically while the matrix and the surrounding composite media exhibit creep deformation. The cooling/heating path is discretized into load steps where elastic-plastic behavior is assumed to occur spontaneously over a temperature increment while creep behavior occurred over the following time increment. The plastic characteristics follows the deformation theory of plasticity. In the transient and steady-state stages of creep, the constraint-free creep deformation of the matrix and the composite media are calculated using the Bailey-Norton law with an Arrhenius-type expression for time-dependent creep coefficient. The "stiffness" method with a modified load vector is employed in calculating the constrained deformation in the composite. The accumulated creep strain history is predicted using the "strain hardening" formulation. The model can be easily extended to include external loading and employed to study the evolution of the stress and strain states in the constituents of the composite during isothermal and thermo-mechanical loadings.

3.1 INTRODUCTION

In Titanium-based metal matrix composites, the metallic matrix properties of ductility and toughness are combined with reinforcement properties of high strength and high modulus to yield increased strength-to-weight ratio and higher stiffness materials. These metal matrix composites (MMCs) are being developed as high performance materials capable of withstanding high temperatures and operating loads typical for advanced aerospace applications.

Continuous-fiber-reinforced MMCs are consolidated at high temperature which induce high thermal residual stresses during post-fabrication cool down. This is a consequence of mismatches of the coefficients of thermal expansions (CTEs) of the matrix and the fibers. These thermal residual stresses may initiate fiber/matrix debonding and radial cracking in the matrix and hence, dictate the subsequent behavior of the composites when subjected to thermo-mechanical loading. It was found that post-fabrication procedures such as thermal cycling can alter the residual stress states in titanium composites [1]. Consequently, determination of thermal residual stress and strain fields in a continuous-fiber-reinforced MMC is an essential step in characterizing the performance of the composite system.

Various analytical models have been developed and applied to study the thermal stress behavior

³ based on "Time-dependent behavior of continuous-fiber-reinforced metal matrix composites, part I: micromechanical modeling", M. Tamin, D. Zheng and H. Ghonem, submitted to Composite Material & Technology, 1993.

of continuous-fiber-reinforced composites. Besides the plane-stress lamina model (e.g. [2,3]), the concentric cylinder model has been well studied (e.g. [4-7]). Uemura [5] developed a two-phase model which consists of inner and outer cylinder to simulate the fiber and the matrix phase, respectively. In this model, the fiber-matrix interface has been treated as a perfect mathematical surface. Experimental work, however, indicated that the interphase formation accompanying the development of reaction zones in metal matrix composites is inevitable (e.g. [8,9]). Incorporation of interphase behavior into the micromechanical analyses of composite systems is therefore critical in realistic modelling of the mechanical behavior of the composites [7,10]. Based on this consideration, several researchers have proposed the three-phase model (fiber/interphase/matrix) to account for interphase effects (e.g. [7,10-12]). In reality, the "matrix cylinder" is surrounded by the composite media instead of a free surface, thus it is reasonable to impose a layer of homogeneous material with the composite properties surrounding the matrix layer in order to retain realistic boundary conditions (e.g. [13,14]). Following these ideas, Mikata [6] proposed a four-phase model (fiber/interphase(coating)/matrix/surrounding composite media) for elastic analysis of stress field in the composites.

As mentioned above, Titanium-based metal matrix composites are primarily developed for high temperature applications. At such extreme thermal and mechanical service conditions, the composite will experience time dependent deformation. Accurate representation of this nonlinear material behavior is essential in realistic determination of the stress and strain response of the composite. Experimental creep study on SCS-6/Ti-6Al-4V composite indicated that titanium-based composite exhibits creep behavior similar to that of the monolithic matrix (even though the longitudinal creep has been suppressed considerably by fiber reinforcement). This fact implies that creep behavior of the matrix alloy and the corresponding composite must be incorporated into the model formulation. However, fewer work has been done to model the creep behavior of fiber-reinforced metal matrix composites. Min [15] developed a plane-stress continuum model to analyze the primary creep deformation of a unidirectional metal matrix composite. Gayda [16] employed a cylindrical two-phase model to study the time-dependent behavior of TMCs in which the creep behavior of the matrix was considered by a relaxation curve obtained from an empirical fit of stress relaxation data for the matrix alloy. Since the composite media and the reaction zone were not included in these models, the models could not consider influences of the existence of these two phases on the overall creep behavior of the composite.

The objective of this section is to develop a micromechanical approach to analyze the elastic-plastic and creep behavior of a unidirectional continuous-fiber-reinforced metal matrix composite. This approach emphasizes the time-dependent stress analysis which is critical to high temperature applications. The four-phase cylinder model adopted in the present approach makes it possible to trace the evolution of the stress states for each constituent in the composite during cyclic thermal loadings. The concept of the model including mathematical formulations of the elastic, plastic and creep analyses are presented in the next section of the paper. This is followed by narration of a typical elastic-plastic-creep calculation routine. The last part of the paper includes conclusions and summary.

3.2 CONCEPTS OF THE MICROMECHANICAL APPROACH

The four-phase configuration adopted in this approach is illustrated in Fig. 3-1(a) where the fibers in the composite are assumed to be arranged in a hexagonal array. A hexagonal unit is substituted for the concentric fiber, reaction zone and matrix cylinders with radii r_4 , r_3 , and r_2 ,

respectively, while the equivalent composite media is represented by the outermost cylinder with radius r_1 , as shown in Fig. 3-1(b). The fiber and the reaction zone are assumed to behave elastically at all loading conditions while the matrix and the surrounding equivalent composite media may undergo any combination of elastic, plastic and creep deformation depending on the nature of the applied load. All the constituent phases are assumed to be isotropic. In addition, the model is subjected to axisymmetric thermal loading with a uniform temperature distribution across all layers.

During post-fabrication cool down and subsequent thermal cycling, the cooling/heating path is piecewise discretized into load steps, each of which consists of a temperature increment, ΔT , followed by a time increment, Δt , as shown in Fig. 3-2. For a particular load step, the elastic-plastic and creep response is a summation of the elastic-plastic response due to ΔT and the creep response over the range of Δt .

In order to illustrate the fundamental concepts of the approach proposed here, a one-dimensional four-bar model is utilized as schematically detailed in Fig. 3-3. The assumed stress-free state of the composite at consolidation temperature, T_c , is shown in Fig. 3-3(a) while Fig. 3-3(b) represents the relative amount of thermal strain increments (shrinkage), $\Delta \epsilon_1^{(i)th}$, in each layer if subjected to a uniform finite temperature drop, $-\Delta T_1$ corresponding to the first load step. Superscript $i = 1, 2, 3, 4$ denotes the outermost composite media, the matrix, the reaction zone and the fiber, respectively. Assuming that all layers are perfectly bonded at interfaces, the deformation compatibility requires that an isostrain condition exists in all layers giving rise to elastic stress increments, $\Delta \sigma_1^{(i)e}$ as illustrated in Fig. 3-3(c). These uniaxial stresses are compressive in the fiber and reaction zone thus making the layers as if compressed from their initial strain-free position to the common level A-A. However, the matrix layer and the composite media are elongated from their initial strain-free position to the same level A-A resulting in tensile stresses. The magnitude of the stresses depend on the values of CTE and elastic modulus of each layer. The difference between the strain level due to free thermal contraction for each layer and the strain at the constrained level A-A is termed the mechanical strain. The mechanical strain increments corresponding to each of the model layers, $\Delta \epsilon_1^{(i)me}$ are represented as shaded areas in Fig. 3-3(b) with positive values lying below and negative values above the level A-A.

If the effective stress in the matrix exceeded the yield limit of the matrix material at a particular temperature level, plastic deformation in the matrix is calculated using the deformation theory of plasticity [17]. Stresses in all layers are redistributed such that equilibrium and compatibility conditions are satisfied. The new stress and strain increments in all layers due to matrix plasticity are denoted as $\Delta \sigma_1^{(i)mp}$ and $\Delta \epsilon_1^{(i)mp}$, respectively.

The important feature of the present model is the incorporation of the creep behavior of the matrix and the surrounding equivalent composite media into the stress analysis. This concept can also be explained by the four-bar representation shown in Fig. 3-3. The stresses induced in the matrix and the composite media due to temperature change, ΔT_1 will produce a relative constraint-free creep strain increment, $\Delta \epsilon_1^{(i)cr}$ in the respective layer over the proceeding time duration, Δt_1 (see Fig. 3-3(d)). The existence of non-creeping phases (the reaction zone and the fiber) and perfect bonding at layer interfaces will restrain the creep deformation in both the matrix and the equivalent composite media, resulting in stress redistribution in all layers. These creep-related stress increments are denoted as $\sigma_1^{(i)mc}$ (see Fig. 3-3(e)). The net stress developed for the first load step is taken as the summation of the stress increments, $\Delta \sigma_1^{(i)e}$ or $\Delta \sigma_1^{(i)mp}$, generated by restriction imposed on free thermal contraction of each layer, and the stress increments, $\Delta \sigma_1^{(i)mc}$, induced by constrained creep deformation of the matrix and the equivalent composite media. Since the creep stress increments in the matrix and equivalent composite media are compressive, the net stress increments in these layers

are always less than that calculated for the elastic-plastic case.

The concepts discussed above are identical for subsequent load steps. For the k^{th} load step, elastic calculation is first performed to obtain the elastic stress increments, $\Delta\sigma_k^{(i),e}$, corresponding to the current temperature change, ΔT_k . The elastic stress increments are then added to the total stress level in the matrix up to the last load step and the value is compared with the yield limit at the current temperature. If the yield criterion is satisfied, the plasticity analysis is executed and the stresses in all phases are redistributed resulting in the stress increments, $\Delta\sigma_k^{(i),mp}$. The total stresses acting in the matrix and the equivalent composite media may cause constraint-free creep deformation during the time duration, Δt_k . However, restriction imposed on the creep deformation by the elastic reaction zone and fiber, and perfect bonding at layer interfaces result in stress increments, $\Delta\sigma_k^{(i),mc}$ in all layers. At the end of the k^{th} load step, the total stress is the sum of the accumulated stresses from all previous load steps, stress increment due to temperature change and stress increment due to creep flow restriction imposed in the current load step, i.e.

$$\sigma_k^{(i)} = \sigma_{k-1}^{(i)} + \Delta\sigma_k^{(i),mp} + \Delta\sigma_k^{(i),mc} \quad (1)$$

The simultaneous evolution of the corresponding radial and hoop stress components in the complex stress state of MMC are analogous to the axial component described above. However, the relative magnitudes of these transverse stresses are also influenced by the Poisson's ratio effects in all the phases.

3.3 FORMULATIONS

A cylindrical coordinate system with the radial, hoop, and axial coordinates denoted as r , θ , and z , respectively is shown in Fig. 3-1(a). Due to the axisymmetry of the model, the shear stress and shear strain components are zero. Neglecting body forces, the equilibrium equations for the i^{th} layer can be written as:

$$\frac{\partial \sigma_{rr}^{(i)}}{\partial r} + \frac{\sigma_{rr}^{(i)} - \sigma_{\theta\theta}^{(i)}}{r} = 0, \quad \frac{\partial \sigma_{zz}^{(i)}}{\partial z} = 0 \quad (2)$$

It is assumed that the total strain in i^{th} layer can be decomposed into elastic, $\epsilon^{(i),e}$, thermal, $\epsilon^{(i),th}$, plastic, $\epsilon^{(i),p}$, and creep, $\epsilon^{(i),cr}$, components such that

$$\begin{aligned} \epsilon_{rr}^{(i)} &= \epsilon_{rr}^{(i),e} + \epsilon_{rr}^{(i),th} + \epsilon_{rr}^{(i),p} + \epsilon_{rr}^{(i),cr} \\ \epsilon_{\theta\theta}^{(i)} &= \epsilon_{\theta\theta}^{(i),e} + \epsilon_{\theta\theta}^{(i),th} + \epsilon_{\theta\theta}^{(i),p} + \epsilon_{\theta\theta}^{(i),cr} \\ \epsilon_{zz}^{(i)} &= \epsilon_{zz}^{(i),e} + \epsilon_{zz}^{(i),th} + \epsilon_{zz}^{(i),p} + \epsilon_{zz}^{(i),cr} \end{aligned} \quad (3)$$

The constitutive relations for isotropic material behavior in generalized plane strain conditions can be written as:

$$\begin{aligned} \sigma_{rr}^{(i)} &= K^{(i)} \left[(1 - \nu^{(i)}) (\epsilon_{rr}^{(i)} - \epsilon_{rr}^{(i),p} - \epsilon_{rr}^{(i),cr}) + \nu^{(i)} (\epsilon_{\theta\theta}^{(i)} - \epsilon_{\theta\theta}^{(i),p} - \epsilon_{\theta\theta}^{(i),cr}) \right. \\ &\quad \left. + \nu^{(i)} (\epsilon_{zz}^{(i)} - \epsilon_{zz}^{(i),p} - \epsilon_{zz}^{(i),cr}) - (1 + \nu^{(i)}) \epsilon^{(i),th} \right] \end{aligned}$$

$$\sigma_{\theta\theta}^{(i)} = K^{(i)} \left[(1 - \nu^{(i)}) (\epsilon_{\theta\theta}^{(i)} - \epsilon_{\theta\theta}^{(i),p} - \epsilon_{\theta\theta}^{(i),cr}) + \nu^{(i)} (\epsilon_{zz}^{(i)} - \epsilon_{zz}^{(i),p} - \epsilon_{zz}^{(i),cr}) \right. \\ \left. + \nu^{(i)} (\epsilon_{rr}^{(i)} - \epsilon_{rr}^{(i),p} - \epsilon_{rr}^{(i),cr}) - (1 + \nu^{(i)}) \epsilon^{(i),th} \right] \quad (4)$$

$$\sigma_{zz}^{(i)} = K^{(i)} \left[(1 - \nu^{(i)}) (\epsilon_{zz}^{(i)} - \epsilon_{zz}^{(i),p} - \epsilon_{zz}^{(i),cr}) + \nu^{(i)} (\epsilon_{rr}^{(i)} - \epsilon_{rr}^{(i),p} - \epsilon_{rr}^{(i),cr}) \right. \\ \left. + \nu^{(i)} (\epsilon_{\theta\theta}^{(i)} - \epsilon_{\theta\theta}^{(i),p} - \epsilon_{\theta\theta}^{(i),cr}) - (1 + \nu^{(i)}) \epsilon^{(i),th} \right]$$

where the constant $K^{(i)}$ is defined as:

$$K^{(i)} = \frac{E^{(i)}}{(1 + \nu^{(i)})(1 - 2\nu^{(i)})} \quad (5)$$

and $E^{(i)}$ is the elastic modulus, $\nu^{(i)}$ is the Poisson's ratio, $\epsilon_{rr}^{(i),p}$, $\epsilon_{\theta\theta}^{(i),p}$ and $\epsilon_{zz}^{(i),p}$ are the radial, hoop and axial components, respectively of the plastic strain, while $\epsilon_{rr}^{(i),cr}$, $\epsilon_{\theta\theta}^{(i),cr}$ and $\epsilon_{zz}^{(i),cr}$ are the radial, hoop and axial components, respectively of the creep strain of the constituent phases. The thermal strain, $\epsilon^{(i),th}$, is defined as:

$$\epsilon^{(i),th} = \int_{T_0}^T \alpha^{(i)} dT \quad (6)$$

where $\alpha^{(i)}$ is the CTE of i^{th} layer, T_0 is the reference temperature and T is the current temperature.

Due to the axial symmetry of the model configuration, the radial and axial displacements in each layer can be expressed as functions of r and z , respectively while the hoop displacement component is zero, i.e.

$$u_r^{(i)} = u^{(i)}(r) \quad , \quad u_\theta^{(i)} = 0 \quad , \quad u_z^{(i)} = w^{(i)}(z) \quad (7)$$

The non-zero strain-displacement relations could then be obtained using the displacement field which, when used in the constitutive relations, eqs. (4), would result in the governing equations for elastic-plastic-creep behavior of MMC as follows:

$$r^2 \frac{d^2 u^{(i)}}{dr^2} + r \frac{du^{(i)}}{dr} - u^{(i)} = \Phi^{(i)}(r) \quad , \quad \frac{d^2 w^{(i)}}{dz^2} = 0 \quad (8)$$

where $\Phi^{(i)}(r)$ is defined as:

$$\Phi^{(i)}(r) = r \left(\frac{1 - 2\nu^{(i)}}{1 - \nu^{(i)}} (\epsilon^{(i),p_{rr}} + \epsilon^{(i),cr_{rr}}) + r \frac{d}{dr} (\epsilon^{(i),p_{rr}} + \epsilon^{(i),cr_{rr}}) - \frac{1 - 2\nu^{(i)}}{1 - \nu^{(i)}} (\epsilon^{(i),p_{\theta\theta}} + \epsilon^{(i),cr_{\theta\theta}}) \right. \\ \left. + r \frac{\nu^{(i)}}{1 - \nu^{(i)}} \frac{d}{dr} (\epsilon^{(i),p_{\theta\theta}} + \epsilon^{(i),cr_{\theta\theta}}) + r \frac{\nu^{(i)}}{1 - \nu^{(i)}} \frac{d}{dr} (\epsilon^{(i),p_{zz}} + \epsilon^{(i),cr_{zz}}) \right)$$

It is noted that $\Phi^{(i)}(r)$ consists of plastic strain terms pertaining to the matrix and creep strain terms pertaining to both the matrix and the outermost composite media. Consequently, for a purely elastic

loading, the function, $\Phi^{(i)}(r)$ is reduced to zero. The form of $\Phi^{(i)}(r)$ used in this analysis will be discussed in detail in the creep analysis part of this section.

The boundary conditions for the present study under the assumption that no external applied loading exist, are specified as follows:

(a) The continuity requires that both radial displacements and stresses at all layer interfaces be continuous.

(b) Since there is no external radial load at the outermost surface, therefore:

$$\text{at } r = r_1, \sigma_{rr}^{(1)} = 0 \quad (10)$$

(c) In the absence of external axial load, the axial forces in each layer due to thermal loading are equilibrated in the average sense, i.e.

$$\int_0^{r_1} \sigma_{zz}^{(4)} r dr + \int_{r_1}^{r_2} \sigma_{zz}^{(3)} r dr + \int_{r_2}^{r_3} \sigma_{zz}^{(2)} r dr + \int_{r_3}^{r_4} \sigma_{zz}^{(1)} r dr = 0 \quad (11)$$

In addition, under the assumption of perfect bonding at layer interfaces, the isostrain condition is applied to the total strains for all layers.

3.3.1 Elastic-Plastic Analysis

As discussed above, the cooling and heating paths are discretized into load steps each of which consists of a temperature increment, ΔT followed by a time increment, Δt . The analysis begins with a purely elastic formulation due to the temperature increment, so that the function $\Phi^{(i)}(r)$ diminishes and eq. (8) is reduced to

$$r^2 \frac{d^2 u^{(i)}}{dr^2} + r \frac{du^{(i)}}{dr} - u^{(i)} = 0, \quad \frac{d^2 w^{(i)}}{dz^2} = 0 \quad (12)$$

The above homogeneous equations have the following general solutions for the radial and axial displacement, respectively,

$$u^{(i)} = A_i r + \frac{B_i}{r}, \quad w^{(i)} = L_i z + P_i \quad (13)$$

where A_i , B_i , L_i and P_i are unknown constants.

Since the displacement is finite at the center of the fiber, where $r = 0$, i.e. $|u^{(4)}(0)| < \infty$, thus $B_4 = 0$. It is also noted that P_i in the above equations account for rigid body motion in axial direction, thus P_i can be set to zero without loss of generality. In addition, application of the boundary conditions for axial displacement components results in

$$L_1 = L_2 = L_3 = L_4 = L \quad (14)$$

The elastic strain field can now be expressed as:

$$\epsilon_{rr}^{(i),e} = A_i - \frac{B_i}{r^2}, \quad \epsilon_{\theta\theta}^{(i),e} = A_i + \frac{B_i}{r^2}, \quad \epsilon_{zz}^{(i),e} = L \quad (15)$$

and the corresponding stress field for the elastic case are given as:

$$\begin{aligned}\sigma_{rr}^{(i),e} &= K^{(i)} \left[A_i - (1 - 2\nu^{(i)}) \frac{B_i}{r^2} + \nu^{(i)} L - (1 + \nu^{(i)}) \epsilon^{(i),th} \right] \\ \sigma_{\theta\theta}^{(i),e} &= K^{(i)} \left[A_i + (1 - 2\nu^{(i)}) \frac{B_i}{r^2} + \nu^{(i)} L - (1 + \nu^{(i)}) \epsilon^{(i),th} \right] \\ \sigma_{zz}^{(i),e} &= K^{(i)} \left[2\nu^{(i)} A_i + (1 - \nu^{(i)}) L - (1 + \nu^{(i)}) \epsilon^{(i),th} \right]\end{aligned}\quad (16)$$

The unknown constants in eqs. (13) ~ (16) are determined by the boundary conditions. Applying these conditions to eqs. (13) and (16) results in a set of eight simultaneous equations which should be solved for the determination of the constants $A_1 \sim A_4$, $B_1 \sim B_3$ and L . These equations can be arranged in the following matrix form:

$$Ac = b \quad (17)$$

where A is an 8×8 matrix termed the stiffness matrix consisting of model geometry and mechanical properties of all constituents of the composite, b is the thermal loading vector and c is the vector of unknown constants. Once the unknown vector c is solved from eq. (17), the elastic stress and strain states in the composite are then established.

The thermal stresses developed in the matrix during cool down may be high enough to initiate plastic yielding in the monolithic matrix material. Matrix plasticity is assumed to be a time-independent process and its effect can be treated separately from the time-dependent creep response of the matrix material. The governing equation for the elastic-plastic deformation of the composite is then given by eqs. (8) but without the creep strain terms in the loading function, $\Phi^{(i)}(r)$ given by eq. (9). One solution approach requires the knowledge of plastic strain distribution across the matrix layer. The assumption on this distribution will dictate the form and order of the displacement field in each layer due to the occurrence of matrix plasticity. This approach results in a similar stiffness equation, eq. (17) but with a new load vector, f , for thermal and matrix plasticity effects.

An alternate solution approach which modifies the stiffness matrix instead of the load vector of eq. (17), to account for strain hardening of the matrix material is employed in the present analysis. This approach utilizes the deformation theory of plasticity in conjunction with the von Mises yield criterion and the isotropic hardening rule. Matrix yielding commences when the effective stress, $\bar{\sigma}$ is equal to the temperature-dependent yield limit of the matrix material, $\sigma_{ys}(T)$. Here, $\bar{\sigma}$ is defined as:

$$\bar{\sigma} = \frac{1}{\sqrt{2}} \left[(\sigma_{rr} - \sigma_{\theta\theta})^2 + (\sigma_{\theta\theta} - \sigma_{zz})^2 + (\sigma_{zz} - \sigma_{rr})^2 \right]^{\frac{1}{2}} \quad (18)$$

The constitutive relations for total strain increment (elastic plus plastic) are employed based on the work of Hecker [4,17], and are given as:

$$\begin{aligned}
d\epsilon_{rr} &= \frac{1}{H(T)} [d\sigma_{rr} - \eta(d\sigma_{\theta\theta} + d\sigma_{zz})] \\
d\epsilon_{\theta\theta} &= \frac{1}{H(T)} [d\sigma_{\theta\theta} - \eta(d\sigma_{rr} + d\sigma_{zz})] \\
d\epsilon_{zz} &= \frac{1}{H(T)} [d\sigma_{zz} - \eta(d\sigma_{rr} + d\sigma_{\theta\theta})]
\end{aligned} \tag{19}$$

where $H(T)$ is the plastic modulus of the uniaxial tensile stress-strain curve of the matrix and η is the effective Poisson's ratio which is defined for a small increment of effective total strain, $d\bar{\epsilon}$, as:

$$\eta = 0.5 - (0.5 - \nu) \frac{H(T)}{E(T)} \tag{20}$$

The effective total strain increment is defined as:

$$d\bar{\epsilon} = \frac{\sqrt{2}}{2(1+\eta)} [(d\epsilon_{rr} - d\epsilon_{\theta\theta})^2 + (d\epsilon_{\theta\theta} - d\epsilon_{zz})^2 + (d\epsilon_{zz} - d\epsilon_{rr})^2]^{\frac{1}{2}} \tag{21}$$

It is assumed that the effective stress-strain curve of the matrix material in the region the yield limit can be represented by

$$\bar{\sigma} = k(T) \bar{\epsilon}^{\frac{1}{n(T)}} \tag{22}$$

where $k(T)$ and $n(T)$ are material parameters varying with temperature T . The slope of the curve represented by this equation is equal to the plastic modulus, $H(T)$, i.e.

$$\frac{d\bar{\sigma}}{d\bar{\epsilon}} = \frac{\bar{\sigma}}{n(T)\bar{\epsilon}} = H(T) \tag{23}$$

If plastic deformation occurs in the matrix, the stresses in all the four layers must be redistributed such that equilibrium and compatibility conditions are always satisfied. The stiffness matrix in eq. (19) is modified by substituting the plastic modulus, $H(T)$ and the effective Poisson's ratio, η for the elastic modulus, $E(T)$ and Poisson's ratio, ν , respectively. Consequently, the stiffness equation which accounts for matrix plasticity can be written as:

$$M\mathbf{c} = \mathbf{b} \tag{24}$$

It is noted that in elastic region $H(T)$ is equivalent to $E(T)$ and η reduces to ν , so that eq. (19) resembles the Hooke's law. Since the equilibrium equations, the compatibility equations and the boundary conditions are independent of the state of the material, therefore, the plasticity formulation is identical to the elastic case with the modified stiffness matrix, M in eq. (24). The resulting stress components, $\Delta\sigma_{ij}^{(i),mp}$ and strain components, $\Delta\epsilon_{ij}^{(i),mp}$ due to matrix yielding are given by eqs. (16) and (15), respectively.

3.3.2 Creep Analysis

The effect of creep deformation in both the monolithic matrix and the surrounding effective composite media on the residual stress and strain fields in the composite is now considered. It is assumed that the creep behavior of both layers in the primary and secondary stages of creep can be represented by the Bailey-Norton law as:

$$\epsilon^{cr} = B \sigma^m t^n \quad (25)$$

where ϵ^{cr} is the creep strain occurring in the material under uniaxial stress, σ , over a time duration t . The superscript i is omitted in the following derivation for convenience. Parameters B , m and n are material parameters. Based on the fit of experimental data, parameters B and m are generally taken to be functions of temperature while n is viewed as temperature-independent (e.g. [18,19]). Here, B is assumed to follow a general expression of Arrhenius-type:

$$B = b_0 \exp\left(-\frac{Q}{RT}\right) \quad (26)$$

where b_0 is a constant, Q is the activation energy for creep, R is the gas constant and T is temperature in Kelvin scale. Extension of uniaxial case to multiaxial case is made by introducing effective quantities such that

$$\bar{\epsilon}^{cr} = B \bar{\sigma}^{m(T)} t^n \quad (27)$$

where $\bar{\sigma}$ is the effective stress defined in eq. (18).

The path-dependent creep process is incorporated into the model through the use of the flow rate which describes the creep strain components, ϵ_{ij}^{cr} , in terms of the stress deviator tensor, S_{ij} , i.e.

$$\dot{\epsilon}_{ij}^{cr} = \lambda S_{ij} \quad (28)$$

The use of the deviatoric stress components, S_{ij} in the above equation ensures that creep deformation is independent of the hydrostatic state of stress as have been observed experimentally. In this equation, the proportionality factor, λ , is defined as:

$$\lambda = \frac{3}{2\bar{\sigma}} \frac{d\bar{\epsilon}^{cr}}{dt} = n B \bar{\sigma}^{m(T)} t^{n-1} \quad (29)$$

The strain history prediction in this analysis follows the "strain hardening" formulation in which the creep strain rate in a variable stress situation depends on the stress, strain and temperature. Eliminating time from eq.(29) with the aid of eq.(25), the flow rule can be rewritten as:

$$\dot{\epsilon}_{ij}^{cr} = \frac{3}{2} n B^{\frac{1}{n}} \bar{\sigma}^{\frac{m}{n}} (\bar{\epsilon}^{cr})^{\frac{n-1}{n}} \frac{S_{ij}}{\bar{\sigma}} = \frac{3 F}{2 \bar{\sigma}} S_{ij} \quad (30)$$

where F is a scalar defined as:

$$F = n B^{\frac{1}{n}} \bar{\sigma}^{\frac{m}{n}} (\bar{\epsilon}^{cr})^{\frac{n-1}{n}} \quad (31)$$

It can be shown using eqs. (27) and (29) that:

$$\bar{\epsilon}^{cr} = \left(\frac{2}{3} \dot{\epsilon}_{ij}^{cr} \dot{\epsilon}_{ij}^{cr} \right)^{\frac{1}{2}} = F \quad (32)$$

thus, the flow rule can now be expressed in differential form as:

$$d\epsilon_{ij}^{cr} = \frac{3}{2} \frac{d\bar{\epsilon}^{cr}}{\bar{\sigma}} S_{ij} \quad (33)$$

This equation can be written explicitly for the three components of the constraint-free creep strain increments as:

$$\begin{aligned} \Delta \epsilon_{rr}^{cr} &= \frac{\Delta \bar{\epsilon}^{cr}}{2\bar{\sigma}} (2\sigma_{rr} - \sigma_{\theta\theta} - \sigma_{zz}) \\ \Delta \epsilon_{\theta\theta}^{cr} &= \frac{\Delta \bar{\epsilon}^{cr}}{2\bar{\sigma}} (2\sigma_{\theta\theta} - \sigma_{rr} - \sigma_{zz}) \\ \Delta \epsilon_{zz}^{cr} &= \frac{\Delta \bar{\epsilon}^{cr}}{2\bar{\sigma}} (2\sigma_{zz} - \sigma_{rr} - \sigma_{\theta\theta}) \end{aligned} \quad (34)$$

where the effective creep strain increment, $\Delta \bar{\epsilon}^{cr}$, occurring over the time increment, Δt is approximated from uniaxial creep behavior given by eq. (27) as:

$$\Delta \bar{\epsilon}^{cr} = B \bar{\sigma}^{m(T)} \Delta t^n \quad (35)$$

The axisymmetric creep strain components are represented by the effective value defined as:

$$\bar{\epsilon}^{cr} = \frac{\sqrt{2}}{3} \left[\left(\epsilon_{rr}^{cr} - \epsilon_{\theta\theta}^{cr} \right)^2 + \left(\epsilon_{\theta\theta}^{cr} - \epsilon_{zz}^{cr} \right)^2 + \left(\epsilon_{zz}^{cr} - \epsilon_{rr}^{cr} \right)^2 \right]^{\frac{1}{2}} \quad (36)$$

Constraint-free creep deformation in the matrix and the composite media, as described above, is coupled with the existence of perfect bonding at layer interfaces and the relative inextensibility of the reaction zone and the fiber. Consideration of creep behavior of the composite, therefore, results in inhomogeneous Euler equation as described by eq. (8) but without the plastic strain terms in the loading function, $\Phi^{(i)}(r)$ of eq. (9). The solution for the displacement field is obtained by assuming that the radial variation of the constraint-free creep strain increments in the matrix and the outermost equivalent composite media can each be represented as a third order polynomial as follows:

$$\begin{aligned} \Delta \epsilon_{rr}^{(i),cr} &= a_1^{(i)} + a_2^{(i)} r + a_3^{(i)} r^2 + a_4^{(i)} r^3 \\ \Delta \epsilon_{\theta\theta}^{(i),cr} &= b_1^{(i)} + b_2^{(i)} r + b_3^{(i)} r^2 + b_4^{(i)} r^3 \\ \Delta \epsilon_{zz}^{(i),cr} &= c_1^{(i)} + c_2^{(i)} r + c_3^{(i)} r^2 + c_4^{(i)} r^3 \end{aligned} \quad (37)$$

where the coefficients $a_1^{(i)} \sim a_4^{(i)}$, $b_1^{(i)} \sim b_4^{(i)}$, and $c_1^{(i)} \sim c_4^{(i)}$ ($i = 1, 2$) are obtained from least-squared curve fit procedures. This assumption dictates the form and order of the particular solution for the displacement field in the creeping layers. Upon substitution of eqs. (37) into eq. (9), the governing differential equations for the deformation of the composite in the case of elastic-plastic-creep can be written as:

$$r^2 \frac{d^2 u^{(i)}}{dr^2} + r \frac{du^{(i)}}{dr} - u^{(i)} = \phi_1^{(i)} r + \phi_2^{(i)} r^2 + \phi_3^{(i)} r^3 + \phi_4^{(i)} r^4, \quad \frac{dw^{(i)}}{dz} = 0 \quad (38)$$

where the coefficients, $\phi_1^{(i)} \sim \phi_4^{(i)}$ consists of material constants for the i^{th} layer. For the elastic fiber and interphase zone, these coefficients are zero. The solution of the above equations which corresponds to the displacement field with creep deformation in the matrix and the equivalent composite media are obtained as:

$$u^{(i),mc} = A_i r + \frac{B_i}{r} + \frac{\phi_1^{(i)}}{2} \ln r + \frac{\phi_2^{(i)}}{3} r^2 + \frac{\phi_3^{(i)}}{8} r^3 + \frac{\phi_4^{(i)}}{15} r^4, \quad w^{(i)} = Lz \quad (39)$$

The stress field in the composite for the elastic-plastic-creep case accumulate incrementally throughout the cooling process. The expressions for this stress field are obtained with the aid of the strain-displacement relations and the above displacement field as follows:

$$\begin{aligned} \sigma_{rr}^{(i),mc} = K^{(i)} & \left[A_i - (1 - 2\nu^{(i)}) \frac{B_i}{r^2} + \nu^{(i)} L - (1 + \nu^{(i)}) \epsilon^{(i),th} \right. \\ & + (1 - \nu^{(i)}) \frac{\phi_1^{(i)}}{2} + \frac{\phi_1^{(i)}}{2} \ln r + (2 - \nu^{(i)}) \frac{\phi_2^{(i)}}{3} r + (3 - 2\nu^{(i)}) \frac{\phi_3^{(i)}}{8} r^2 \\ & \left. + (4 - 3\nu^{(i)}) \frac{\phi_4^{(i)}}{15} r^3 - (1 - \nu^{(i)}) \epsilon_{rr}^{(i),mc} - \nu^{(i)} \epsilon_{\theta\theta}^{(i),mc} - \nu^{(i)} \epsilon_{zz}^{(i),mc} \right] \\ \sigma_{\theta\theta}^{(i),mc} = K^{(i)} & \left[A_i + (1 - 2\nu^{(i)}) \frac{B_i}{r^2} + \nu^{(i)} L - (1 + \nu^{(i)}) \epsilon^{(i),th} \right. \\ & + \nu^{(i)} \frac{\phi_1^{(i)}}{2} + \frac{\phi_1^{(i)}}{2} \ln r + (1 + \nu^{(i)}) \frac{\phi_2^{(i)}}{3} r + (1 + 2\nu^{(i)}) \frac{\phi_3^{(i)}}{8} r^2 \\ & \left. + (1 + 3\nu^{(i)}) \frac{\phi_4^{(i)}}{15} r^3 - (1 - \nu^{(i)}) \epsilon_{\theta\theta}^{(i),mc} - \nu^{(i)} \epsilon_{rr}^{(i),mc} - \nu^{(i)} \epsilon_{zz}^{(i),mc} \right] \quad (40) \end{aligned}$$

$$\sigma_{zz}^{(i),mc} = K^{(i)} \left[2\nu^{(i)} A_1 + (1 - \nu^{(i)}) L - (1 + \nu^{(i)}) \epsilon^{(i),th} + \nu^{(i)} \frac{\phi_1^{(i)}}{2} + \nu^{(i)} \phi_1^{(i)} \ln r + \nu^{(i)} \phi_2^{(i)} r \right. \\ \left. + \nu^{(i)} \frac{\phi_3^{(i)}}{2} r^2 + \nu^{(i)} \frac{\phi_4^{(i)}}{3} r^3 - (1 - \nu^{(i)}) \epsilon_{zz}^{(i),mc} - \nu^{(i)} \epsilon_{rr}^{(i),mc} - \nu^{(i)} \epsilon_{\theta\theta}^{(i),mc} \right]$$

Applying the same boundary conditions specified earlier results in a similar set of eight simultaneous equations as arranged in eq. (17), but with additional terms in the load vector, **d** resulting from creep contributions, i.e.

$$\mathbf{A} \mathbf{c} = \mathbf{d} \quad (41)$$

This equation should be solved for the unknown constants, $A_1 \sim A_4$, $B_1 \sim B_4$ and L appearing in the vector **c**.

3.4 SOLUTION PROCEDURES

The algorithm for the determination of thermal stresses in MMC is shown in Fig. 3-4. It initially reads the model geometry, cooling rate and temperature dependent material data from a tabular input file. Starting with an initial stress and strain free states at consolidation temperature, the first load step is initiated which consists of a negative temperature increment followed by a time step. The stiffness equation, eq. (17) is solved for elastic stress increments induced over the temperature drop. A yield limit is determined for the present temperature and compared with the effective stress in the matrix. If the effective stress is less than the yield limit, the procedure proceeds to calculate creep strain increments for the matrix and the outermost equivalent composite media. Otherwise, plasticity calculations are executed in which the plastic modulus, $H(T)$, and the effective Poisson's ratio, η , are determined using the current values of the effective stress and strain in eq. (23) and eq. (20), respectively. They are substituted for the elastic modulus, $E(T)$, and the Poisson's ratio, ν , respectively in the stiffness matrix of eq. (17). These equations are then solved for the new stress and strain increments in all layers due to matrix plasticity and the latter is compared with the previous value. If the difference is less than a prescribed value, plasticity calculations are completed. Otherwise, new values for $H(T)$ and η are established and plasticity calculations are repeated until convergence of the incremental effective strain is achieved.

The procedure then performs the creep analysis of the composite over the proceeding time increment. During the first Δt step, the constraint-free creep strain increments for the matrix and the composite media are initially calculated using eqs. (34) with the previously calculated stress acting in the respective layers. The distribution of each component of the creep strain increment across the matrix layer and the equivalent composite media are fitted to polynomials as described by eqs. (37). The creep effect is accommodated in the load vector, **d** of eq. (41) and the resulting stiffness equation, is solved for the constrained deformation of all layers due to creep. Since temperature decreases and time proceeds simultaneously during the consolidation stage of the composite, employing the average of the stress increments from elastic-plastic calculation and

the creep calculation should provide a better estimate of the constrained creep deformation. This is utilized in the second estimation of the creep strain increments, and the resulting stress increments due to constrained creep deformation in the matrix and the equivalent composite media are used in the next iteration. Convergence of the iterative process is achieved when the difference between the incremental creep strain in the matrix from the last two successive iterations are within a small prescribed value.

The stress and strain increments from both the elastic-plastic and the creep calculations are then summed to represent the total thermal stress and strain at the beginning of the next load step.

For any subsequent load step, the elastic stress increments occurring over the current temperature increment is summed with the previously accumulated thermal stress until the last load step. This (effective) stress is then used to determine the occurrence of plastic flow in the matrix at the current temperature. The sum of the stress increments from the elastic-plastic calculations and the previously accumulated thermal stress is used to provide the first estimate of the constraint-free creep strain increment in the matrix and the equivalent composite media. Equation (41) is again solved to provide the constrained creep deformation in these layers and the resulting stress increments in all layers due to creep. The average of the resulting stress increments due to creep and the stress increments from elastic-plastic calculations are summed with the previously accumulated stress for the next estimate of the constraint-free creep strain. The iteration process continues until convergence is achieved.

The accumulated stress and strain values at the current temperature are written to output files. The next load step is then incremented and the process continues until room temperature is reached.

The history of the accumulated creep strain in both the matrix and the equivalent composite media, as mentioned before is based on the strain hardening creep formulation in which the creep strain rate is assumed to be a function of stress, strain and temperature. This history is schematically illustrated in Fig. 3-5 in terms of effective stress and strain values for the first two load steps. During the initial load step from consolidation temperature, constraint-free creep strain increment, $\Delta \bar{\epsilon}_1^c$, occurring over time increment Δt_1 , is estimated using eqs. 33- 35 and indicated as open circle (point 1) on the creep curve corresponding to load condition $(\bar{\sigma}_1, T_1)$. Physical constraints imposed by the existence of perfectly bonded interfaces and non-creeping phases modify the magnitude of $\Delta \bar{\epsilon}_1^c$ to a lower value $\Delta \bar{\epsilon}_1^{mc}$ (point 2). This latter strain must fall on the creep curve corresponding to current stress and temperature levels. This would then lead to the determination of point 3. In the second load step, as the stress increases to $\bar{\sigma}_2$, the end response of the load step, following the strain hardening concept, is shifted horizontally to point 4 which marks the onset of the creep flow of the unconstrained matrix and equivalent composite material along the creep curve corresponding to load condition $(\bar{\sigma}_2, T_2)$. Tracing this curve for the duration Δt_2 would define point 5. Again, this point under constrained deformation condition would be modified to point 7 along the path 5-6-7. The strain magnitude generated between the points 4 and 7 thus represents the actual $\Delta \bar{\epsilon}_2^{mc}$ occurring during the second load step. This path 4-7 must be shifted horizontally to have its starting position initiating at point 3. This would then generate the curve 3-8 for which point 8 marks the starting position for the third load step. The total creep strain accumulated in the matrix at the end of the second load step, $\bar{\epsilon}_2^{mc}$, is then the sum of $\Delta \bar{\epsilon}_1^{mc}$ and $\Delta \bar{\epsilon}_2^{mc}$. This procedure is repeated for all load steps between consolidation temperature and end temperature level.

The composite may be subjected to thermal fatigue in order to reduce the magnitude of the thermal residual stress induced during post-fabrication cool down. Throughout these processes, creep deformation is expected to progress.

3.5 SUMMARY AND CONCLUSIONS

In this section, a new micromechanical stress analysis approach has been proposed which considers time-dependent behavior of a continuous-fiber-reinforced MMC during post-fabrication cool down and subsequent thermal fatigue. A four-phase concentric cylinder model consisting of an embedded fiber and an interphase zone which behave elastically, while the matrix and the equivalent composite media may experience plasticity and creep was employed in the formulation. All the constituent phases of the composite model are assumed to be isotropic. The conceptual uniaxial four-bar model has illustrated that the deformation behavior of the composite can be isolated into time-independent and time-dependent deformation and treated separately for mathematical convenience. The former considers elastic-plastic deformation occurring over discrete temperature change, while the latter emphasizes creep response of the matrix and the equivalent composite media over the corresponding duration of time. Both effects are then combined at the end of each discrete load step. The tensile thermal stress induced in the matrix due to mismatches of the CTEs of the matrix and other constituents of the composite is lowered through the evolution of the compressive stress set-up in the matrix due to constrained creep deformation at elevated temperature. The occurrence of matrix plasticity is treated using the deformation theory of plasticity with total strain increment (elastic plus plastic) in conjunction with the von Mises yield criterion. Strain hardening characteristics of the matrix material are represented by the tangent modulus of the stress-strain curve beyond the initial yield point and the corresponding effective Poisson's ratio. Constraint-free creep deformation of the matrix and the equivalent composite media is estimated using the Bailey-Norton law in the transient and steady-state stages of creep. An Arrhenius-type expression is used for the time-dependent creep coefficient of the creep law. Constrained creep deformation in the composite is calculated using the "stiffness" method with modified load vector resulting in stress redistribution in all layers due to creep. The creep strain history prediction followed the strain hardening formulation which assumed the creep strain rate to be dependent on stress, strain and temperature. The model has been used in a parametric study and the results will be discussed in the next section.

The present micromechanical analysis can be extended to predict the variation of stress and strain states in the fiber, the interphase zone and the matrix when subjected to thermo-mechanical loadings. External radial pressure and axial stress can be accommodated through the boundary conditions in eqs. (10) and (11), respectively. In addition, non-uniform temperature distribution across a layer can be specified by the temperature gradient through the right-hand side of the governing equation (8). This will result in additional terms in the load vector, \mathbf{b} and \mathbf{d} of eq. (17) and (41), respectively. Extension of the model to n -layers can be made with additional boundary conditions on the continuity of the radial displacements and radial stresses specified at each new interface. An additional pair of unknown constants and hence additional two new equations in the stiffness equation, eq. (41) are associated with each new layer.

3.6 REFERENCES

1. Saigal, A., Kupperman, D. S. and Majumdar, 1992. Mat. Sc. Engng.,:59-66.
2. Min, B. K., 1981. J. The Mechanics and Physics of Solids, 29:327-352.
3. Min, B. K. and Crossman, F. W., 1982. Composite Materials: Testing and Design (Sixth Conf), ASTM STP 787, ed. by Daniel, I. M., Am Soc for Testing and Materials, :371-392.
4. Hecker, S. S., Hamilton, C. H. and Ebert, L. J., 1970. J. Materials, JMLSA, 5,No.4:868-900.
5. Uemura, M., Iyama, H. and Yamaguchi, Y., 1979. J. Thermal Stresses, 2:393-412.
6. Mikata, Y. and Taya, M., 1985. J. Composite Materials, 19:554-578.
7. Jayaraman, K. and Reifsnider, K. L., 1992. J. Composite Materials, 26,No.6:771-791.
8. Yang, J. M. and Jeng, S. M., 1989. J. Metals, Nov.:56-59.
9. Gundel, D. B. and Wawner, F. E., 1991. Scripta Metallurgica et Materialia, 25:437-441.
10. Theocaris, P., 1985. Advances in Polymers Science, ed. by Kausch, H. H. and Zachmann, H. G., Springer-Verlag, Berlin, 66:149-187.
11. Nairn, J. A., 1985. Polymer Composites, 6:123-130.
12. Jansson, S. and Leckie, F. A., 1992. J. Composite Materials, 26:1474-1486.
13. Hashin, Z. and Rosen, B. W., 1964. J. Applied Mechanics, 31:223-232.
14. Christensen, R. M. and Lo, K. H., 1979. J. The Mechanics and Physics of Solids, 27:315-330.
15. Min, B. K. and Crossman, F. W., 1982. J. Composite Materials, 16:188-203.
16. Gayda, J., Gabb, T. P. and Freed, A. D., 1990. Fundamental Relationships Between Microstructure and Properties of Metal Matrix Composites, ed. by Liaw, P.K. and Gungor, M.N., The Mineral, Metal and Materials Society, Warrendale, PA:497-513.
17. Hecker, S. S., Hamilton, C. H. and Ebert, L. J., 1969. Metallurgica, 3:793-798.
18. Kraus, H., 1980. Creep Analysis, John Wiley and Sons, Inc., NY.
19. Lemaitre, J. and Chaboche, L., 1990. Mechanics of Solid Materials (English Translation), Cambridge University Press, NY.

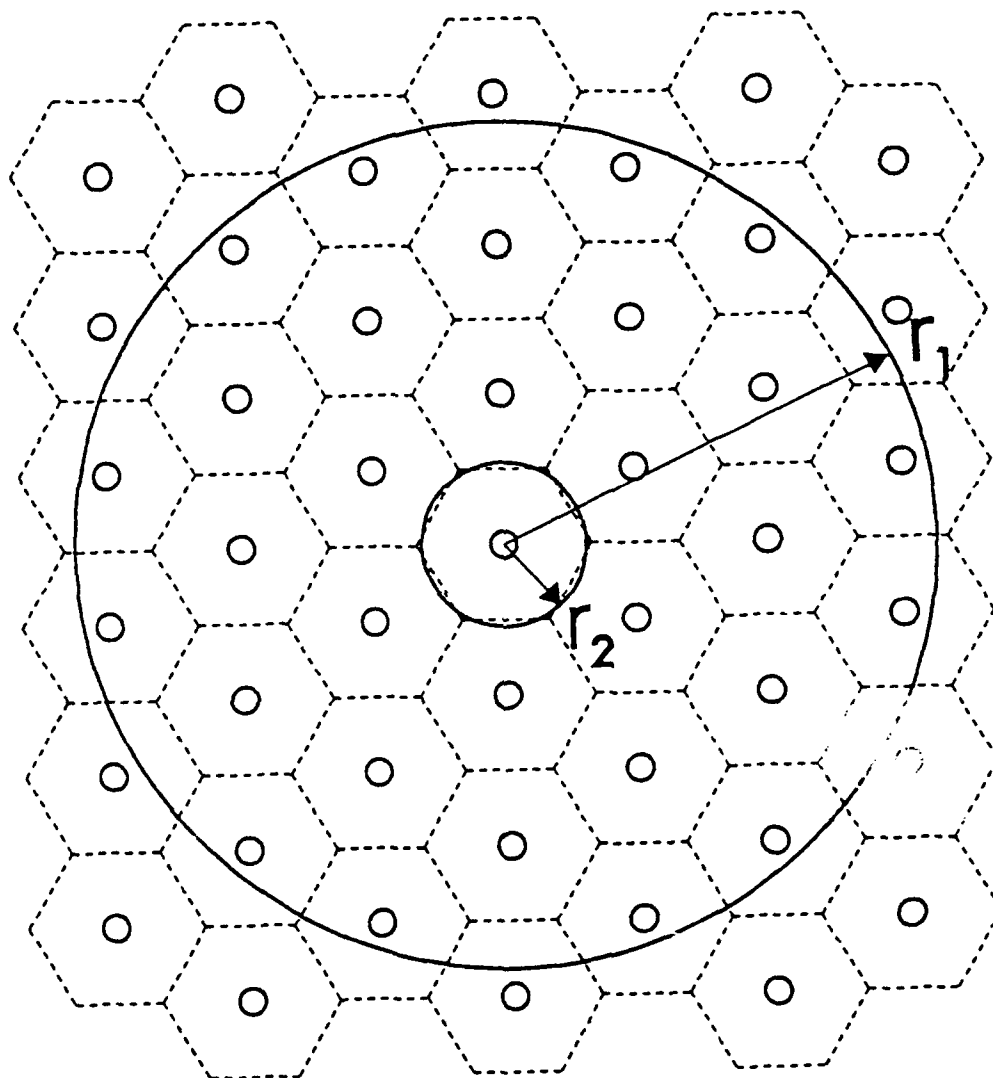


Fig. 3-1(a) Selected configuration of a unit cell with surrounding composite material.

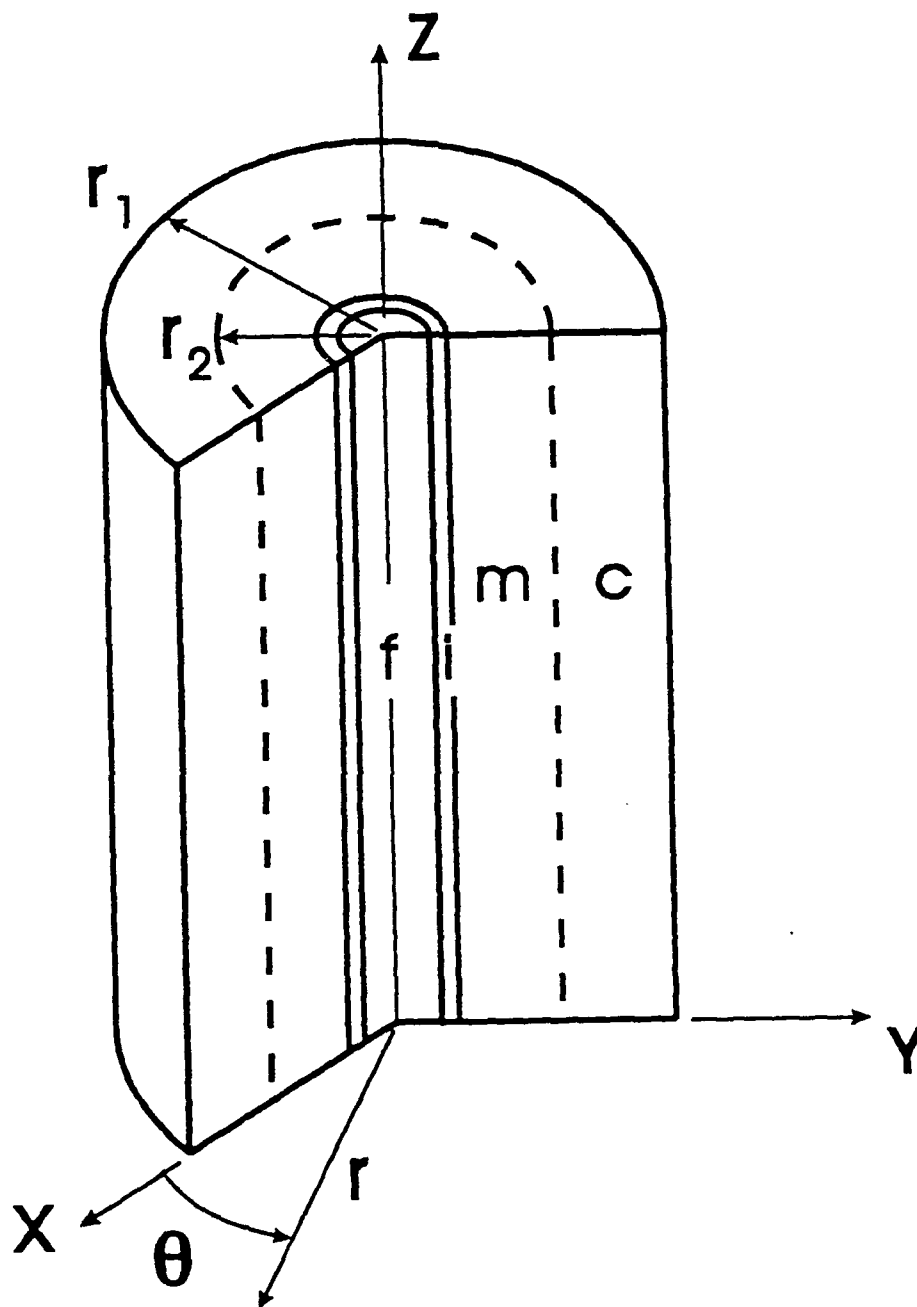


Fig. 3-1(b) Cut-out section of the four-phase model.

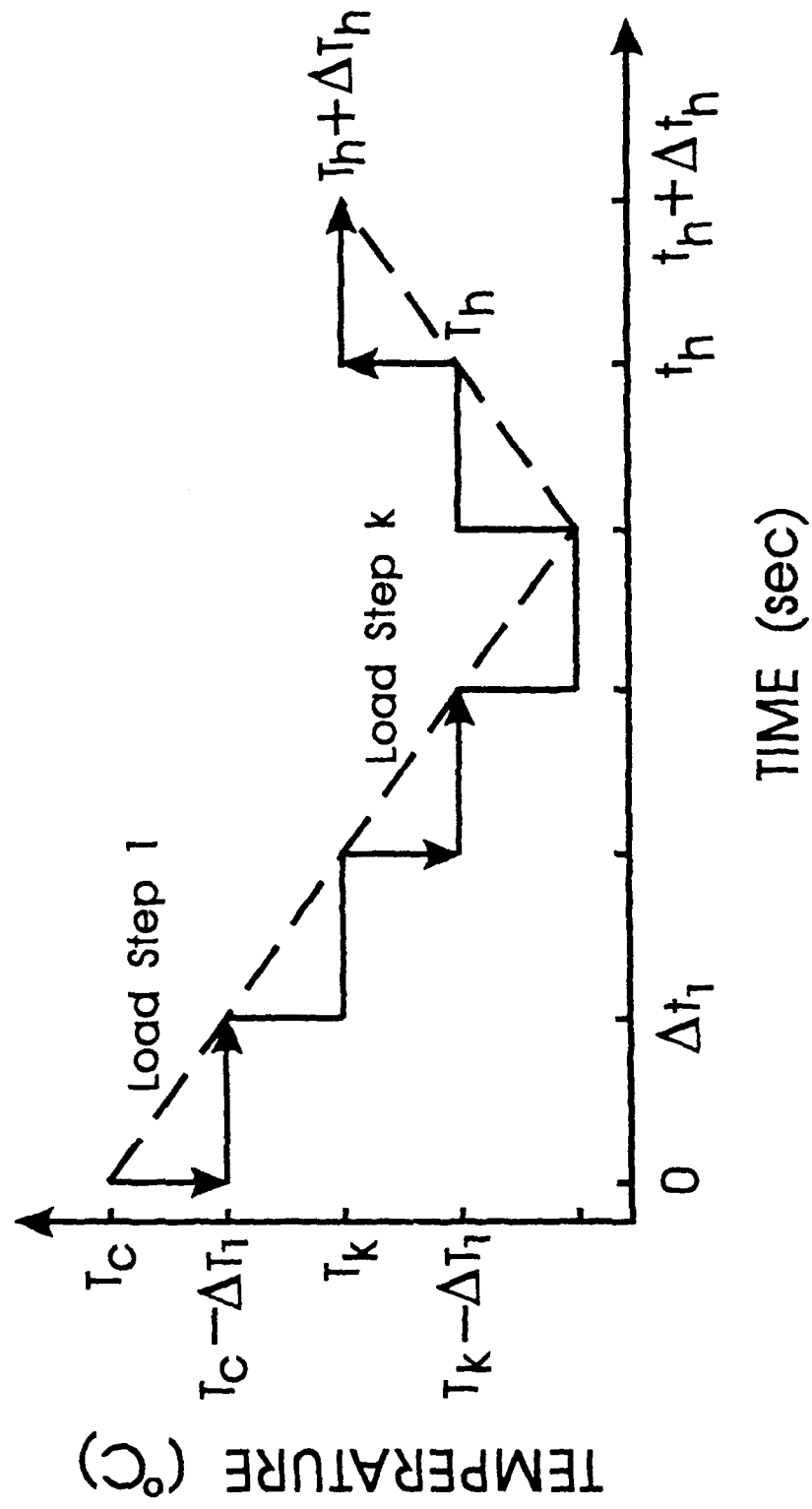


Fig. 3-2 Discretization of the cooling/heating path (no externally applied mechanical load).

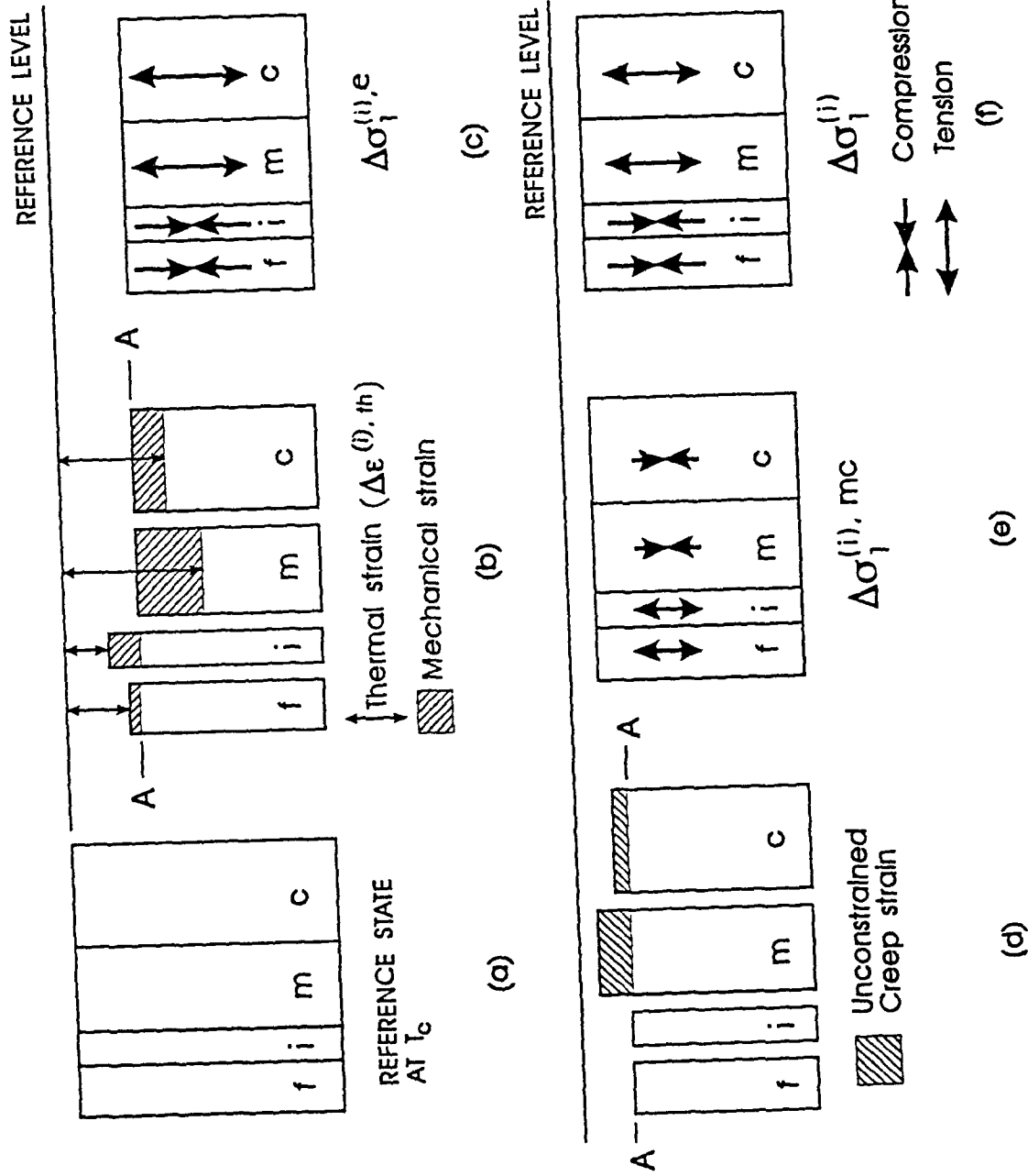


Fig. 3-3 (a) Reference state at consolidation. (b) Constraint-free thermal deformation. (c) Equilibrium conditions due to boundary constraints. (d) Constraint-free creep deformation. (e) Equilibrium conditions due to boundary constraints. (f) Final equilibrium conditions at the end of the first temperature-time step loading (sum of conditions at (c) and (e)).

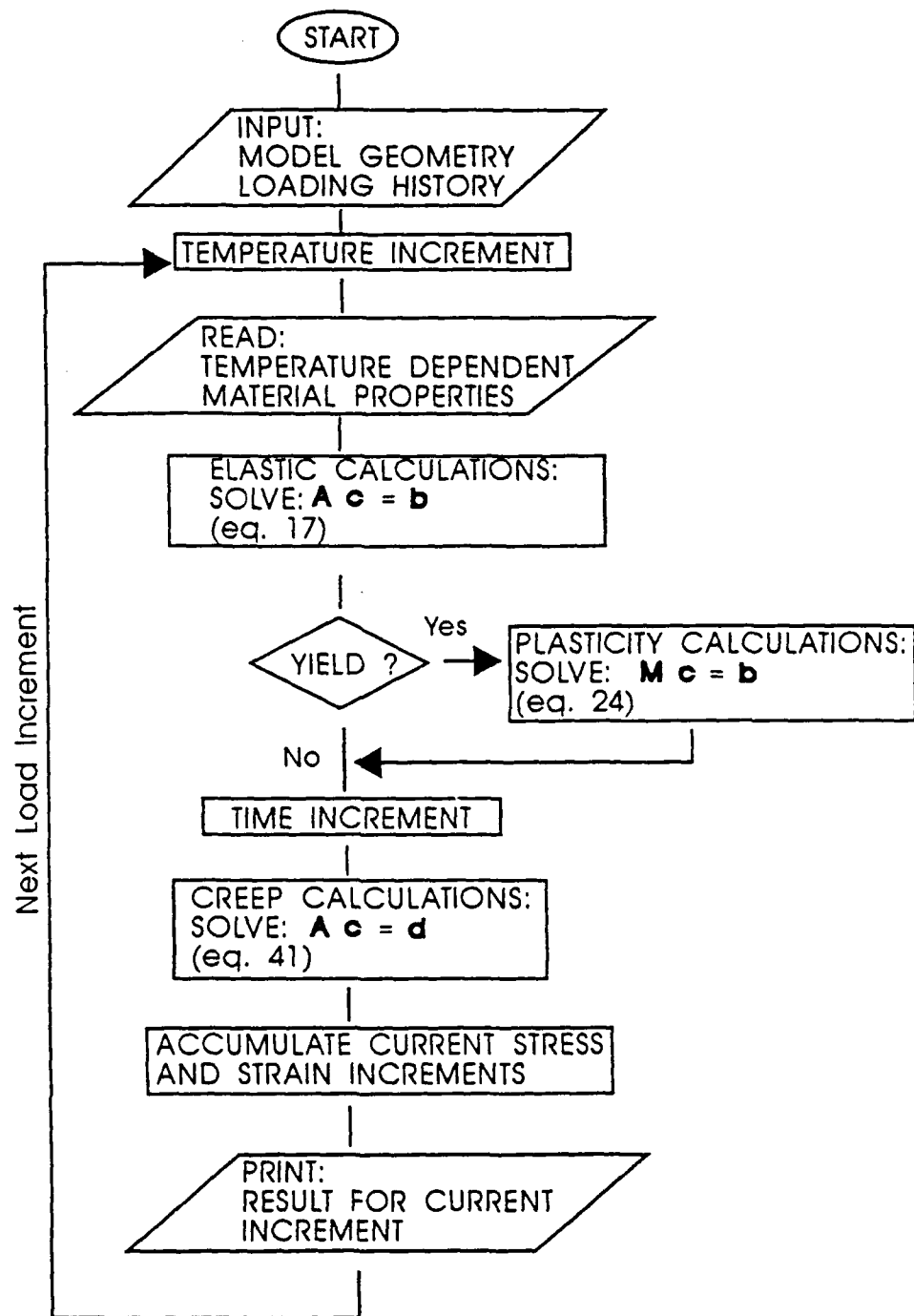


Fig. 3-4 Flow charts for elastic-plastic-creep algorithm.

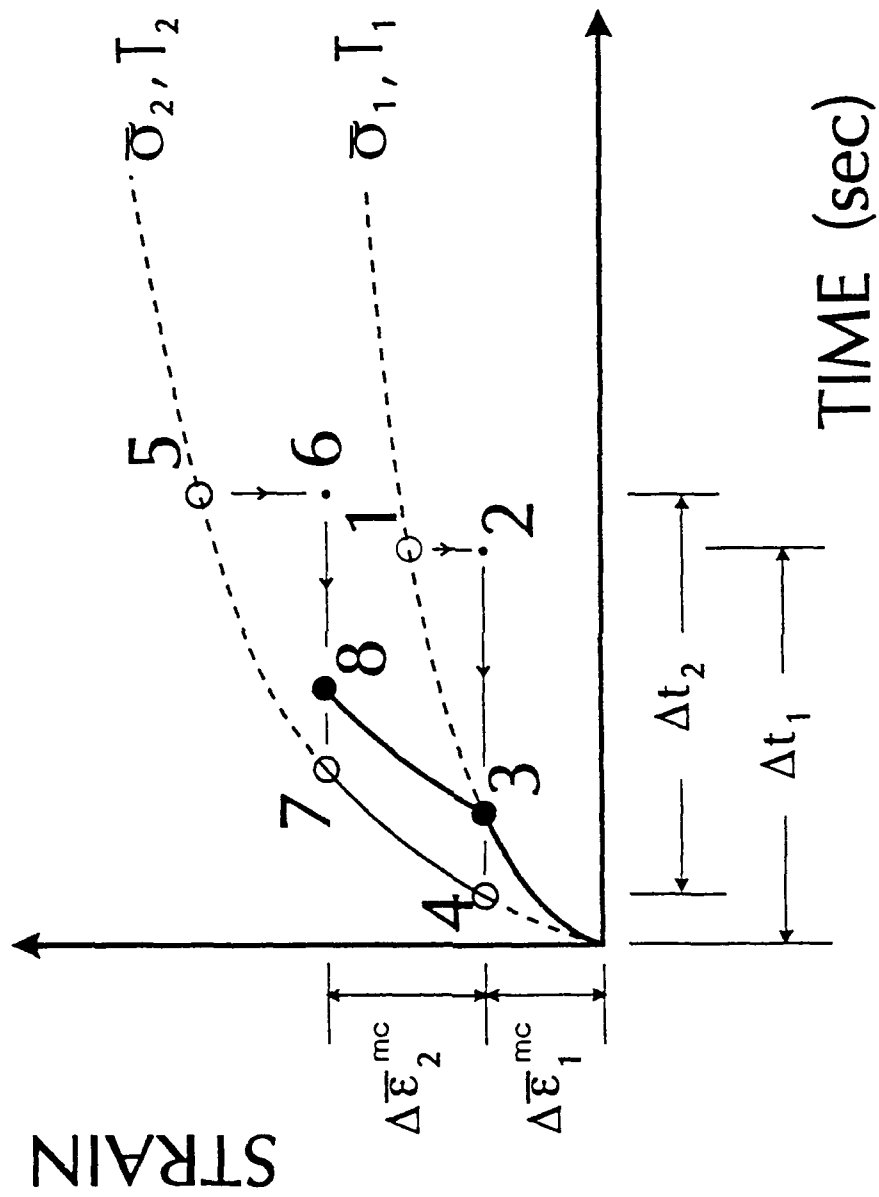


Fig. 3-5 Strain history prediction for the first two load steps from strain hardening method.

SECTION 4

PARAMETRIC STUDY OF THE TIME-DEPENDENT BEHAVIOR OF CONTINUOUS-FIBER REINFORCED METAL MATRIX COMPOSITES BASED ON MICROMECHANICAL MODEL⁴

ABSTRACT

The micromechanical model developed in section 3 for the evaluation of the time-dependent stress-strain response of continuous-fiber-reinforced MMCs is applied to the SCS-6/Timetal 21S composite system. The influence of several parameters were examined; they include the thickness of the equivalent composite media, the type of fiber coating material, the thickness of the reaction zone, cooling rate from the consolidation temperature and the kinetics of the creep process during thermal cyclic loading. Results of this application show that the optimum ratio of the radii of composite media to that of the matrix layer should be larger than seven. At this ratio, sufficient fiber interactions is provided by the equivalent composite media. The analysis also indicates that the process-induced thermal stresses in the matrix can be relaxed due to creep during initial cool-down from fabrication. This stress reduction is enhanced at a slower cooling rate. Furthermore, the study of the role of different fiber coating materials shows that Copper coating is most effective in lowering the tensile stress components in the matrix when compared to Niobium, porous TiB_2 and Amorphous Carbon. The effectiveness increases with increasing thickness of the interfacial region. TiB_2 and Niobium coatings are favorable because they induce compressive radial stress in the brittle interfacial region and the matrix. The effect of thermal cycles subsequent to initial cool-down has been analyzed. It is found that the matrix thermal activation energy, Q , is history dependent and can be correlated with the level of the accumulated creep strain in the matrix layer. Furthermore, the residual thermal stresses in the matrix due to cool-down from consolidation can be fully relaxed by the thermal fatigue process.

4.1 INTRODUCTION

A micromechanical approach which takes into account the influence of time dependent effects on the evolution of thermal stresses in continuous fiber-reinforced metal matrix composites (MMCs) was developed in the previous section [1]. This approach which adopts the four-phase concentric cylinder model is able to provide information on the stress and strain states as well as their evolution in each constituent of the composite during the loading history.

A critical aspect of this approach is the inclusion of the creep deformation developed in the matrix and the effective composite media due to thermal variations. This inelastic deformation is described through the use of the Bailey-Norton's equation which accounts for the primary and secondary creep stages. A numerical scheme based on the "strain-hardening" creep formulation is employed to predict the accumulation of creep strain during the simultaneous variation of both

⁴ based on "Time-dependent behavior of continuous-fiber-reinforced metal matrix composites, part II: parametric study", M. Tamin, D. Zheng and H. Ghonem, submitted to Composite Material & Technology, 1993.

stress and temperature in the composite.

In this section, the model is applied to SCS-6/Timetal 21S composite system under the thermal loading conditions which include cooling from processing temperature and subsequent thermal cycling. Through this application, an attempt has been made to identify the key parameters in the model and their physical significance. The minimum size of the equivalent composite media necessary to account for the effect of fibers interaction in the composite is investigated. MMCs with different fiber coating materials and various thickness are modelled to study their effects on the thermal stress level in the constituents of the composite. The significant influence of time-dependent behavior of MMCs during initial cool-down and subsequent thermal fatigue are also studied. In addition, effects of different cooling rates during consolidation on the residual thermal stress level in the composite are considered. The characteristics of the stress state in the fiber, the reaction zone and the matrix during consolidation and subsequent thermal cycles are presented. Finally, certain interesting features of the thermal stresses in the composites revealed from the application of the model to thermal fatigue conditions are discussed.

4.2 PARAMETRIC STUDY

The composite employed for the model here is the Titanium-based SCS-6/Timetal 21S composite system. The Silicon Carbide fiber reinforcement, SCS-6 is assumed to behave elastically for all loading conditions with temperature-independent elastic modulus and Poisson's ratio. The coefficient of thermal expansion (CTE) is taken as temperature-dependent [2-6]. The reaction zone formed between the fiber and the matrix with a thickness of 3 μm is assumed to have mechanical and thermal properties similar to those of the fiber coating material used. The elastic modulus, CTE, and yield limit of the metastable Timetal 21S monolithic matrix alloy were also considered to be temperature-dependent [7]. The properties of the equivalent composite media were obtained using the rule of mixture for fiber volume fraction of 35%. The volume fractions of the fiber, v_f , the reaction zone, v_{re} , and the matrix, v_m , are expressed as:

$$v_f = \left(\frac{r_4}{r_2} \right)^2, \quad v_{re} = \frac{r_3^2 - r_4^2}{r_2^2}, \quad v_m = 1 - \left(\frac{r_3}{r_2} \right)^2 \quad (1)$$

where r_1 , r_2 , r_3 and r_4 are the radii of the equivalent composite media, the matrix, the reaction zone and the fiber, respectively. The mechanical properties of all the constituents of the composite are shown in Fig. 3-1(a)-(c).

Both the monolithic matrix and the composite exhibit creep behavior during consolidation. The creep properties of Timetal 21S monolithic matrix and the composite material are based on limited experimental data given in reference [7,8]. It is assumed that the creep curves can be represented by the Bailey-Norton's equation in the transient and the steady state stages of creep as:

$$\bar{\epsilon}^{cr} = B \bar{\sigma}^{m(T)} t^n \quad (2)$$

where $\bar{\epsilon}^{cr}$ and $\bar{\sigma}$ are the effective creep strain and the effective stress, respectively. The

parameters B , $m(T)$ and n are obtained from correlations with the experimental data. The coefficient, B can be expressed by an Arrhenius-type expression:

$$B = b_0 \exp\left(-\frac{Q}{RT}\right) \quad (3)$$

where b_0 is a constant, R is the gas constant, Q is the thermal activation energy and T is temperature in degrees Kelvin. The stress exponent, $m(T)$, which is treated as a function of temperature is described as a polynomial function in the form [9]:

$$m(T) = A_1 + A_2 T + A_3 T^2 + A_4 T^3 \quad (4)$$

where A_i , ($i=1,2,3,4$) are material constants.

Due to lack of creep data for the SCS-6/Timetal 21S composite, the creep response of the equivalent composite media under thermal loading conditions is estimated from the matrix creep data by accounting for the effect of fiber reinforcement in the following manner:

$$\epsilon_{rr}^{(1),cr} = (1 - v_f) \epsilon_{rr}^{(2),cr}, \quad \epsilon_{\theta\theta}^{(1),cr} = (1 - v_f) \epsilon_{\theta\theta}^{(2),cr}, \quad \epsilon_{zz}^{(1),cr} = (1 - v_f) \epsilon_{zz}^{(2),cr} \quad (5)$$

where $\epsilon_{rr}^{(1),cr}$, $\epsilon_{\theta\theta}^{(1),cr}$ and $\epsilon_{zz}^{(1),cr}$ are the radial, hoop and axial component, respectively, of the unconstrained creep strain for the composite while $\epsilon_{rr}^{(2),cr}$, $\epsilon_{\theta\theta}^{(2),cr}$ and $\epsilon_{zz}^{(2),cr}$ are the corresponding creep strain components for the matrix.

The first part of this section will deal with the thickness of the equivalent composite media surrounding the matrix, the reaction zone and the embedded fiber. The effect of the reaction zone thickness and different types of fiber coating materials on the stress states in the matrix and the reaction zone will be examined next. This will be followed by analysis related to the role of creep deformation and the response of the matrix activation energy to thermal loadings. In this section, the stress fields in the matrix and the reaction zone are calculated in the vicinity of the matrix/reaction zone interface.

4.2.1 Thickness of the Equivalent Composite Media

As described in the last section, the geometry of the model adopted in the present approach consists of a fiber surrounded by a reaction zone and the matrix layer, and embedded in an unbounded homogeneous media that has the properties of the composite. This model is the counterpart for multi-phase media of the self-consistent method for single phase media [10]. Theoretically, the equivalent composite media surrounding the matrix cylinder should be infinitely large, and generally the numerical techniques take this size fairly large to meet infinite requirement. The choice of a large equivalent composite media leads to a stable stress field solution at the expense of longer computational time and larger required computer memory. Fig. 4-2(a)~(c) show the relationship between the stress fields in the matrix layer and the size of the equivalent composite media in terms of the ratio of the radii of the matrix to the surrounding equivalent composite media. The stresses are normalized by $\sigma_0 = E^{(2)}\alpha^{(2)}\Delta T$, where $E^{(2)}$ and $\alpha^{(2)}$ are the Young's modulus and CTE, respectively of the matrix at room temperature, and ΔT is 840 °C. It indicates that the stress fields of the phases are stable until the ratio is less than seven,

and this trend is not affected by the fiber volume fraction. The significance of this ratio of seven could be explained in terms of the minimum number of fibers that should be contained in the optimum thickness of the composite media for the model. In the real composite, the fibers are not regularly align in the matrix. The distribution of the center-to-center fiber spacing for a typical SCS-6/Ti-15-3 composite with 35% fiber volume fraction can be obtained using the method of quantitative stereology [11] as illustrated in Fig. 4-3. The mean center-to-center fiber spacing for this composite is 230 μ m. Assuming that the fiber arrangement follows the hexagonal array with the fiber, the reaction zone and the matrix cylinders at the center of the arrangement, then other fibers are arranged in series of concentric hexagonal arrays about this center as depicted in Fig. 4-4. The minimum diameter of the equivalent composite media is also illustrated in the figure. It can be shown that for the hexagonal array architecture, the minimum size of the equivalent composite media consists of 40 fibers surrounding the embedded fiber which is being modelled (see Fig. 4-4). This provides sufficient effects of interaction of fibers in the composite.

4.2.2 Fiber Coating Material and Thickness of the Interfacial Region

Previous work [5,6,12] showed that the reaction zone in the composites is a susceptible site for generating cracks after fabrication. Microscopic radial cracks after fabrication are frequently observed in several titanium metal matrix composites. These cracks are caused by the high level of tensile hoop stress component induced in the reaction zone during consolidation [13]. The popular criteria for selecting coating material are currently based on the enhancement of wetting behavior of fiber and matrix and the minimization of interface reactions by reducing the rate of diffusion [14]. Besides being an effective diffusion barrier against chemical reaction leading to the formation of a brittle layer, a promising coating material should also minimize the local tensile residual thermal stresses in the composite especially at the interfacial region. In view of either preventing premature damage caused by residual thermal stresses in the composite, or load transfer mechanism provided by these stresses, the stress state in the reaction zone and the matrix as influenced by the thickness of the reaction zone and the mechanical properties of the fiber coating material have been investigated. Typical SiC fiber coating materials; Cu, Nb, Amorphous Carbon and TiB₂ with 50% porosity are employed here.

Fig. 4-5(a)-(f) show the variation of the radial, hoop and axial stress components induced in the matrix and the reaction zone during post fabrication cool-down with various thickness of the interfacial region for different fiber coating materials. The results do not reveal any general trend for the relationship between the thickness of the reaction zone, its mechanical properties and the thermal stress states in the constituents of the composite for all coating materials considered. The magnitude of the transverse (radial and hoop) stress components in the matrix decreases as the thickness of the interfacial region increases. While Cu-coating also decreases the axial thermal stress in the matrix, other coating materials considered cause an increase in the axial stress component with increasing thickness of the interfacial region. The radial stress component is compressive in the interfacial regions for all fiber coating materials considered. However TiB₂- and Cu-coating induce highly tensile hoop and axial stresses in the interfacial region. Since this region is usually brittle in nature and is sensitive to tensile loading, thus

reducing the magnitude of the tensile stress components in this layer is of prime importance. This tensile hoop stress is responsible for generating radial cracks in the composite. The result indicates that Cu-coating induces the highest tensile hoop and axial stress level in the reaction zone which would facilitate the nucleation and propagation of radial cracks in this layer. On the other hand, a small compressive hoop and axial stress components result from the use of C-coated fibers, which potentially increase the ability of the layer to resist cracking. From the load transfer point of view, both fiber coating materials, TiB_2 and Nb, are favorable because they induce high compressive radial stress components in the reaction zone and the matrix. The relative magnitudes of the CTEs and Young's moduli of the different coating materials considered, the SCS-6 fiber, and the Timetal 21S matrix are shown in Fig. 4-6(a)-(b). It is noted that C-coating with both CTE and Young modulus values much smaller than for the matrix generates lower level of residual thermal stress in the interfacial region. Although the radial stress component decreases substantially with increasing thickness of the interfacial layer, the thickness has small effect on other components of thermal stress in the layer (see Fig. 4-5(d)-(f)). The radial stress component which is beneficial based on the load transfer mechanism is preserved in the reaction zone and the matrix when employing fiber coating materials (Nb or TiB_2) with both CTE and Young's modulus values close to the values for the matrix.

Throughout consolidation, a compressive stress state is induced in the fiber because both the reaction zone and the matrix with higher CTEs but lower Young's moduli than the fiber shrink rapidly around the fiber.

The results of this study indicate that the selection of a suitable fiber coating material should be based on the application requirement of the composite.

4.2.3 Role of Creep Deformation in the Evolution of Thermal Stresses

During post-fabrication cool-down of the composite from consolidation temperature, the thermal stresses induced in the matrix may cause creep deformation at relatively high temperature. The deformation however, is constrained by the relative inextensibility of the elastic fiber and the reaction zone, and the bonding between each constituents of the composite. In the present study, the significant influence of time-dependent deformation behavior on the evolution of thermal stresses in MMCs during initial cool-down has been investigated. Fig. 4-7 shows the evolution of thermal stresses in the matrix throughout consolidation for purely elastic, elastic-plastic and elastic-plastic-creep cases. The elastic-plastic-creep calculations predicted that at high temperature following consolidation, the thermal stresses were relaxed extensively by creep. Consequently, no plasticity occurred in the composite since the effective stress level is always lower than the yield stress of the matrix throughout the initial cool-down. However, elastic-plastic calculations predicted that the matrix yielded at 720 °C and the stress is brought down to the yield value of the matrix. The final locked-in residual thermal stresses at room temperature are considerably lowered due to creep deformation.

The time-dependent characteristics have been studied through the effect of cooling rate during consolidation on the creep behavior and the residual thermal stress state of the composite. Several cooling rates ranging from 5×10^{-3} to 1.0 °C/sec are utilized in the model and the results are presented in terms of the reduction in effective stress accounted for creep effect in relation

to elastic case as shown in Fig. 4-8. The amount of reduction in the effective stress increases exponentially as the cooling rate is lowered. A stress reduction of 9.97% was calculated for cooling rate of 0.5 °C/sec while an additional 10.72% occurred for a slower cooling rate of 0.005 °C/sec. At a slower cooling rate, the composite is exposed to high temperature creep for a longer duration of time, which enhance the accumulation of creep strain resulting in extensive stress relaxation in the matrix. This result indicates that the final locked-in residual thermal stress can be tailored by controlling the cooling rate during consolidation of the composite.

For a particular cooling rate, the maximum reduction in thermal stress always occurs in the vicinity of the matrix/reaction zone interface where the elastic stress is maximum due to the largest difference in CTEs of adjacent layers. The magnitude of the stress relaxation in the matrix due to creep decreases non-linearly from 10% at the interface to 5.3% at the outer layer of the matrix. The results indicate that the matrix creep deformation has a significant effect on the evolution of the thermal stresses and the stress relaxation mechanism in MMCs.

4.2.4 Evolution of Thermal Stresses During Thermal Cycling

As discussed above, the time-dependent deformation plays a significant role in generating thermal stresses in MMCs. The determination of the key parameters which yield the correct stress state in the composite is of prime importance in the current mathematical modelling. During initial cool-down from consolidation temperature, the matrix experiences creep deformation which is governed by eq. (2) and (3). The matrix thermal activation energy, Q in eq. (3) can be treated as a constant for the evolution of thermal stresses in the matrix throughout this process, as indicated by a good agreement between the calculated and the experimental results, see Fig. 4-9. Previous experimental work by Ghonem and Zheng [15] showed that for loading conditions consisting of the initial cool-down followed by thermal cycling between 100 - 550 °C, the axial thermal stress in the matrix has been reduced to zero at the upper temperature level after the application of only five cycles, as shown in Fig. 4-10. This reduction in thermal stresses has been attributed to the influence of the creep deformation developed in the matrix material during thermal cycling. However, the attempt to predict the stress history during a loading process similar to that of [15] using the present model with Q being kept as a constant, has resulted in a stress cycle pattern with a negligible amount of stress reduction at the upper limit of the thermal cycle. The parameter Q , was then linked to the variation in temperature to obtain the best curve fitting to experimental data. The resulting Q was further correlated to the induced matrix stress and strain during the thermal cyclic process. This correlation could be expressed in terms of the inelastic strain energy density, W_{pc} , as:

$$Q = Q_0 - f(W_{pc}) \quad (6)$$

where Q_0 is the value of Q prior to thermal cycling and $f(W_{pc})$ is a monotonic increasing function of W_{pc} , in which W_{pc} is defined as:

$$W_{pc} = \int_{\bar{\epsilon}_0}^{\bar{\epsilon}''} \bar{\sigma} d\bar{\epsilon}^{cr} \quad (7)$$

$\bar{\sigma}$, $\bar{\epsilon}^c$ are the effective stress and the creep strain, respectively, and $\bar{\epsilon}_0^c$ is the initial creep strain.

This result indicates that the level of thermal activation energy, Q , in the matrix is affected by the simultaneous variation of stress, strain and temperature experienced by the composite throughout consolidation and thermal cycling. This observation, in fact, supports similar conclusion made by Ghonem and Zheng [16] in their experimental work on Alloy 718 at 650 °C and by Freed et al. [17], on the basis of thermodynamics analysis conducted on Copper and LiF-22mol percent CaF hypereutectic salt.

4.3 CONCLUSIONS

The model developed in the last section was employed in a parametric study using SCS-6/Timetal 21S composite system. The following conclusions are derived through the analysis of the results:

- 1- The geometry of the four-phase model requires that the radius of the surrounding composite media to be at least seven times larger than the radius of the matrix to ensure its role in providing realistic geometrical constraints through the surrounding fiber interactions with the model unit.
- 2- The residual thermal stress induced in the composite during consolidation can be reduced considerably by the creep deformation occurring in the matrix. A slow cooling rate allows longer duration of time for the composite to be exposed to high-temperature creep effects resulting in extensive stress relaxation. The matrix layer experiences significant creep effects at the matrix/reaction zone interface where the residual stress level is high.
- 3- Subjecting a composite system to reversing thermal cycles indicate that the matrix thermal activation energy, Q , should be correlated with the creep behavior through the level of accumulated creep strain in the matrix layer.
- 4- The properties and thickness of the reaction zone formed in MMCs influence the thermal stress behavior in the matrix layer. The effective residual stress decreases as the thickness of the reaction zone increases.
- 5- The choice of a fiber coating material that inhibit fiber/matrix reaction and reduce the residual thermal stress level in the composite, and a particular cooling rate following fabrication provide a potential mean of optimizing the mechanical performance of the composite system.

4.4 REFERENCES

1. Tamin, M. N., Zheng, D. and Ghonem, H., 1993. J. Composite Materials.

2. Schwenker, S. W., Evans, D. J. and Eylon, D., 1992. Longitudinal Creep Behavior and Damage in SCS-6/Ti-6Al-4V Metal Matrix Composites, Seventh World Conference on Titanium, San Diego, CA.
3. Dicarlo, J. A., 1986. J. Material Science, 21:217-224.
4. Saigal, A., Kupperman, D. S. and Majumdar, S., 1992. Mat. Sc. Engng., :59-66.
5. Arnold, S. M. and Wilt, T. E., 1992. NASA TM 105438.
6. Arnold, S. M., Arya, V. K. and Melis, M. E., 1990. NASA TM103204.
7. Khobaib, M. and Ashbaugh, N., 1991. Unpublished work.
8. Martin, P.L., Bingel, W. H. and Mahoney, M.W., 1992. Titanium Matrix Components, Workshop Proceedings, ed. by Smith, P. R. and Revelos, W.C., WL-TR-92-4035, :277-291.
9. Lemaitre, J. and Chabache, L., 1990. Mechanics of Solids (English Translation), Cambridge University Press, NY.
10. Christensen, R. M. and Lo, K. H., 1979. J. The Mechanics and Physics of Solids, 27:315-330.
11. Underwood, E. E., 1969. Quantitative Stereology, Addison-Wesley, Reading, Man.
12. Sohi, M., Adams, J. and Mahapatra, R., 1991. Constitutive Laws of Engineering Materials, ed. by Desai, C. D., Krempl, E., Frantziskonis, G. and Saadatmanesh, H., ASME Press NY, :617-626
13. Buesking, K. W., Young, J. L. and Reynolds, G. H., 1992. Titanium Matrix Components, Workshop Proceedings, ed. by Smith, P. R. and Revelos, W. C., WL-TR-92-4035, :42-64.
14. Maruyama, G. Barrera, E. and Rabenberg, L., 1991. Characterization and Modification of Composite Interfaces, Metal Matrix Composites: Processing and Interfaces, ed. by Everett, R. K. and Arsenault, R. L., Academic Press, Inc., NY, :181-216.
15. Ghonem, H. and Zheng, D., 1993. Mat. Sc. Engng., (in press).
16. Ghonem, H. and Zheng, D., 1991. Fatigue & Fracture of Engineering Materials and Structures, 14:749-760.
17. Freed, A. D., Raj, S. V. and Walker, K. P., 1992. J. Engng. Mat. and Tech., 114:46-50.2

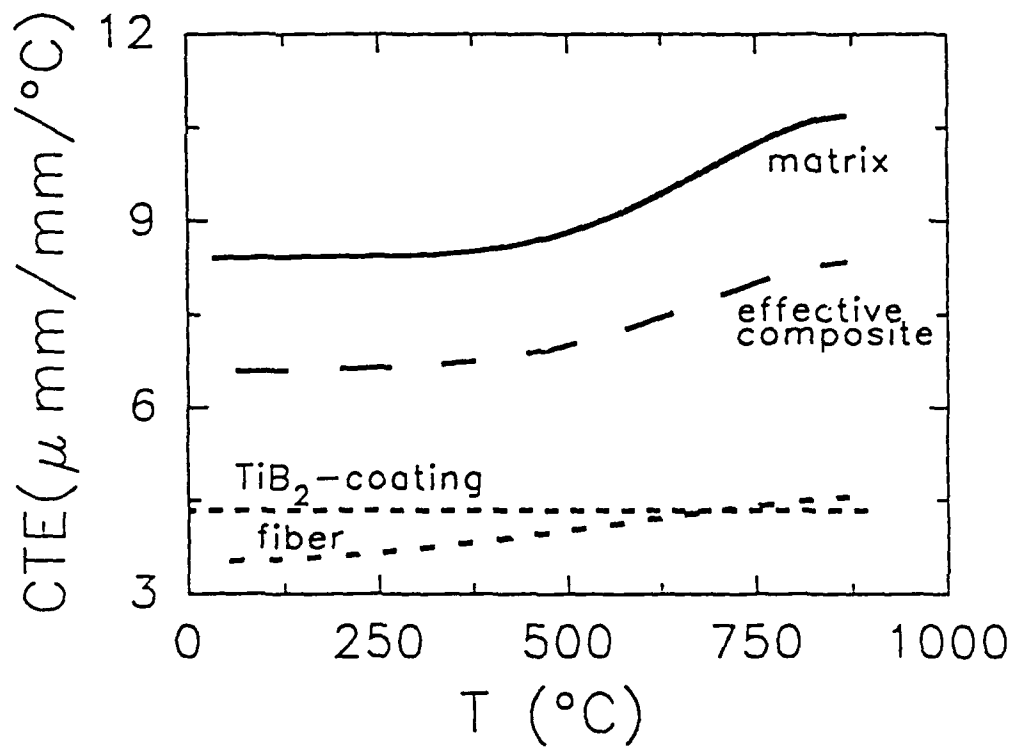


Fig. 4-1(a) Physical properties of the constituents: CTE.

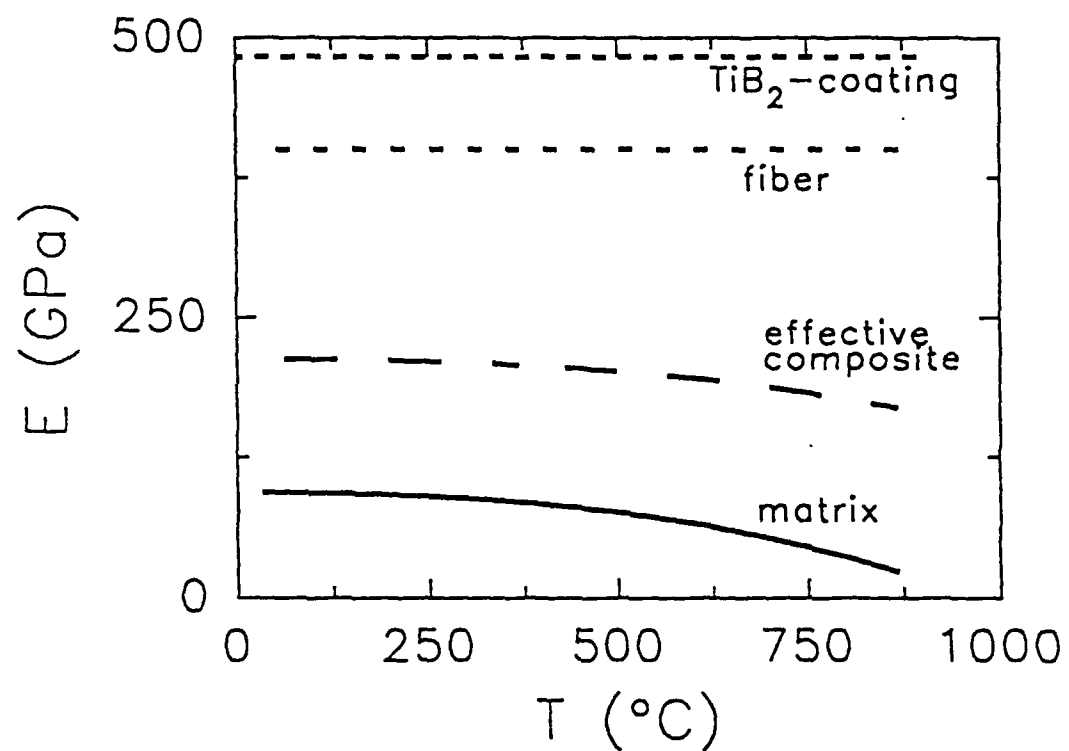


Fig. 4-1(b) Physical properties of the constituents: Young's modulus.

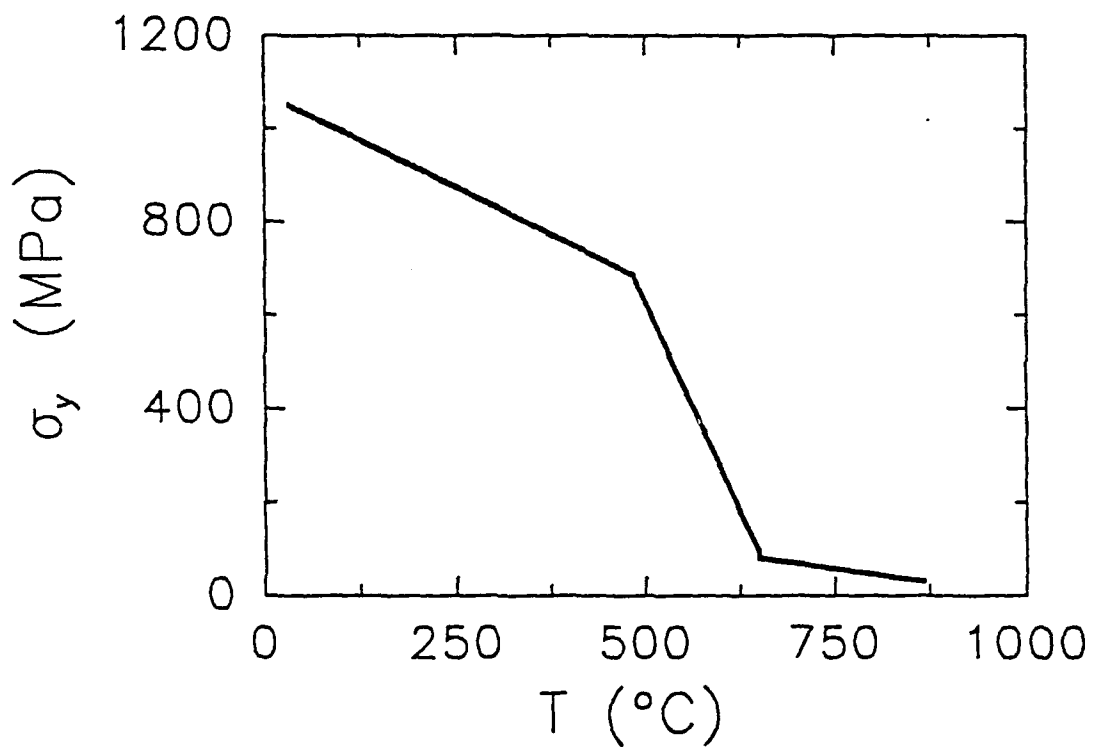


Fig. 4-1(c) Physical properties of the constituents: Yield strength of Timetal®21S.

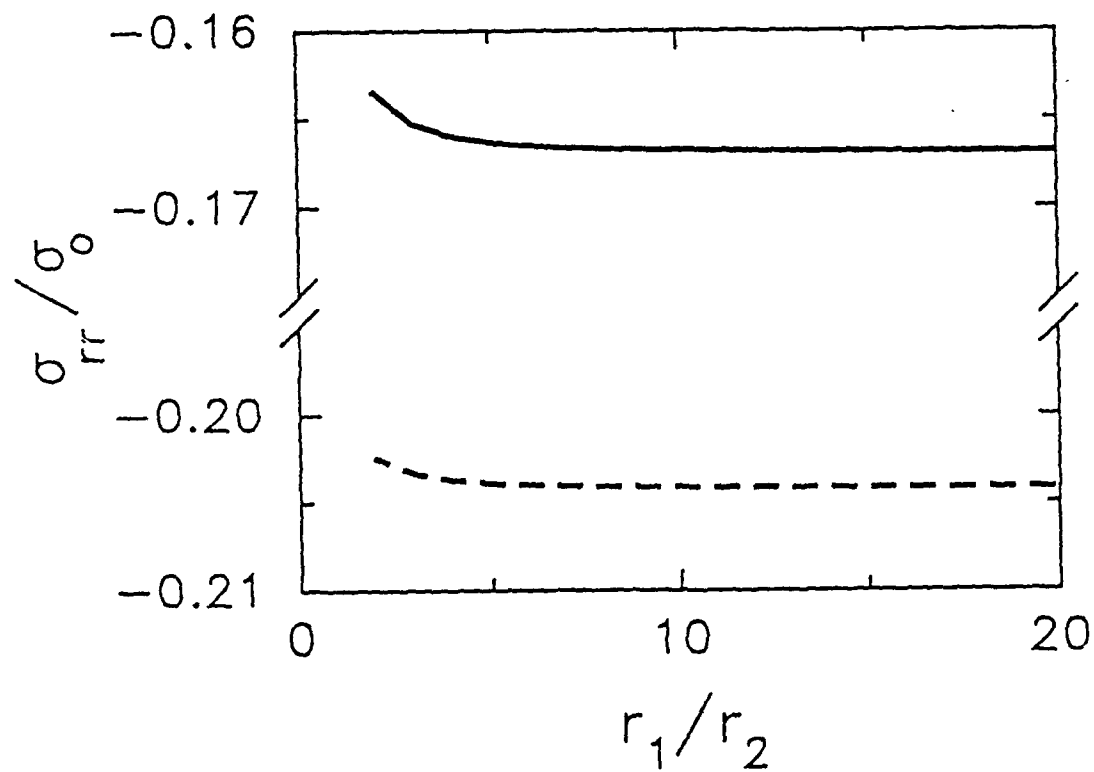


Fig. 4-2(a) Variation of stress field in the matrix layer with size of the equivalent composite: Radial Component. — $v_f = 35\%$, ---- $v_f = 20\%$.

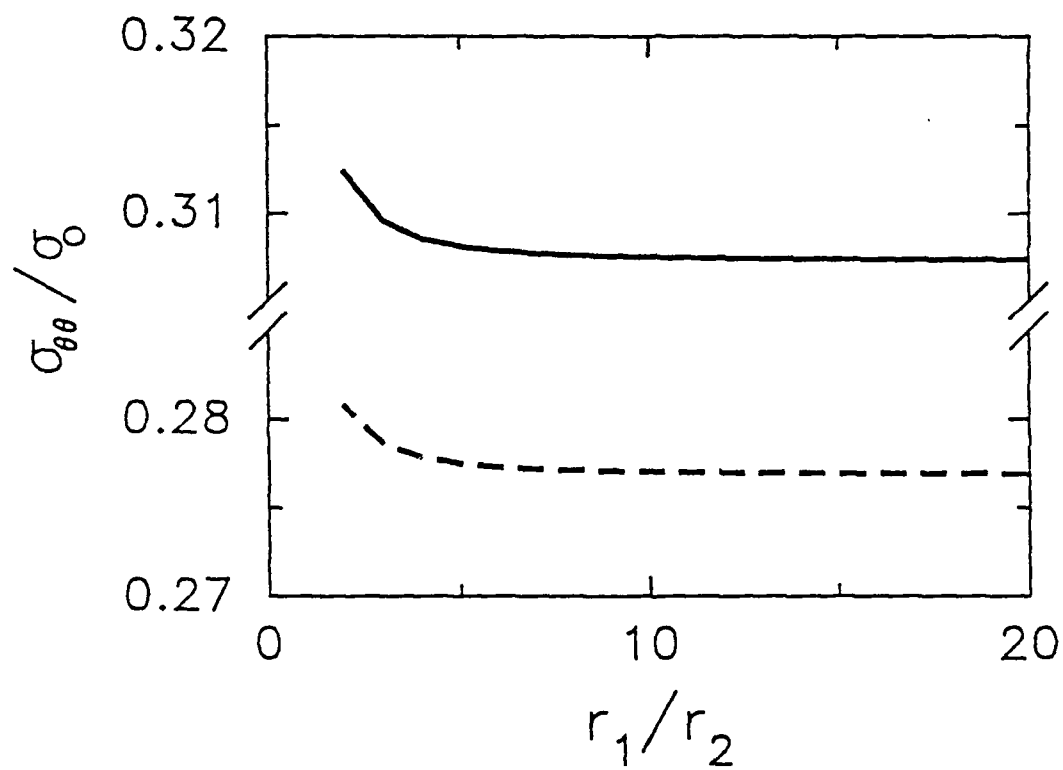


Fig. 4-2(b) Variation of stress field in the matrix layer with size of the equivalent composite: Hoop component. — $v_f = 35\%$, - - - $v_f = 20\%$.

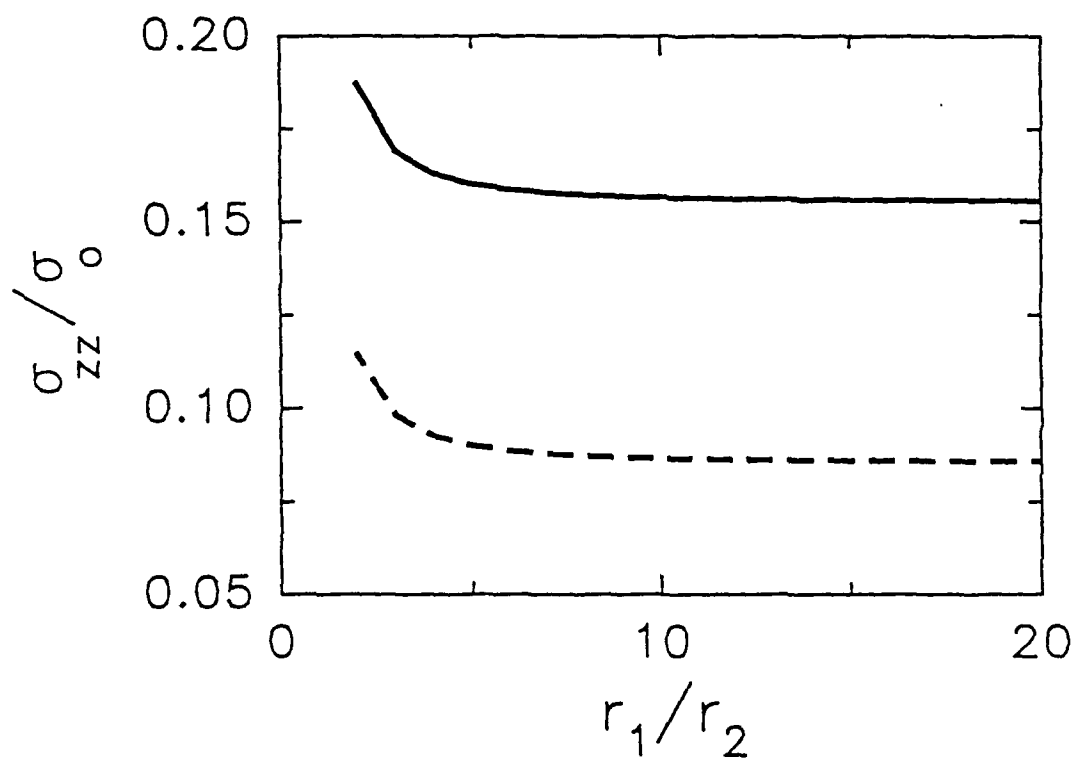


Fig. 4-2(c) Variation of stress field in the matrix layer with size of the equivalent composite: Axial component. — $v_f = 35\%$, - - - $v_f = 20\%$.

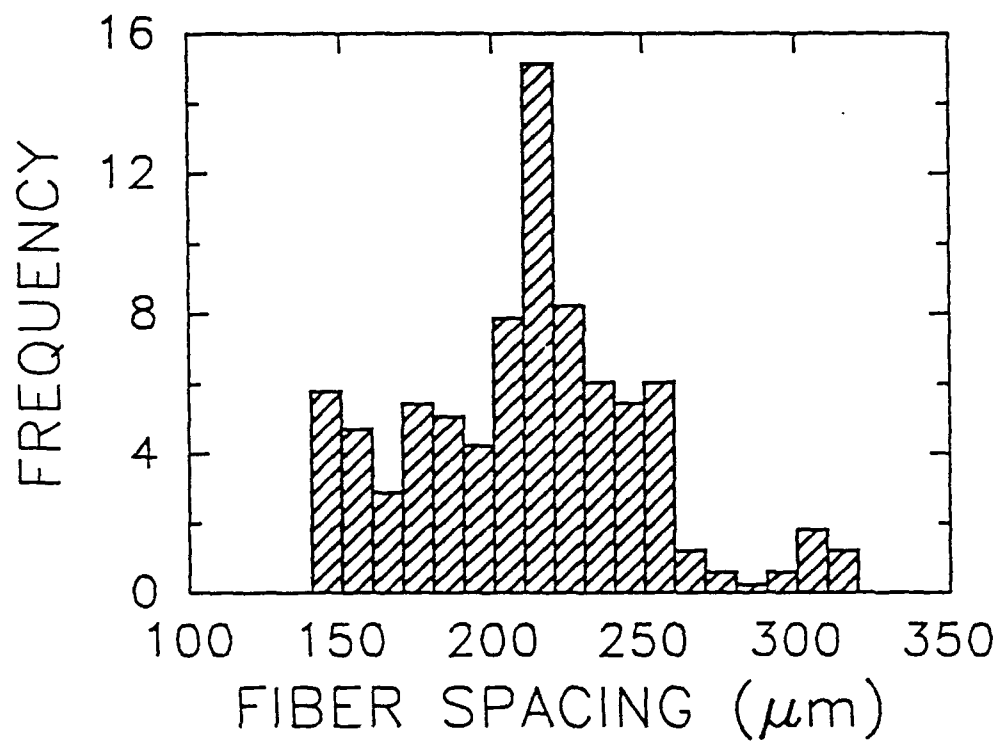


Fig. 4-3 Frequency distribution of center-to-center spacings between fibers in Ti-15-3 composite with 35% fiber volume fraction.

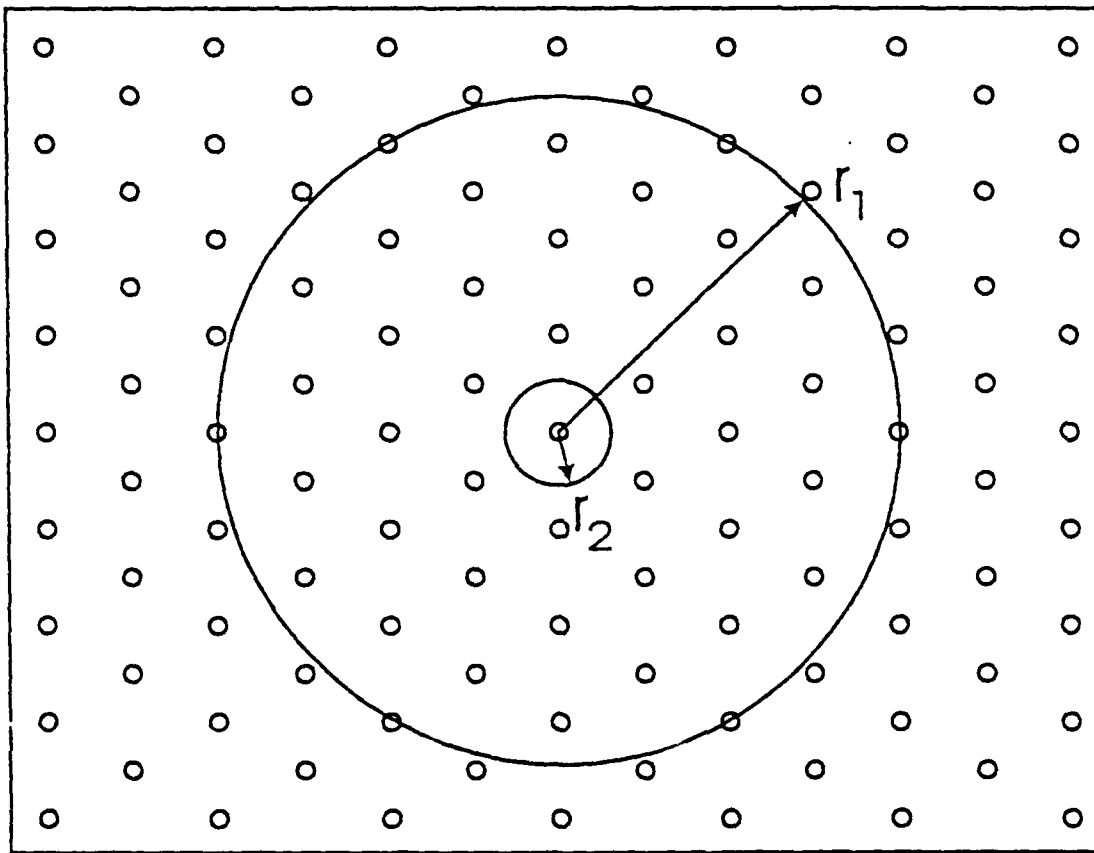


Fig. 4-4 Idealized array of fibers in MMC with 35 % fiber volume fraction.

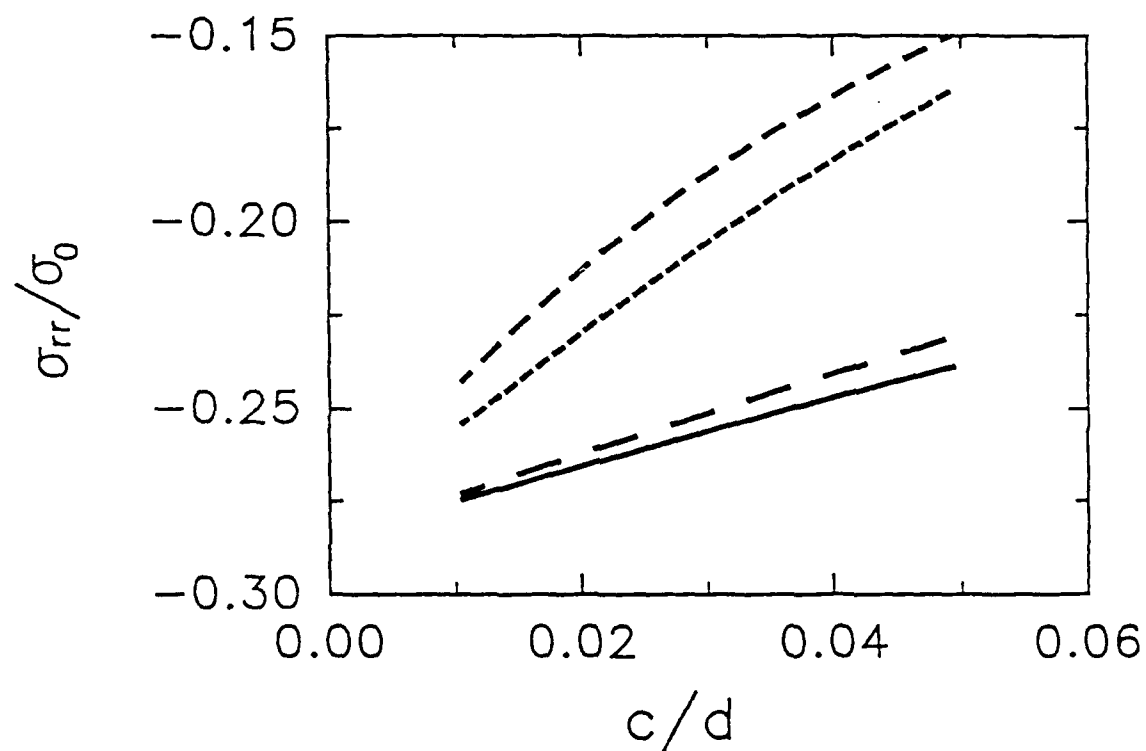


Fig. 4-5(a) Variation of radial stress field in the matrix with thickness of fiber coating for different coating materials: — TiB_2 , — — Nb , - - - C , . . . Cu .

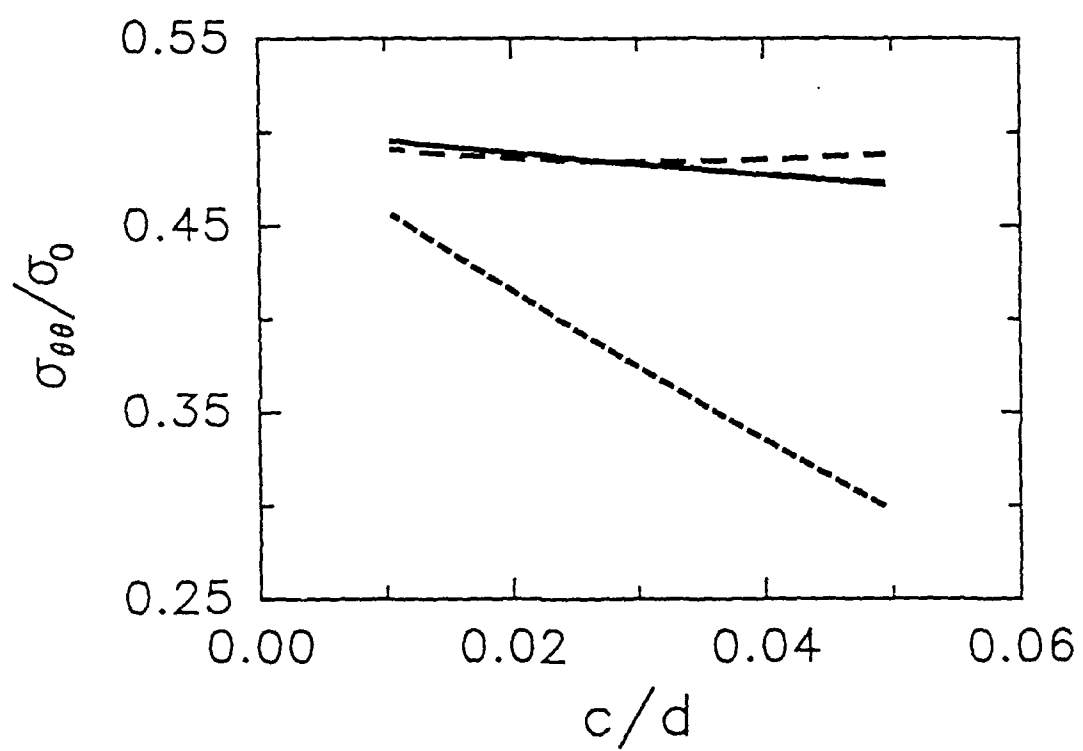


Fig. 4-5(b) Variation of hoop stress field in the matrix with thickness of fiber coating for different coating materials: — TiB₂, — — Nb, — — — C, — · — · — Cu.

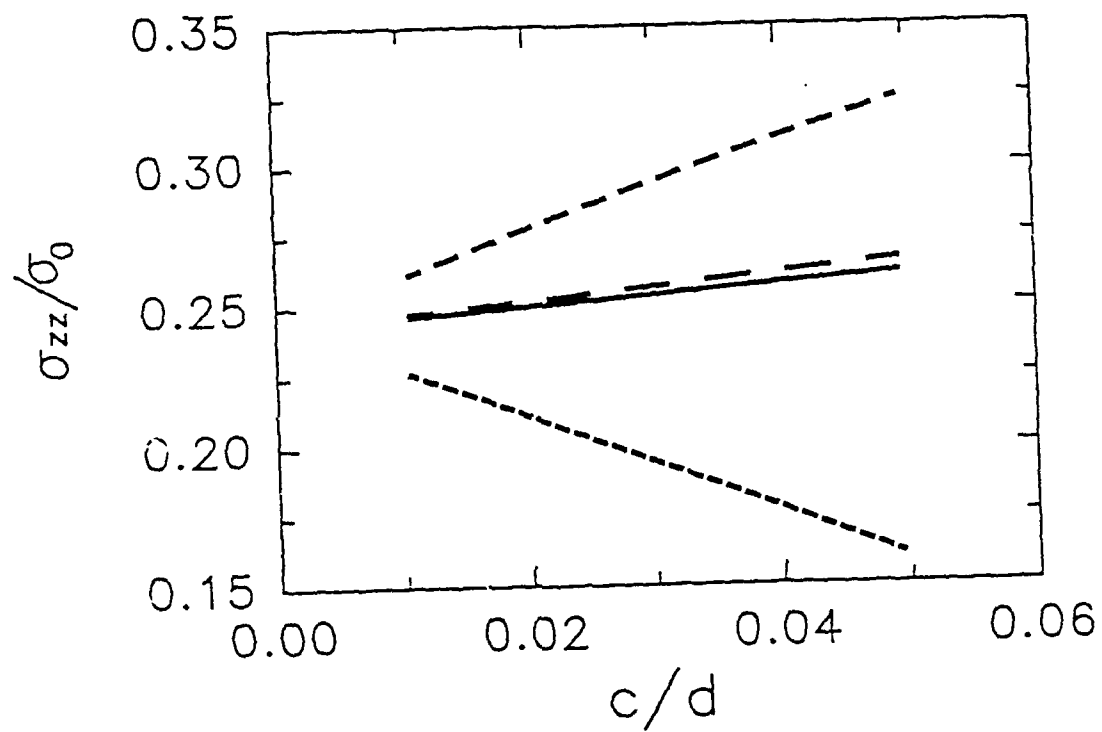


Fig. 4-5(c) Variation of axial stress field in the matrix with thickness of fiber coating for different coating materials: ——— TiB₂, — — — Nb, - - - - C, - . - . - Cu.

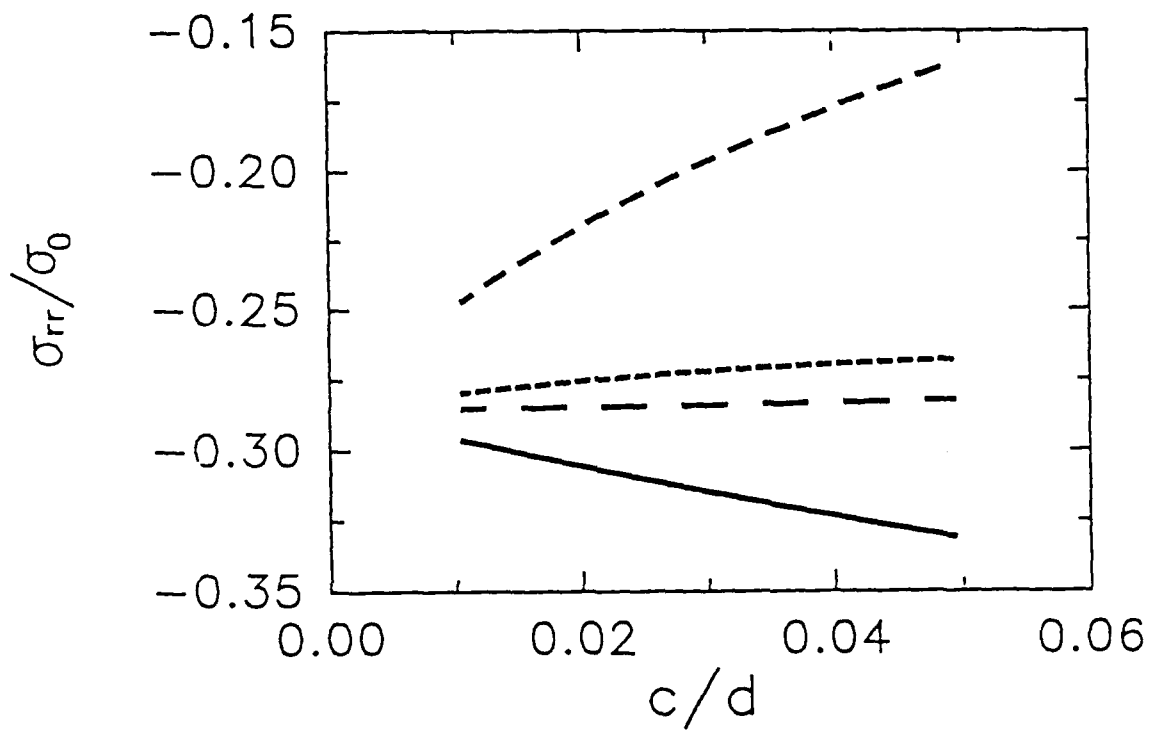


Fig. 4-5(d) Variation of radial stress field in the interfacial region with thickness of fiber coating for different coating materials: ——— TiB₂, — — — Nb, - - - - C, - . - . - Cu.

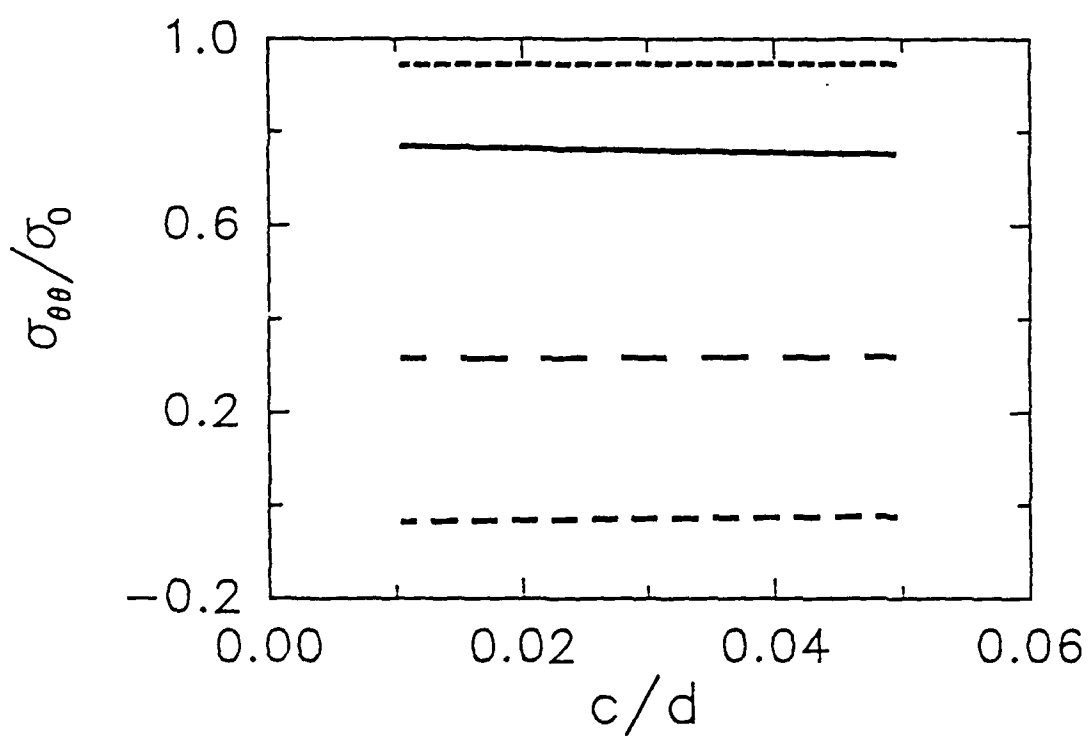


Fig. 4-5(e) Variation of hoop stress field in the interfacial region with thickness of fiber coating for different coating materials: ——— TiB_2 , ——— Nb, — — — C, - - - - Cu.

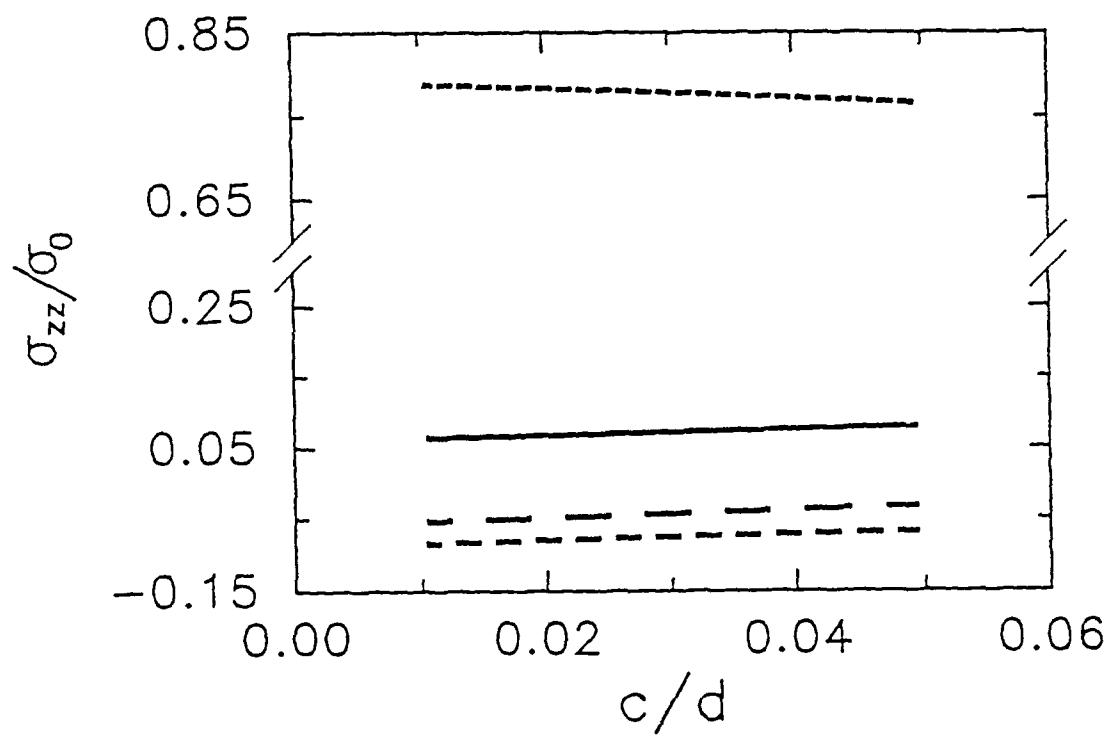


Fig. 4-5(f) Variation of axial stress field in the interfacial region with thickness of fiber coating for different coating materials: ——— TiB₂, ——— Nb, ——— C, ——— Cu.

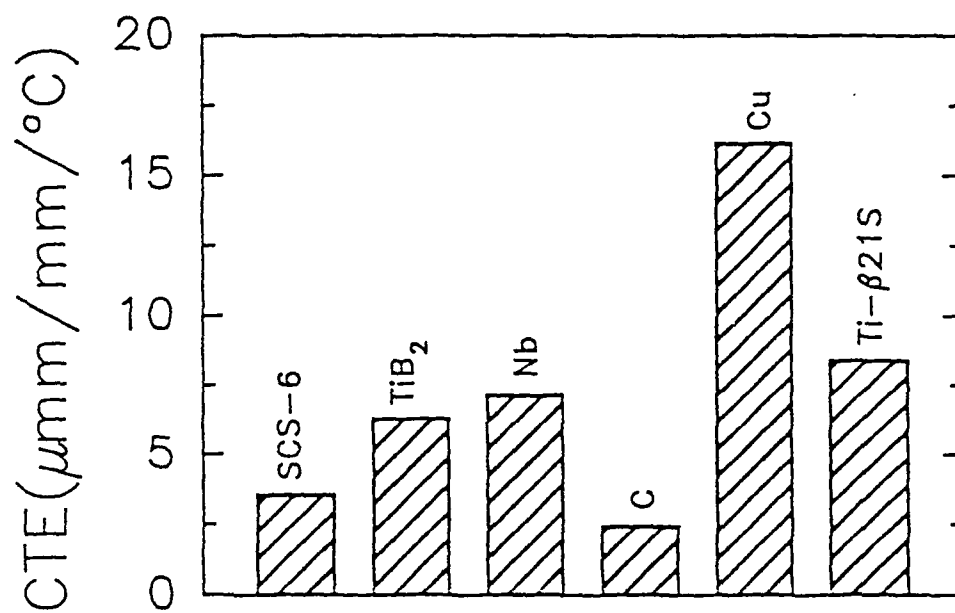


Fig. 4-6(a) Physical properties of the composite constituents at room temperature: CTE.

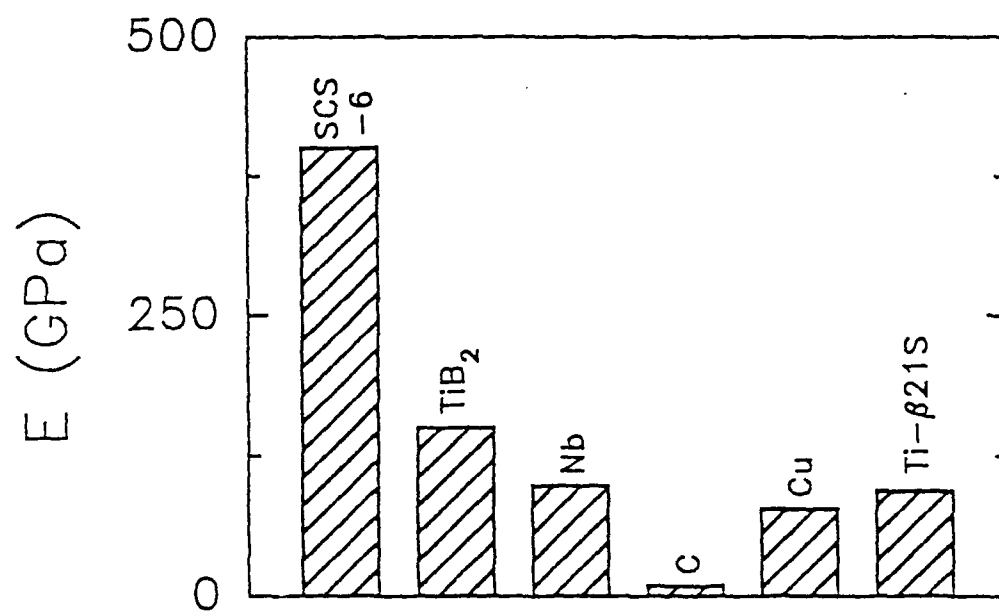


Fig. 4-6(b) Physical properties of the composite constituents at room temperature: Young's modulus.

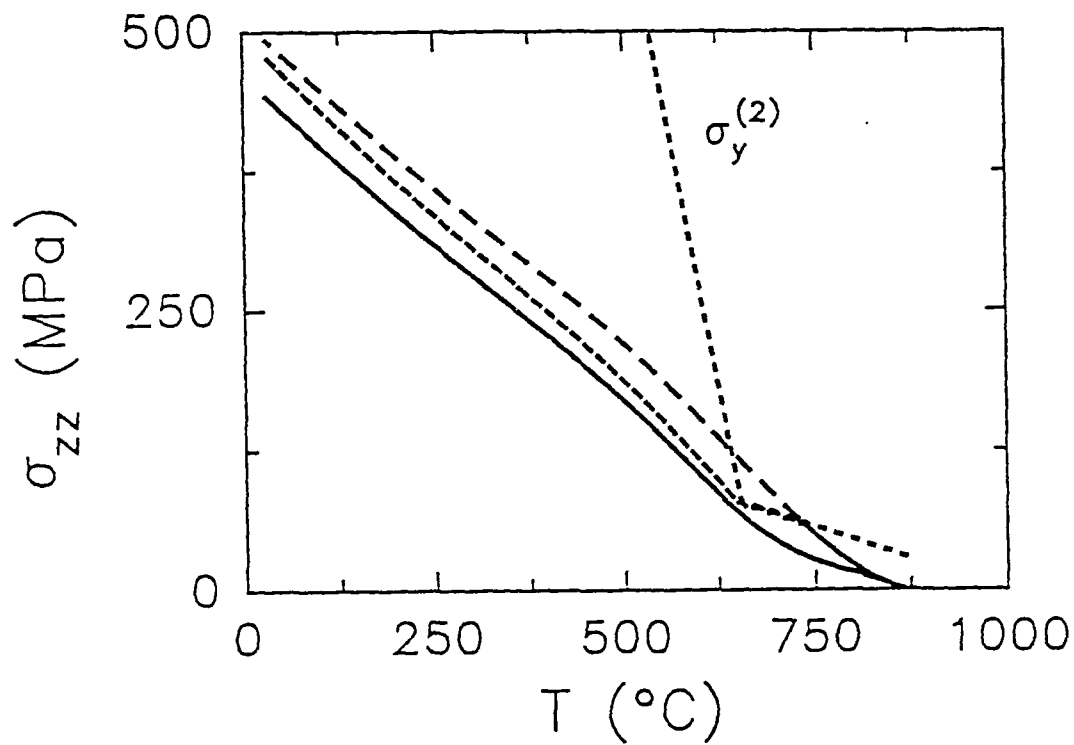


Fig. 4-7 Evolution of axial thermal stress in the matrix during initial cool-down at 0.5 °C/sec.: ——— elastic-plastic-creep, - - - - - elastic-plastic, — — — elastic. $\sigma_y^{(2)}$ is the matrix yield strength.

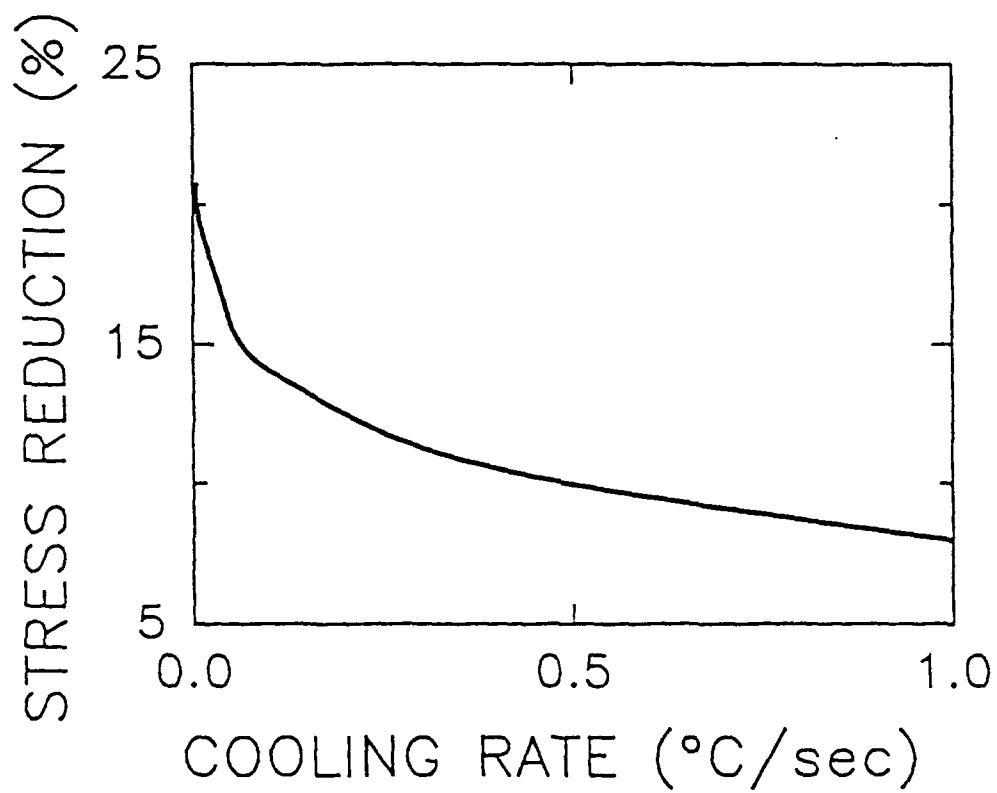


Fig. 4-8 Amount of stress reduction due to creep in the matrix at various cooling rates.

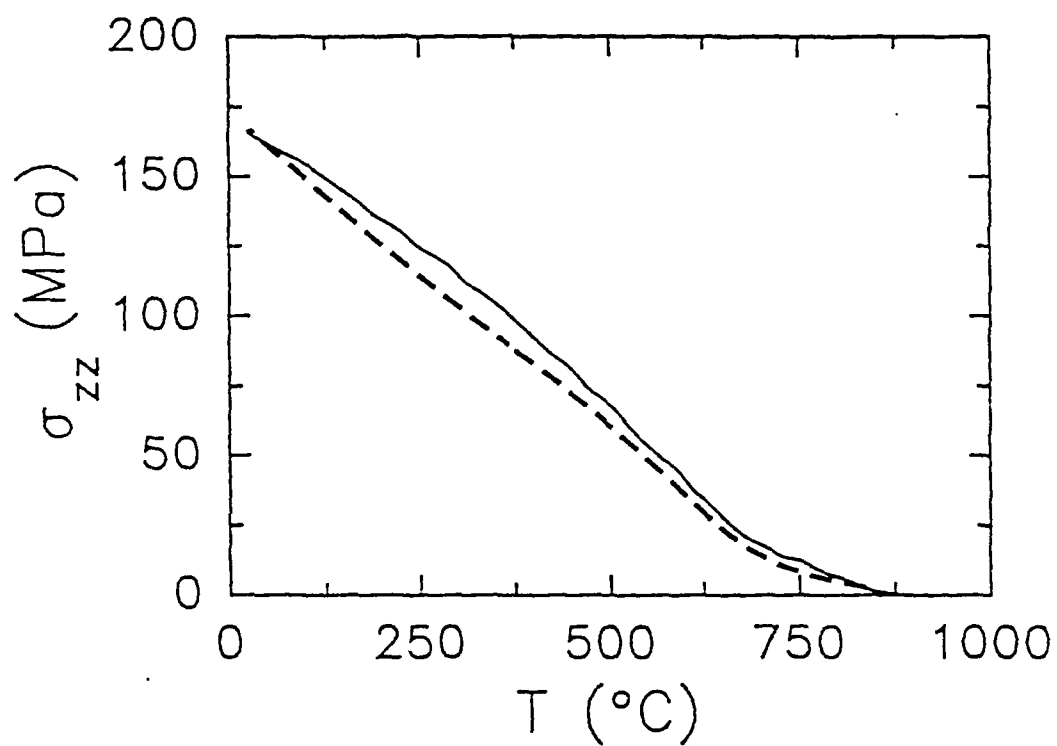


Fig. 4-9 Evolution of axial thermal stress during initial cool-down at 0.5 °C/sec.:
 ——— experiment [Ref. 15], - - - - present result.

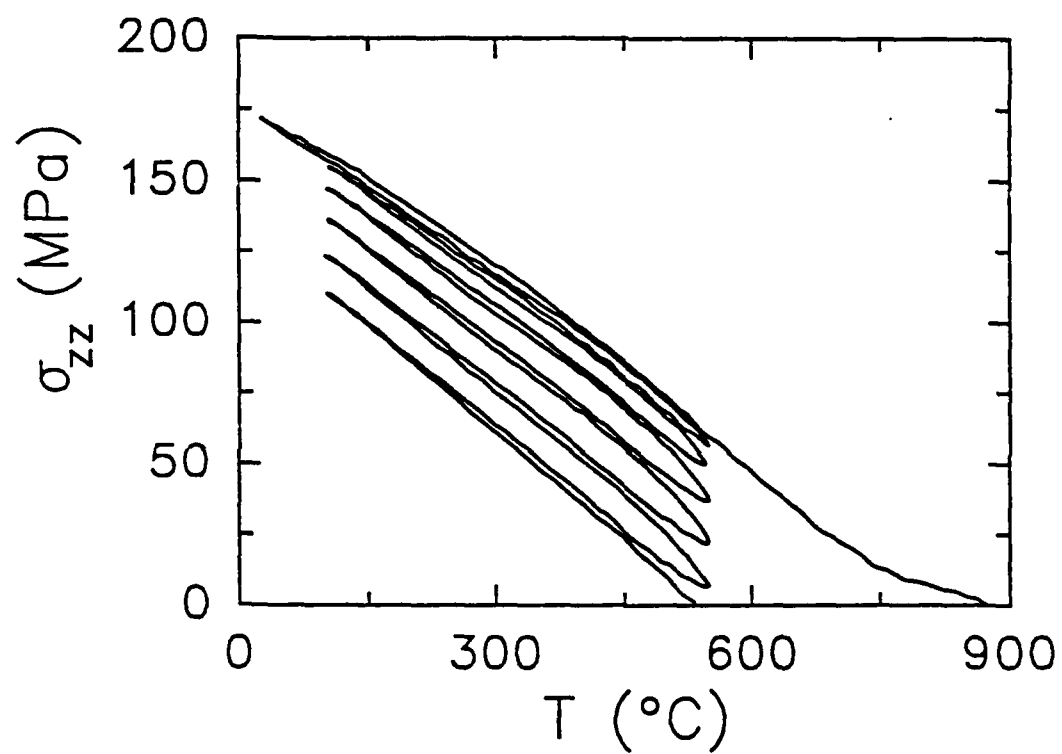


Fig. 4-10 Evolution of axial thermal stress in the matrix during initial cool-down and thermal cycle between 100 - 550 °C at 0.5 °C/sec.

SECTION 5

HIGH TEMPERATURE FATIGUE CRACK GROWTH OF THE CONTINUOUS FIBER REINFORCED TITANIUM METAL MATRIX COMPOSITE SIGMA/TIMETAL 21S⁵

ABSTRACT

A series of fatigue crack growth experiments were conducted on the continuous fiber reinforced σ 1240/Timetal 21S composite. In all tests, the cracking process concentrated along a single dominant crack. The principal damage mechanism of this composite under the load condition studied in this section was crack bridging and fiber/matrix debonding confined to regions near the crack surfaces. Furthermore, the crack growth in all tests consisted of a growth retardation stage followed by a growth acceleration stage leading to final failure. The increase in temperature was found to lead to a decrease in the crack growth rate which was also found to be inversely proportional to the loading frequency. Furthermore, an anomalous behavior depicting a decrease in the fatigue crack growth rate as the nominal applied stress intensity factor range, ΔK_{app} , increases was also observed. This behavior was explained by correlating the crack growth rate and the effective stress intensity factor range, ΔK_{eff} , which takes into account the shielding effect due to crack bridging.

5.1 INTRODUCTION

Titanium matrix composites with their unique combination of stiffness, strength and density at high temperatures are promising materials for advanced aerospace applications. The development of continuous fiber reinforced titanium composites is particularly critical for the use in high temperature structural components which are stressed in one dimension only. A key issue in the potential success of these materials is the understanding of their high temperature damage tolerance characteristics with respect to time-dependent related effects such as inelastic deformation and environment attack. Few studies have, however, been made in the area of high temperature damage evolution and in particular the high temperature fatigue crack growth behavior of continuous fiber-reinforced metal matrix composites. The current literature shows that the optimum combination of matrix toughness and interfacial strength is achieved when the crack bridging becomes the principal damage mechanism in the metal matrix composites [1-3]. The crack bridging was found to occur in titanium matrix composites under conditions of practical interest, and work based on ambient temperature showed that bridged fibers can provide shielding effects which decrease the crack tip driving force thus enhancing the resistance to crack

⁵ based on "High temperature fatigue crack growth of the continuous fiber reinforced titanium metal matrix composite Sigma/Timetal-21S", D. Zheng and H. Ghonem, submitted to Materials Science and Engineering, 1993.

propagation [2-5]. In this mechanism the crack growth rate is governed by a process in which the increase in the crack length is accompanied by an increase in the number of fibers bridging the crack. This would continue up to a "steady state" condition produced by the competition between creating more bridged fibers as the crack length increases and the fracture of these fibers as more stress is transferred to them by the increased crack-opening displacements. Here, however, it appears to be difficult to define the conditions at which stable/unstable crack growth transitions occurs [2]. Although the subject of the crack bridging is very important and attracts increasing attentions, the full understanding of related phenomena in metal matrix composites, such as failure mechanisms of bridged fibers, remain an open issue [1]. This situation is further complicated in cases involving elevated temperatures where fewer studies have been attempted. Bain et al worked on SCS-6/Ti-64 at 318 °C for frequencies of 20 Hz, 0.33 Hz and 0.033 Hz [6]. Their results showed that there was no considerable difference in the fatigue crack growth rates for 20 Hz and 0.33 Hz tests, while the fatigue crack growth rate for 0.033 Hz test increases by a factor of 40. This increase in the crack growth rate was attributed to environmental damage affecting the Ti-64 matrix material. However, they did not observe changes in the fracture surface features of specimens tested at different frequencies. No crack bridging was reported in their work, and for all their tests, the fatigue crack growth rate increases proportional to the crack length. Ibbotson et al studied the fatigue response of single edge notched (SEN) specimens made of SiC/Ti-6Al-4V composite. Tests were carried out in both ambient temperature and 550 °C for two loading frequencies; 10 Hz and 0.5 Hz [5]. They observed that in most cases the crack growth rates initially decreases with increasing crack length. The crack growth rates were, however, found to increase at 550 °C only at low frequency when compared with those obtained at ambient temperature. Here, none of these studies has identified the mechanisms governing the high temperature crack growth process in titanium metal matrix composites.

In order to fully understand the high temperature fatigue resistance phenomena of titanium composites, it is inevitable to explore the possible damage mechanisms related to the crack growth behavior of this kind of composites at elevated temperatures. Seeking this knowledge is the basic motivation behind the work performed in the present study which aims at investigating the high temperature crack growth behavior in relation to the influence of the crack bridging in σ 1240/Timetal 21S composite. In this section, the crack growth response to various temperatures and loading frequencies was described. Attempts were made, utilizing load conditions promoting the crack bridging, to identify the role of time dependent effects on the crack bridging and related failure mechanisms. The first part of the paper describes the composite material and the experimental procedure employed to carry out crack growth testings. This will be followed by detailed description of test results and discussion of their significance in relation to the damage process in this composite.

5.2 MATERIAL AND EXPERIMENTAL PROCEDURE

The material used in this study is the σ 1240/Timetal 21S composite. The matrix material is the metastable β titanium alloy (β 21S). The composition of this alloy (in wt%) is 0.1 Fe, 16.0 Mo, 3.06 Al, 2.9 Nb, 0.2 Si, 0.22 C, 0.12 O, 0.005 N with the balance being Ti [7]. The σ 1240 (SiC) fiber consists of tungsten-cored SiC monofilament with a dual vapor-deposited coatings of

carbon and boron-rich titanium diboride at the surface. The thickness of each of these layers is about 1 μm . The composite material is made of eight plies of β 21S foils with continuous σ 1240 fibers having approximately a 35% volume fraction and oriented along the 0° direction. The β 21S foil is 112 μm in thickness. The mechanical properties of the matrix material as well as those of the fiber are listed in Table 5.1.

Table 5.1 Mechanical Properties of the Fiber and the Matrix

T (°C)	E_m (GPa) [7]	ν_m [8]	$\sigma_{YS,m}$ (MPa) [7]	$\sigma_{UTS,m}$ (MPa) [7]	$\epsilon_{F,m}$ (%) [7]	E_f (GPa) [9]	ν_f [10]	$\sigma_{UTS,f}$ (Fiber) [9]	$\epsilon_{F,f}$ (%) [11]
24	98.2	0.35	1043	1089	>3.9	390	0.3	3340	1
500	72.4	0.35	552	641	>10.5	390	0.3	3340	1
650	47.6	0.35	245	289	50-55	390	0.3	3340	1

The composite was consolidated using vacuum hot pressing employing pre-established critical processing parameters. All consolidated composite plates, measuring 900 mm x 100 mm x 1 mm, had received a stabilization heat treatment (621 °C/8 hours) in a dynamic vacuum furnace. Fig. 5-1(a) is a chemically etched cross-section of the as-fabricated composite showing a hexagonal fiber arrangement and traces of the foil to foil interfaces. The average center-to-center fiber spacing is approximately 150 μm . Typical microstructure details of the fiber surrounding region is shown in Fig. 5-1(b). One observes that very fine α phase precipitated homogeneously within the grains and along the grain boundaries. Furthermore, the average grain size in the fiber surrounding region is about 12 μm which is smaller than that of the matrix material which measures about 50 μm . The distribution of finer grains is associated with the recrystallization during fabrication where large amount of viscoplastic flow exists near the fibers [11]. The high viscoplastic strain, which is necessary to form complete fiber/matrix bonding, produces high dislocation densities in areas surrounding fibers which in turn should provide sufficient driving force for recrystallization and the formation of smaller grain sizes in these areas [12-14].

The composite plates were machined into rectangular specimens measuring 75 mm x 4 mm with a center hole of 1.575 mm in diameter. All machining was accomplished using diamond cut-off wheels and diamond drills. In order to aid crack initiation, notches were cut at opposite horizontal edges of the center hole using a diamond-coated chromium wire having a diameter of 30 μm . To facilitate the use of the DC potential drop technique to measure variations in crack length during testing, four chromium wires were attached to each test specimen; two wires for measuring the reference voltage signal and the other two for measuring the change of voltage related to the change of crack length. The length of both cracks growing out of the machined notches was measured on both sides of the specimen using a travelling microscope. The optical observations were the primary means of crack length determination and were used to calibrate the DC potential drop signal for each test. The test specimen was heated using 8 quartz lamps

arranged in an open furnace configuration, allowing a ± 4 °C maximum temperature variations along the 60 mm specimen gage length. Testing temperature was measured by two thermocouples, each of which was placed on different ends of the specimen gage length and at a distance of 14 mm from the center hole. In addition to testing at room temperature, two other temperatures have been investigated, 500 °C and 650 °C. The temperature of 500 °C is the expected application temperature while 650 °C represents a near upper limit use of this type of Sigma fiber [14].

All specimens were gripped by a self-aligning hydraulic grip and tested using a servohydraulic material testing machine equipped with computer control and data acquisition capabilities. Tests were carried out in air environment under constant load range with the ratio of minimum to maximum load (R ratio) of 0.1. All specimens were subjected to precracking performed with loading frequency of 10 Hz while load range, R ratio and temperature were set equal to values intended for use in the actual test. Loads were applied parallel to 0° orientation of the fibers. The load levels were selected to produce an initial maximum stress in the range of 300 to 386 MPa. Stresses in this range were shown to produce crack bridging during the fatigue crack growth process in Ti-composites [3-5].

Three loading frequencies were examined in this test program: 10 Hz, 0.1 Hz and 0.02 Hz. The selection of these frequencies was based on results obtained from previous work on Timetal 21S fiberless laminates [7]. They showed that frequencies higher than 10 Hz produce insignificant oxidation damage at temperatures below 650 °C. Frequencies lower than 10 Hz, on the other hand, were shown to induce effects related to viscoplastic deformation and oxidation at temperatures up to 650 °C.

Several tests have been stopped before the specimen separation occurred in order to identify related fiber/matrix damage features. In each of these cases one of the specimen's surfaces parallel to the fiber direction was ground to a depth sufficient to uncover the near surface fiber array. This provided an opportunity to observe possible fibers bridging and the extent of fiber/matrix debonding in relation to the crack path.

The fracture surfaces of all specimens were subjected to scanning electron microscopy in order to identify the features of the fracture mechanisms and the changes taking place in the fiber/matrix interface region.

5.3 RESULTS

In all the tests carried out here, the fatigue fracture process was seen to advance along mainly a single dominant crack perpendicular to both the 0° fiber orientation and the direction of the applied load. The dominant damage mechanism associated with this single crack was observed to be crack bridging, an example of which is shown in Fig. 5-2. Furthermore, the degree of debonding of the fiber/matrix interfaces along the bridged fibers was limited to the vicinity of the crack surface which indicates a medium interfacial bond strength [14]. An advantage of the confinement of the fracture process to a single propagating crack is that the crack tip related damage could be described in terms of the crack growth rate. For this purpose, the curve of crack length versus cycle number for each of the tests was first constructed, see Fig. 5-3. The slopes of these curves which represent the crack growth rates were in turn plotted versus the

crack length. These results are compared in Fig. 5-4(a) for the loading frequency of 10 Hz with different temperatures and in Fig. 5-4(b) for the temperature of 650 °C with different loading frequencies.

Results in Figs. 5-4(a) and 5-4(b) indicate that in all test conditions the fatigue crack growth process exhibits two distinctive sequential stages. The first of these stages is a pattern of continuously decreasing crack growth rate as the crack length increases. The crack length corresponding to this crack growth retardation stage, as well as its cycle number, was observed to vary between tests. Therefore, contrary to results obtained by Bowen et al [2], the crack growth resistance in this Ti composite seemed not to be controlled by the number of fibers bridging the crack. The end of the crack growth retardation stage in each test is marked by the attainment of the minimum crack growth rate pertaining to the particular test condition. This minimum rate ranges from 5.6×10^{-6} mm/cycle in the case of 24 °C/10 Hz to 2.4×10^{-7} mm/cycle in the case of 500 °C/10 Hz. The crack growth retardation stage is followed by a stage which consists of either a single event of crack growth acceleration leading to crack instability and final failure as in the 500 °C/10 Hz test condition or consists, as in the test conditions of 650 °C/10 Hz and 500 °C/0.1 Hz, of repeated events of crack growth acceleration and retardation followed, again, by crack instability and final failure. This type of two-stage crack growth pattern has also been observed in the work of Ibbotson et al in the study of SCS6/Ti-6Al-4V composite at both ambient temperature and 550 °C [5] and in the work of Walls et al carried out on SCS-6/Ti-15-3 composite at room temperature. In no test carried out here, however, was complete crack arrest observed.

The importance of each of these two crack growth stages described above was determined on the basis of the ratio of the number of cycles corresponding to the crack growth retardation stage to the number of cycles to failure. In each of the test, this ratio was found to be greater than 50% of the total lifetime of the corresponding test specimen, which indicates that the crack growth retardation stage dominates the overall damage evolution process and plays a vital role in understanding and modelling the crack growth behavior of this composite when subjected to the range of load conditions utilized here.

The different fracture processes encountered in each of these crack growth stages are also evident in the appearance of the fracture surface features. For example, Fig. 5-5 which belongs to the 500 °C/10 Hz test condition, shows two different fracture zones, the first is for crack growth retardation stage and the second for the crack growth acceleration stage. The first zone has an excessive fiber core damage, see Fig. 5-6, which may have resulted from the application of large number of fatigue cycles and prolonged thermal exposure. The pullout fibers in this zone are relatively short. The second zone shows no fiber core damage and displays longer fiber pullout length. An example of the instable fracture zone is shown in Fig. 5-7, it has a high degree of matrix deformation surrounding the pullout fibers.

The extent of fiber slip during the fracture process was determined by measuring the length of pulled out fibers at mating positions along the fracture surfaces belonging to the same test specimen. The distribution of these lengths for different test conditions are shown in Fig. 5-8. The average fiber pullout length is seen to be proportional to the crack growth rate, the longest being achieved in the instable crack growth region. Furthermore, the dotted curves in Fig. 5-8 are the regression fittings of the pull out lengths corresponding to the crack growth retardation stage. Table 5.2 lists the approximate fiber pullout length near the notch tip. This table shows

that, in general, under the same applied stress range and R ratio, the increase in temperature or decrease in frequency results in the increase of the fiber pullout length.

The influence of temperature on crack growth rate for the loading frequency of 10 Hz is shown in Fig. 5-4(a). In these tests, the crack growth rate for the same crack length, decreases as the temperature increases. The increase in temperature from 500 °C to 650 °C does not bring variations in the crack growth rate within the crack growth retardation stage, but does cause an earlier transition to the crack growth acceleration stage.

The crack growth mechanism in the matrix for 10 Hz frequency tests was found to be transgranular. Typical example of the fracture surface features associated with this mechanism are shown in Fig. 5-9(a). They consist of cleavage facets; the size of which seems to depend on their location on the fracture surface and the corresponding crack growth rate; the higher the growth rate is, the larger the cleavage facet size is. Furthermore, foil to foil interfaces along the fracture surface are difficult to identify and did not interrupt the continuity of the cleavage planes. Isolated colonies of fatigue striations were found on fracture surfaces of some of these tests but did not represent a dominate fracture mode in any of the test cases.

Table 5.2 Variations of τ and h_T with Temperatures and Frequencies

Temp. (°C)	Frequency (Hz)	Frictional Shear Stress (τ) (MPa)	Fiber Pullout Length near Notch Tip (h_T) (μm)
24	10	48	86
500	10	78	148
650	10	84	110
650	0.1	99	117
650	0.02	103	152

The influence of the loading frequency on the fatigue crack growth rate at 650 °C is evident in the relative positions of the crack growth rate curves shown in Fig. 5-4(b). It is apparent that the decrease in frequency leads to an increase in the crack growth rate. The important factor in this behavior could be linked, similar to monolithic Ti alloys, to the increased role of time dependent parameters as the cycle duration increases. The contribution of these parameters to the damage process is manifested in the degree of plastic deformation observed on the fracture surfaces of the low frequency tests and the change in their matrix fracture mechanism into a mixed transgranular/intergranular mode as shown in Fig. 5-9(b). The sharpness of the grain boundaries observed in the case of the 0.02 Hz may indicate increase tendency towards brittle matrix fracture. Time dependent effects are also evident in the degree of oxidation damage incurred in the fiber coating layers and the existence of radial cracks, see Fig. 5-10. These kind

of cracks are not observed in the 24 °C test condition.

5.4 DISCUSSION

As mentioned in the previous section, the principal fracture mechanism in the composite under study is the growth of a single dominated crack accompanied with the crack bridging. The confinement of the fiber/matrix interface debonding to the vicinity of the crack surfaces indicates existence of matrix to fiber load transfer via interface bonds having medium interfacial strength [14]. In the crack bridging mechanism, the effective crack tip driving force is determined by the balance established between the influence of the externally applied load and that of tractions in bridged fibers which attempt to close the crack opening. The continuous transfer of load from matrix to bridged fibers could alter this balance thus causing conditions of crack growth retardation similar to that observed in the crack growth retardation stage described previously. The delayed fracture of the fibers within the bridged crack length could result in an apparent crack arrest. Ultimately, however, the fracture of any of these fibers could occur if the stress in the fiber reaches its ultimate strength. In this case the fiber fails at a plane coinciding with that of the maximum stress position in the fiber. The failure of bridged fibers could diminish the crack tip shielding force thus leading to a crack acceleration in the manner observed in the crack growth acceleration stage described above.

Aspects of the crack bridging and the failure of the bridged fibers are strongly influenced by time dependent effects associated with elevated temperatures and low frequency loadings. During the crack growth retardation stage, for example, the crack growth rate in the 500 °C/10 Hz test was always lower than that in the 24 °C/10 Hz test. The mechanism responsible for this outcome would involve initial stress relaxation occurring in the matrix material in response to the high temperature induced viscoplastic deformation. This matrix stress relaxation, in order to maintain a state of stress equilibrium in the composite, is accompanied by an increase in the stress being transferred to the bridged fibers. It should be pointed out that the microstructure of the matrix material surrounding the fibers, being a less resistive to creep due to its smaller grain size, would enhance the process of matrix stress relaxation. Another important element in this mechanism deals with the high shear strain existing in the tip of the fiber/matrix debonded interface region [15]. In order to accommodate this strain, one of two events could occur: (a) large stress will be generated in the fiber which if exceeds the fiber ultimate strength could cause its failure [15]; (b) large shear stress induced by the isostrain requirement in the bonded interfacial region ahead of the debonded zone [16,17]. In this case debonding could take place if this shear stress exceeds the shear strength of the interface. The debonding process would ensue readily in this composite due to the nature of the medium interfacial bond strength and the further decrease in the interfacial strength due to the high temperature effect. However, as the length of the debonded zone increases, the magnitude of the strain required to be accommodated becomes large thus leading to an increase in the fiber stress which could reach the level to cause fiber failure. The observation that the average fiber pullout length in high temperature tests is longer than that for 24 °C test could be viewed as a support of this argument (see Fig. 5-8). The elements of this mechanism, occurring separately or simultaneously, would mean that for the same crack length, the bridged fibers at high temperature carry higher loads thus producing

higher degree of crack tip shielding effect.

While the crack growth trend in the crack growth retardation stage for the 650 °C/10 Hz test is identical to that of the 500 °C/10 Hz test, indicating similarity in the matrix viscoplastic behavior at both temperatures, the transition to the crack growth acceleration stage occurs earlier in the 650 °C test. The increased influence of the environmental attack at this latter temperature could cause earlier failure of the bridged fibers through these oxidation of their exposed surfaces. This would reduce the shielding effect and prompt an acceleration in the fatigue crack growth. It should be noticed here that while the average fiber pullout length in the 650 °C/10 Hz test is shorter than the average length in the 500 °C/10 Hz test, it is still longer than that of the 24 °C test.

The last point to be discussed here is the use of the nominal applied stress intensity factor range, ΔK_{app} , to describe the crack growth behavior of composites exhibiting the crack bridging mechanisms. The difficulty in this subject stems from the fact that, as mentioned earlier, the existence of crack tip shielding limits the ability of ΔK_{app} to be viewed as a unique crack tip driving force [1,4,18,19]. The knowledge of the fatigue crack growth rate, da/dN , dependency on ΔK_{app} is, however, important in attempts to identify the extent of crack tip shielding and in providing basis for estimating the effective crack tip driving force. For this purpose the relationship between da/dN versus ΔK_{app} , the latter being calculated for center hole geometry, was obtained and, again, compared separately with respect to the influence of the temperature and the loading frequency in Figs. 5-12(a) and 5-12(b), respectively. One observes in these figures that during the crack growth retardation stage, the crack growth rate decreases as ΔK_{app} increases. This anomalous behavior is understood in terms of the assumption that ΔK_{app} consists of two components: a component representing the stress intensity factor range experienced by the crack tip, ΔK_{eff} , and a component related to the effect of crack tip shielding generated by bridged fibers, ΔK_{sh} . The relationship between these components can be expressed as [20-22]:

$$\Delta K_{eff} = \Delta K_{app} - \Delta K_{sh} \quad (8)$$

Considering ΔK_{eff} to be the actual crack tip driving force, an attempt was made to further examine the pattern observed in Figs. 5-4(a) and 5-4(b) by correlating ΔK_{eff} directly with the fatigue crack growth rate, da/dN . This attempt is carried out for all tests with the focus on the crack growth retardation stage only. The work of Zheng and Ghonem [23], has shown that the two input requirements for estimating ΔK_{eff} are the maximum bridging traction, p_{max} , and the sliding frictional stresses, τ , at the fiber/matrix interface. Following the work of Takakn and Arridge [24] and Watson and Clyne [25,26], p_{max} could be expressed by the following linear relationship:

$$p_{max} = \alpha h \quad (9)$$

where h is the fiber pullout length. The distributions of h for different test conditions are shown in Fig. 5-8. α is a proportional factor that varies with temperature, T , as follows:

$$\alpha(T) = 17.55 + 4.074 \times 10^{-7} \sqrt[3]{T} \exp(2.72 \sqrt[4]{T}) \quad (10)$$

The sliding frictional stress τ was obtained by interpolating the shear stress values listed in the work of Marshal et al [10] which was carried out on a composite similar to the one used

in the present study. Table 5.2 lists the interpolated values of τ for the temperatures 24 °C, 500°C and 650 °C. The variations in τ for different loading frequencies are calculated with the assumption that the initial crack increment measured from the notch tip is smaller than the average distance between fibers. At this position ΔK_{eff} would be taken equal to ΔK_{app} . Here, one should notice that the τ value increases as either the temperature increases or the loading frequency decreases. The proportional increase in τ with temperature has been reported by several authors, see for example Refs. [10,25]. The mechanisms responsible for this increase in τ while is not clear yet, it is believed to be related to the formation of interfacial oxide products which presumably have higher volume ratio. These oxides would induce large local compressive radial stress across the interfacial region, thus causing an increase in the frictional shear stress [27-29]. The change in τ with the loading frequency (or time) has not been discussed in current literature [30]. It is the authors' suggestion, however, that the relationship between τ and frequency should be similar to that of the τ with the test temperature since longer cycle duration at high temperature would favor the occurrence of interfacial reaction and the formation of oxide products. The existence of radial cracks in cases of low frequency tests, see Fig. 5-10, could be viewed as an evidence of high tensile hoop stress and high compressive radial stress being developed in the interfacial region [31].

Having identified p_{max} and τ , the following expression was employed to determine ΔK_{eff} [23]:

$$\Delta K_{\text{eff}} = \frac{p_{\text{max}}^2(x)}{\beta \left\{ a \left[1 - (x/a)^2 \right] \right\}^{\frac{1}{2}}} \quad (11)$$

where x is the position along the half crack length, a . The coefficient β is defined as

$$\beta = \frac{4\tau}{R_f \sqrt{\pi F}} \left(\frac{V_f}{V_m} \right)^2 \frac{E_f E_c(T)}{E_m^2(T)} \quad (12)$$

where E_c , E_m and E_f are the Young's moduli of the composite, the matrix and the fiber, respectively, E_c and E_m are temperature-dependent, V_f and V_m are fiber and matrix volume fractions, respectively, R_f is the fiber radius and F is a geometrical factor [32]. The calculated values of ΔK_{eff} were plotted in Fig. 5-12(c) against the crack growth rates for each of the test conditions carried out here. It is clear from this figure that da/dN increases proportional to ΔK_{eff} , and for the same ΔK_{eff} , da/dN increases as the temperature increases or the loading frequency decreases. These features are similar to those of the crack growth behavior when correlated with ΔK_{app} in high strength monolithic metallic alloys. In this sense, one could consider that ΔK_{eff} represents properly the crack growth driving force of this composite, particularly in the crack growth retardation stage. The correlation of da/dN with ΔK_{eff} can reveal in fact, certain interesting features of crack growth mechanisms in the composite under study. In Fig. 5-12(c), the slopes of the crack growth curves for 10 Hz tests are shown to decrease as the temperature increases. This decrease in slope indicates an increase in the viscoplastic deformation of the composite's matrix. The decrease in the frequency from 0.1 Hz to 0.02 Hz does not change the slopes of these two curves, which means the viscoplastic characteristics in these two cases are similar. The variation in values of da/dN in the 0.1 Hz and 0.01 Hz tests reflect, however, the

severity of the oxidation damage associated with the lower frequency test condition.

Furthermore, the influence of fiber reinforcement on the crack growth behavior was identified by comparing the da/dN vs ΔK curves of Timetal 21S laminate material (33) and those of the 10 Hz loading frequency shown in Figs. 5-4(a) and 5-4(b). This comparison is illustrated in Fig. 5-13. Here, the crack growth driving force for the laminate material is ΔK_{app} while for the composite is ΔK_{eff} . It is interesting to observe that the slopes of the composite crack growth curves are larger than their counterparts of the laminate material and the crack growth rates of the composite are considerably reduced as compared with those of the laminate material. These two modifications in the crack growth behavior of the composite show that the fiber reinforcements can significantly reduce the effects of both the viscoplastic deformation and the oxidation degradation of the composite's matrix.

5.5 CONCLUSIONS

A series of fatigue crack growth experiments were conducted on specimens made of the continuous fiber reinforced $\sigma 1240$ /Timetal 21S composite employing a combination of temperatures and loading frequencies. Major conclusions of this study can be summarized as follows:

1. Under loading conditions promoting the crack bridging, the fatigue crack growth process exhibits two consecutive stages: a crack growth retardation stage where the crack growth rate decreases continuously as the crack length increases and a crack growth acceleration stage which consists of either a single event of crack growth acceleration leading to crack instability and final failure or repeated events of growth acceleration and retardation followed, again, by crack instability and final failure. No crack arrest was observed under any of the test conditions carried out here.
2. For the same crack length, the crack growth rate decreases as the temperature increases from 24 °C to 500 °C. The further increase in temperature from 500 °C to 650 °C does not bring variations in the fatigue crack growth rate in the crack growth retardation stage, but does cause an earlier transition to the crack growth acceleration stage.
3. The loading frequency has considerable effects on the fatigue crack growth behavior in this composite. The decrease in the frequency results in an increase in the fatigue crack growth rates. The crack growth mechanism in the 10 Hz frequency tests was found to be transgranular dominated by cleavage facets. Isolated colonies of fatigue striations were found on fracture surfaces of some of these tests but did not represent a dominate fracture mode in any of the tests. The damage process associated with lower frequency loadings shows the increasing tendency of intergranular fracture.
4. The average fiber pullout lengths for the high temperature tests are longer than that for the ambient temperature test. For all test conditions, the average fiber pullout length is seen to be proportional to the fatigue crack growth rate, the longest being achieved in the instable

severity of the oxidation damage associated with the lower frequency test condition.

Furthermore, the influence of fiber reinforcement on the crack growth behavior was identified by comparing the da/dN vs ΔK curves of Timetal 21S laminate material (33) and those of the 10 Hz loading frequency shown in Figs. 5-4(a) and 5-4(b). This comparison is illustrated in Fig. 5-13. Here, the crack growth driving force for the laminate material is ΔK_{app} while for the composite is ΔK_{eff} . It is interesting to observe that the slopes of the composite crack growth curves are larger than their counterparts of the laminate material and the crack growth rates of the composite are considerably reduced as compared with those of the laminate material. These two modifications in the crack growth behavior of the composite show that the fiber reinforcements can significantly reduce the effects of both the viscoplastic deformation and the oxidation degradation of the composite's matrix.

5.5 CONCLUSIONS

A series of fatigue crack growth experiments were conducted on specimens made of the continuous fiber reinforced $\sigma 1240$ /Timetal 21S composite employing a combination of temperatures and loading frequencies. Major conclusions of this study can be summarized as follows:

1. Under loading conditions promoting the crack bridging, the fatigue crack growth process exhibits two consecutive stages: a crack growth retardation stage where the crack growth rate decreases continuously as the crack length increases and a crack growth acceleration stage which consists of either a single event of crack growth acceleration leading to crack instability and final failure or repeated events of growth acceleration and retardation followed, again, by crack instability and final failure. No crack arrest was observed under any of the test conditions carried out here.
2. For the same crack length, the crack growth rate decreases as the temperature increases from 24 °C to 500 °C. The further increase in temperature from 500 °C to 650 °C does not bring variations in the fatigue crack growth rate in the crack growth retardation stage, but does cause an earlier transition to the crack growth acceleration stage.
3. The loading frequency has considerable effects on the fatigue crack growth behavior in this composite. The decrease in the frequency results in an increase in the fatigue crack growth rates. The crack growth mechanism in the 10 Hz frequency tests was found to be transgranular dominated by cleavage facets. Isolated colonies of fatigue striations were found on fracture surfaces of some of these tests but did not represent a dominate fracture mode in any of the tests. The damage process associated with lower frequency loadings shows the increasing tendency of intergranular fracture.
4. The average fiber pullout lengths for the high temperature tests are longer than that for the ambient temperature test. For all test conditions, the average fiber pullout length is seen to be proportional to the fatigue crack growth rate, the longest being achieved in the instable

crack growth region.

5. The nominal applied stress intensity factor range, ΔK_{app} , does not represent the crack growth driving force when crack bridging exists. An effective crack tip stress intensity factor range, ΔK_{eff} , equals the difference between ΔK_{app} and the shielding force, ΔK_{sh} . This ΔK_{eff} parameter was calculated based on the knowledge of the maximum bridging traction and the sliding frictional stresses at the fiber/matrix interface along positions on the bridged crack length. Results of correlating the crack growth rate and ΔK_{eff} showed that for the same ΔK_{eff} level, the fatigue crack growth rate increases as the temperature increases or the loading frequency decreases. Furthermore, opposite to the anomalous behavior of da/dN in relation ΔK_{app} , the increase in ΔK_{eff} was found to lead to an increase in the crack growth rate.

5.6 REFERENCES

1. K. S Chan and D. L. Davidson, Fatigue Crack Growth in Fiber-Reinforced Metal-Matrix Composites, in Fatigue of Advanced Materials, eds. by R. O. Ritchie, R. H. Dauskardt and B. N. Cox, Materials and Component Engineering Publications Ltd, P. O. Box 1550, Edgbaston, Birmingham B15 2JZ (UK), 1991, pp. 325-342
2. P. Bowen, A. R. Ibbotson and C. J. Beevers, Characterization of Crack Growth in Continuous Fiber Reinforced Titanium Based Composites Under Cyclic Loading, in Fatigue of Advanced Materials, eds. by R. O. Ritchie, R. H. Dauskardt and B. N. Cox, Materials and Component Engineering Publications Ltd, P. O. Box 1550, Edgbaston, Birmingham B15 2JZ (UK), 1991, pp. 379-393
3. L. Ghosn, P. Kantzos and J. Telesman, Modelling of Crack Bridging in a Unidirectional Metal Matrix Composite, International Journal of Fracture, Vol. 54, 1992, pp. 345-357
4. D. Walls, G. Bao and F. Zok, Fatigue Crack Growth in A Ti/SiC Composite, in Fatigue of Advanced Materials, eds. by R. O. Ritchie, R. H. Dauskardt and B. N. Cox, Materials and Component Engineering Publications Ltd, P. O. Box 1550, Edgbaston, Birmingham B15 2JZ (UK), 1991, pp. 343-356
5. A. R. Ibbotson, P. Bowen and C. J. Beevers, Cyclic Fatigue Resistance of Fiber Reinforced Titanium Metal Matrix Composites at Ambient and Elevated Temperature, 7th Ti Conference, San Diego, July, 1992
6. K. R. Bain and M. L. Gambone, Fatigue Crack Growth of SCS-6/Ti-64 Metal Matrix Composites, in Fundamental Relationships Between Microstructure & Mechanical properties of Metal-Matrix Composites, eds. by P. K. Liaw and M. N. Gungor, The Minerals, Metals & Materials Society, 1990, pp. 459-469

7. H. Ghonem, Y. Wen, D. Zheng, M. Thompson and G. Linsey, Fatigue Crack Growth Characteristics of Ti- β 21S Monolithic Laminate, Studies in Applied Mechanics 34: Damage in Composite Materials, ed. by G. Z. Voyiadjis, Elsevier Science Publishers B. V., New York, 1993, pp. 161-180
8. D. L. Ball, Thermomechanical Fatigue Life Prediction of SCS-6/Beta-21S Composites, Workshop Proceedings of Titanium Matrix Composites, eds. by P. R. Smith and W. C. Revelos, WL-TR-92-4035, 1991, pp. 372-390
9. L. Le Petitcorps, M. Lahaye, R. Pailler and R. Naslain, Modern Boron and SiC CVD Filaments: A Comparative Study, Composites Science and Technology, Vol. 32, 1988, pp. 31-35
10. D. B. Marshall, M. C. Shaw, W. L. Morris and J. Graves, Interfacial Properties and Residual Stresses in Titanium and Aluminide Matrix Composites, Titanium Matrix Components, Workshop Proceedings, eds. by P. R. Smith and W. C. Revelos, Wright-Patterson AFB, Ohio, 1992, WL-TR-92-4035, pp. 329-347
11. R. K. Everett, Diffusion Bonding, Metal Matrix Composites: Processing and Interfaces, eds. by R. K. Everett and R. J. Arsenault, Academic Press, Harcourt Brace Jovanovich, Publishers, Boston, 1991, pp. 17-42
12. Robert E. Reed-Hill, Physical Metallurgy Principles. PWS-KENT Publishing Company, Boston, 1973
13. M. Taya, M. Dunn and H. Lilholt, Long Term Properties of Metal Matrix Composites, Metal Matrix Composites — Processing, Microstructure and Properties, eds. by N. Hansen et al, Risø National Laboratory, Roskilde, denmark, 1991, pp.149-171
14. K. Schulte and K. Minoshima, Mechanisms of Fracture and Failure in Metal Matrix Composites, in Metal Matrix Composites — Processing, Microstructure and Properties, eds. by N. Hansen et al, Risø National Laboratory, Roskilde, denmark, 1991, pp.123-147
15. D. L. Davidson, K. S. Chan, A. McMinn and G. R. Leverant, Micromechanics and Fatigue Crack Growth in an Alumina-Fiber-Reinforced Magnesium Alloy Composite, Metallurgical Transactions, Vol. 20 A, 1989, pp. 2369-2378
16. L. J. Ebert and P. K. Wright, Mechanical Aspects of the Interface, Interfaces in Metal Matrix Composites, ed. by A. G. Metcalfe, Academic Press, New York, 1974, pp. 31-64
17. C. C. Chamis, Mechanics of Load Transfer at the Fiber/Matrix Interface, NASA TN D-6588, 1972
18. R. M. McMeeking and A. G. Evens, Matrix Fatigue Cracking in Fiber Composites,

19. P. Kantzos, J. Telesman and L. Ghosn, Fatigue Crack Growth in a Unidirectional SCS-6/Ti-15-3 Composite, in Composite Materials: Fatigue and Fracture (Third Volume), ASTM SPT 1110, ed. by T. K. O'Brien, American Society for Testing and Materials, Philadelphia, 1991, pp. 711-731
20. D. B. Marshall and B. N. Cox, Tensile Fracture of Brittle Matrix Composites: Influence of Fiber Strength, *Acta Metallurgica et Materialia*, Vol. 35, 1987, pp. 2607-2619
21. D. L. Davidson, The Micromechanics of Fatigue Crack Growth at 25°C in Ti-6Al-4V Reinforced with SCS-6 Fibers, *Metallurgical Transactions*, Vol. 23A, 1992, pp. 865-879
22. J. K. Shang and R. O. Ritchie, Crack Bridging by Uncracked Ligaments during Fatigue-Crack Growth in SiC-Reinforced Aluminum-Alloy Composites, *Metallurgical Transactions*, Vol. 20A, 1989, pp. 897-908
23. D. Zheng and H. Ghonem, The Crack Growth Driving Force in Continuous Fiber Reinforced Titanium Metal Matrix Composites, Unpublished Research.
24. A. Takaku and RGC Arridge, The Effect of Interfacial Radial and Shear Stress on Fiber Pull-Out in Composite Materials, *Journal of Phys. D: Applied Physics*, Vol. 6, 1973, pp. 2038-2047
25. M. C. Watson and T. W. Clyne, The Use of Single Fiber Pushout Testing to Explore Interfacial Mechanics in SiC Monofilament-Reinforced Ti — II. Application of the Test to Composite Material, *Acta Metall. Material*. Vol. 40, 1992, pp.141-148
26. M. C. Watson and T. W. Clyne, The Use of Single Fiber Pushout Testing to Investigate the Interfacial Mechanical Properties of Ti-SiC Monofilament Composites, to be published in *Proceedings of 7th World Titanium Conference*, F. R. Froes ed., ASM, 1992
27. B. N. Cox, D. B. Marshall, W. L. Morris, C. G. Rhodes and M. Shaw, Failure Mechanisms in Titanium Aluminide/SiC Composites, *Materials and Processing — More into the 90's*, eds. by S. Benson, T. Cook, E. Trewin and R. M. Turner, Elsevier Science Publishers B. V., Amsterdam, 1989, pp. 313-320
28. B. N. Cox and D. B. Marshall, Crack Bridging in the Fatigue of Fibrous Composites, *Fatigue & Fracture of Engineering Materials & Structure*, Vol. 14, 1991, pp. 847-861
29. R. A. Naik and W. S. Johnson, Observations of Fatigue Crack Initiation and Damage Growth in Notched Titanium Matrix Composites, in Composite Materials: Fatigue and Fracture (Third Volume), ASTM SPT 1110, ed. by T. K. O'Brien, American Society for Testing and Materials, Philadelphia, 1991, pp. 753-771

30. D. Blatt, An Investigation of the Fatigue Crack Growth Behavior of a Titanium Matrix Composites Under Thermomechanical Loading, Seventh Thermomechanical Fatigue Workshop, NASA Lewis Research Center, Cleveland, Ohio, Dec. 3 and 4, 1992
31. K. W. Buesking, J. L. Young and G. H. Reynolds, Status of Advanced Filament Development for Titanium Alloy and Titanium Intermetallic Matrix Composites, Part 2: Computed Residual Stresses in Gamma TiAl/Advanced Filament Composites, Titanium Matrix Components, Workshop Proceedings, eds. by P. R. Smith and W. C. Revelos, Wright-Patterson AFB, Ohio, 1992, WL-TR-92-4035, pp.42-64
32. T. G. F. Gray, Convenient Closed Form Stress intensity Factors for Common Crack Configurations, International Journal of Fracture, Vol. 13, 1977, pp. 65-75
33. H. Ghonem, Y. Wen, D. Zheng, M. Thompson and G. Linsey, Effects of Temperature and Frequency on Fatigue Crack Growth in Ti- β 21S Monolithic Laminate, Materials Science and Engineering, A161, 1993, pp. 45-53.

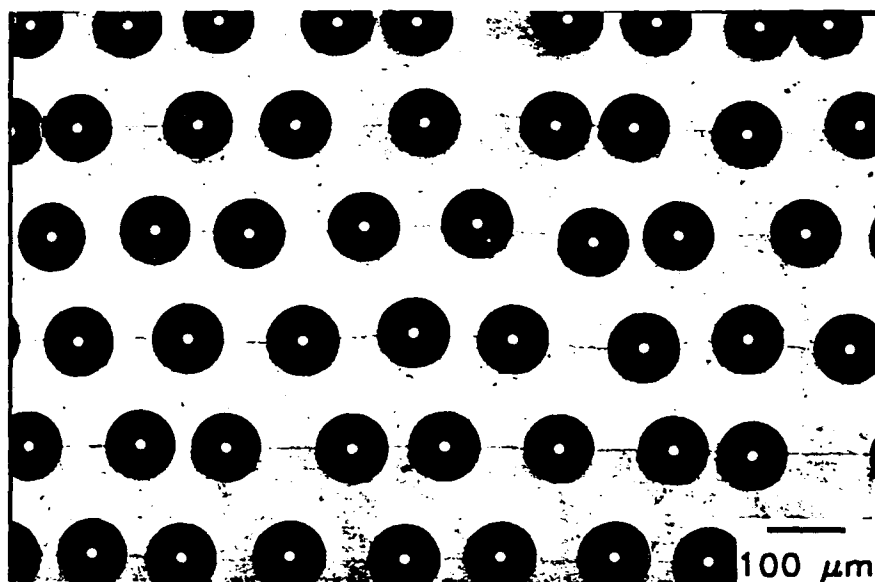


Fig. 5-1(a) A polished and etched cross section of the as-fabricated $\sigma 1240/\text{Timetal@21S}$ composite specimen(observe the hexagonal fiber arrangements)

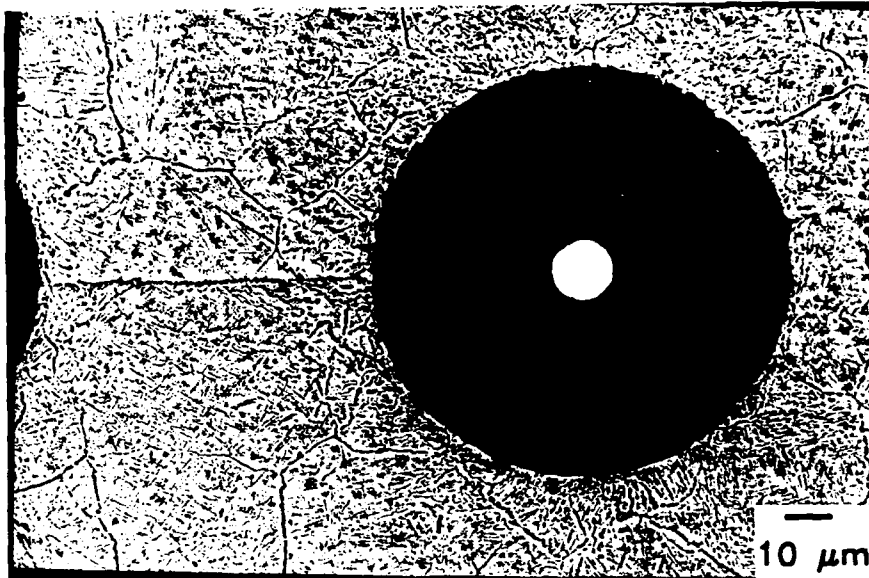
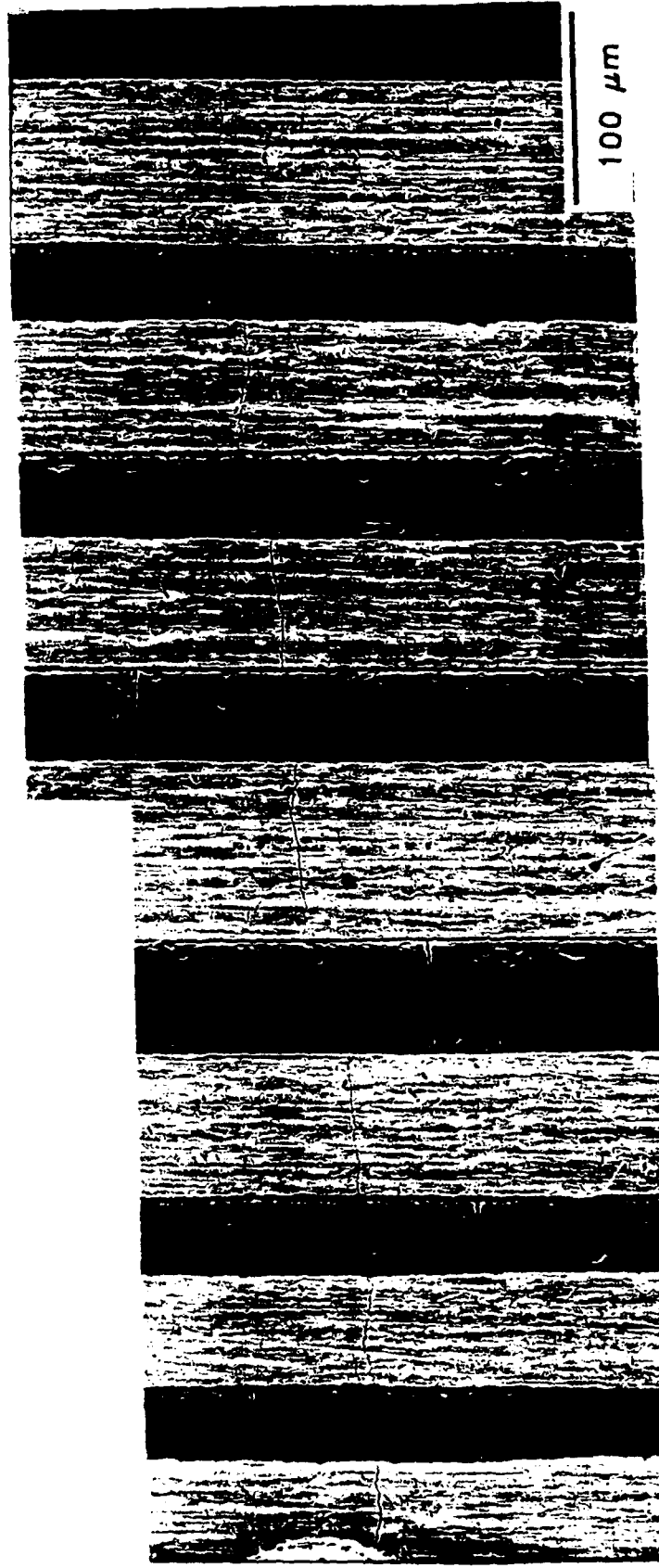


Fig. 5-1(b) Microstructure details of the Timetal@21S matrix in the fiber surrounding region. Note the fine grains around the area of the fiber/matrix interface.

Crack Growth Direction



100 μm

Notch Tip



Fig. 5-2(a) Polished surfaces of test specimens showing crack bridging and positions of fiber fracture for 24 °C/10 Hz test stopped after the crack growth retardation stage.

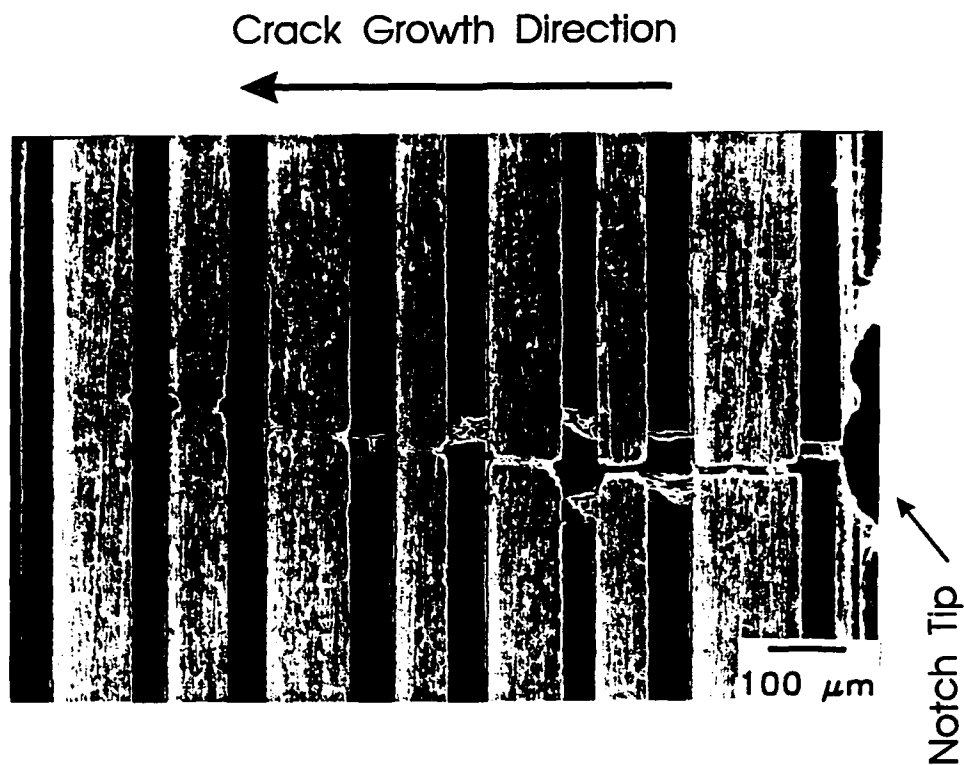


Fig. 5-2(b) Polished surfaces of test specimens showing crack bridging and positions of fiber fracture for 650 °C/ 0.1 Hz test stopped at the instable fracture stage. This figure shows the fracture of all bridged fibers.

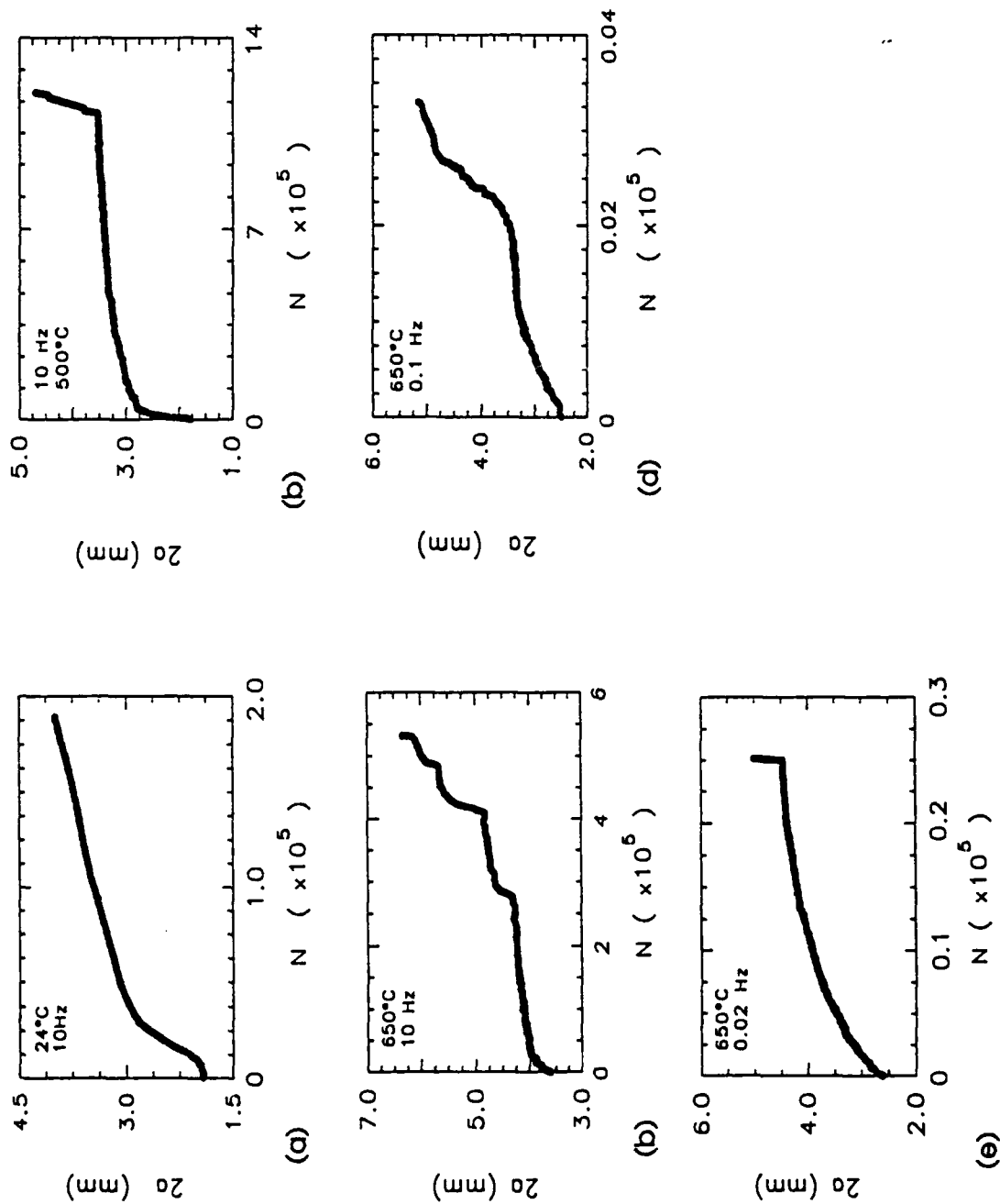


Fig. 5-3 Variation of the crack length, $2a$, with the number of fatigue cycles, N , for different test conditions. (a) 24 °C/10 Hz; (b) 500 °C/10 Hz; (c) 650 °C/0.1 Hz; (d) 650 °C/0.02 Hz; (e) 650 °C/0.02 Hz.

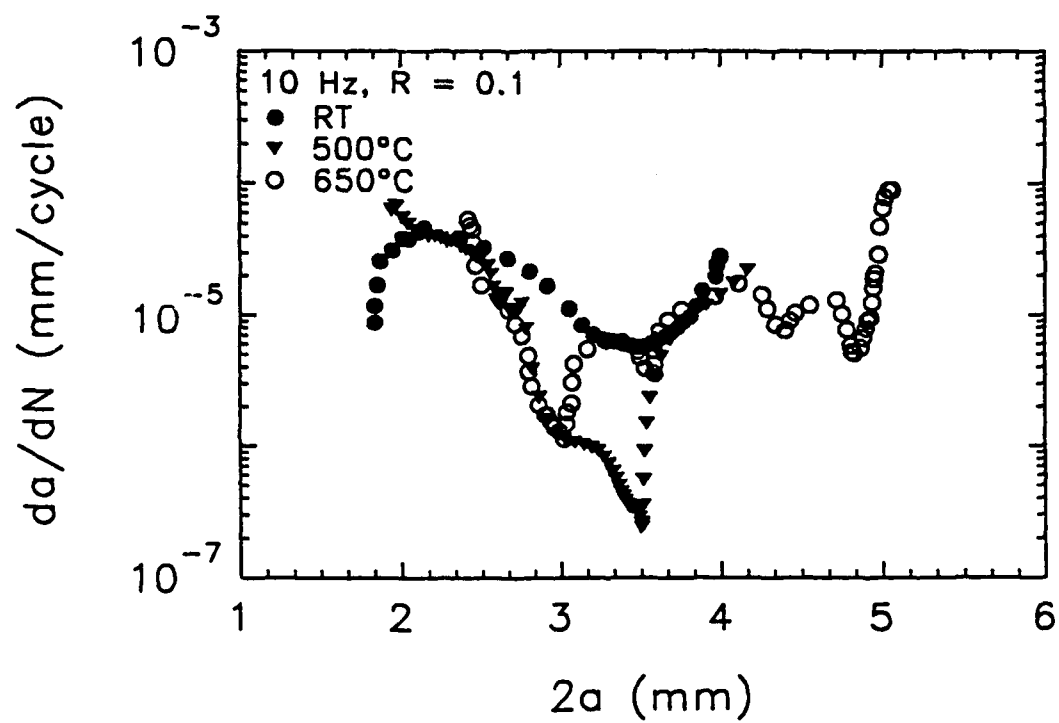


Fig. 5-4(a) Fatigue crack growth rate, da/dN , versus crack length, $2a$, for different test temperatures.

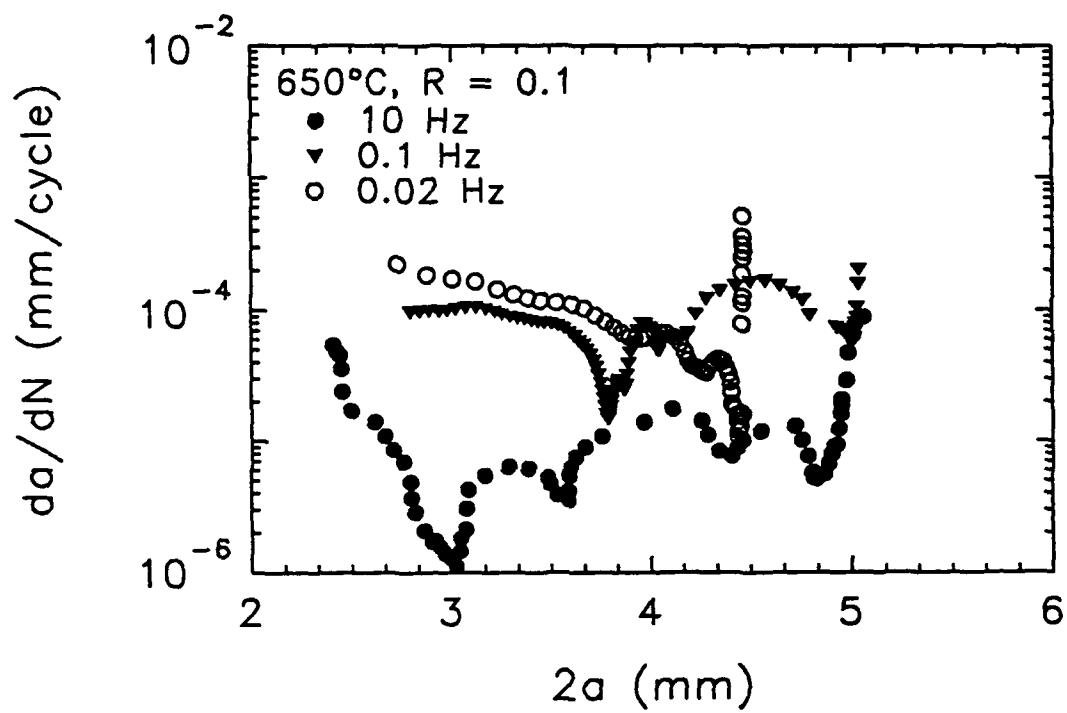


Fig. 5-4(b) Fatigue crack growth rate, da/dN , versus crack length, $2a$, for different loading frequencies.

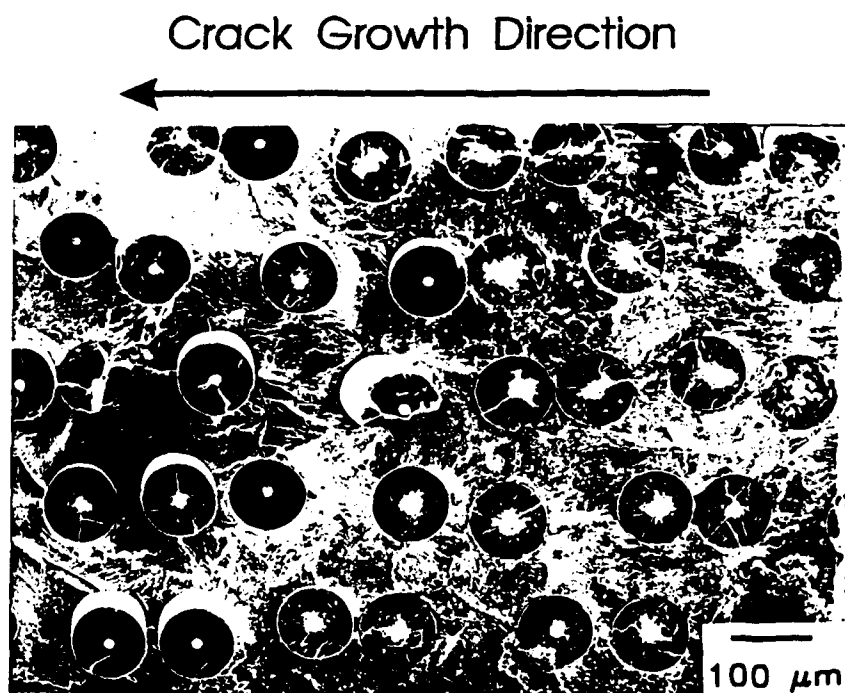


Fig. 5-5 General view of the fracture surface obtained from 650 °C/10 Hz test showing the crack retardation stage and the crack growth acceleration stage.

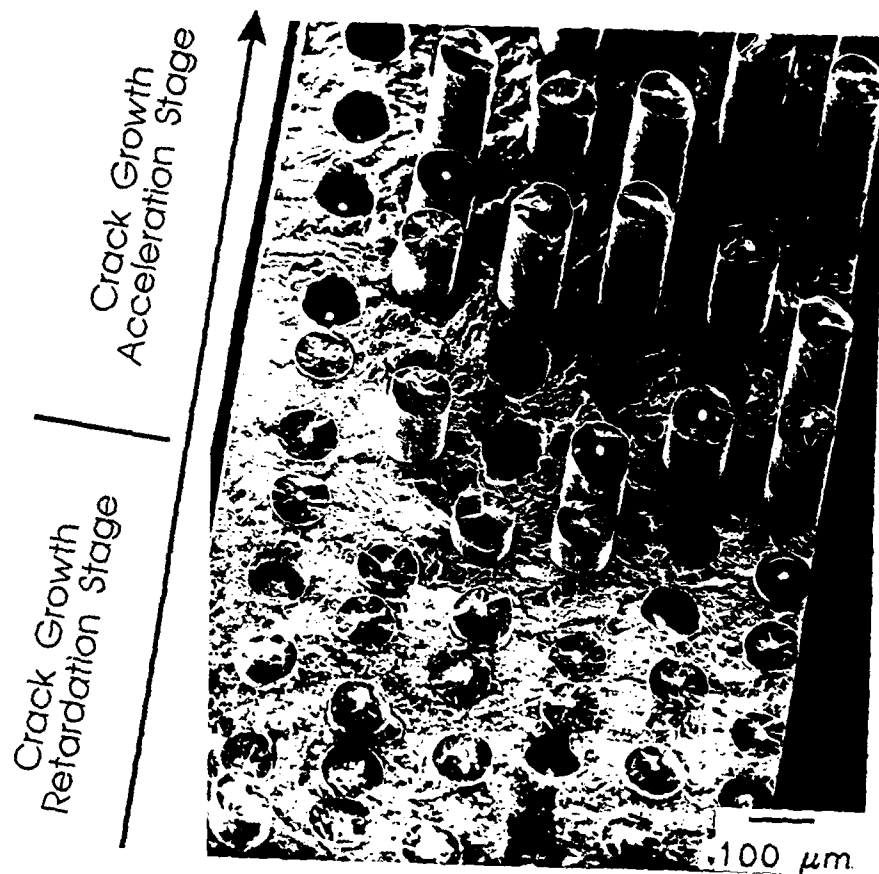


Fig. 5-6(a) Severe fiber core damage in the crack growth retardation stage at low magnification (650 °C/10 Hz).

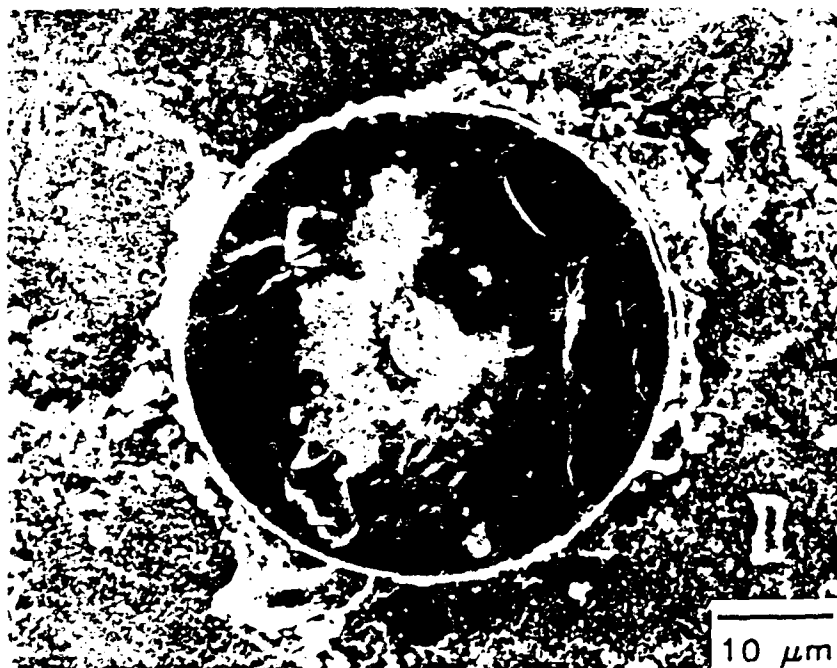


Fig. 5-6(b) Severe fiber core damage in the crack growth retardation stage at high magnification (650 °C/ 0.1 Hz).

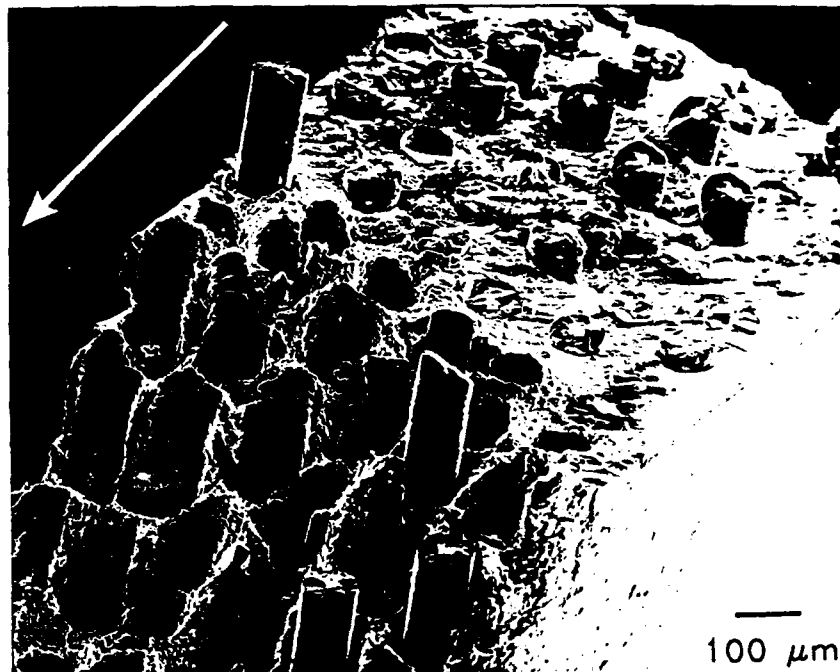


Fig. 5-7(a) View of the instable fracture region at low magnification (650 °C/0.1 Hz, arrow indicates the crack growth direction and the lower left part of the fracture surface is the instable fracture region.

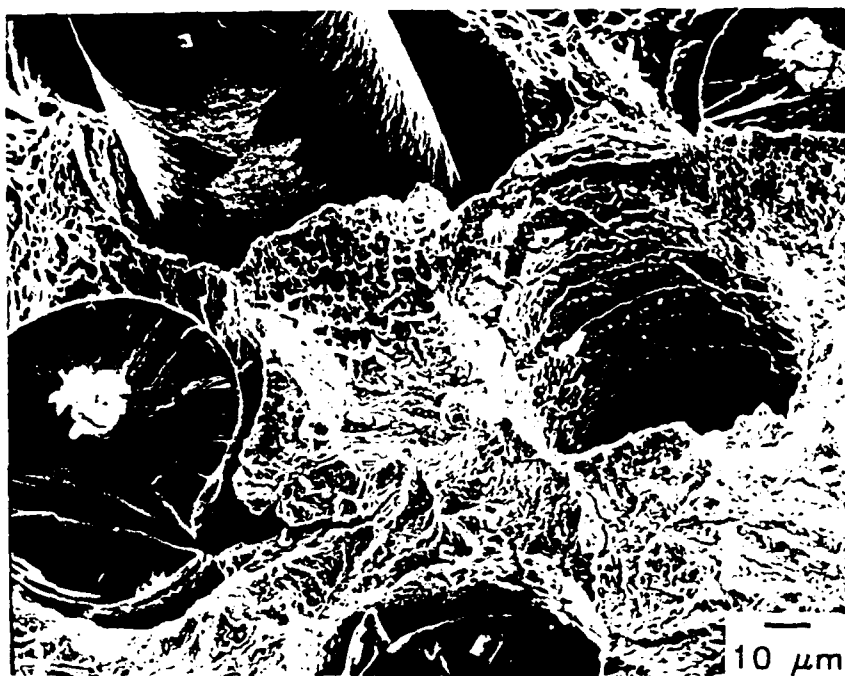


Fig. 5-7(b) View of the instable fracture region at high magnification (650 °C/0.02 Hz), observe the degree of the matrix viscoplastic flow surrounding the pullout fibers.

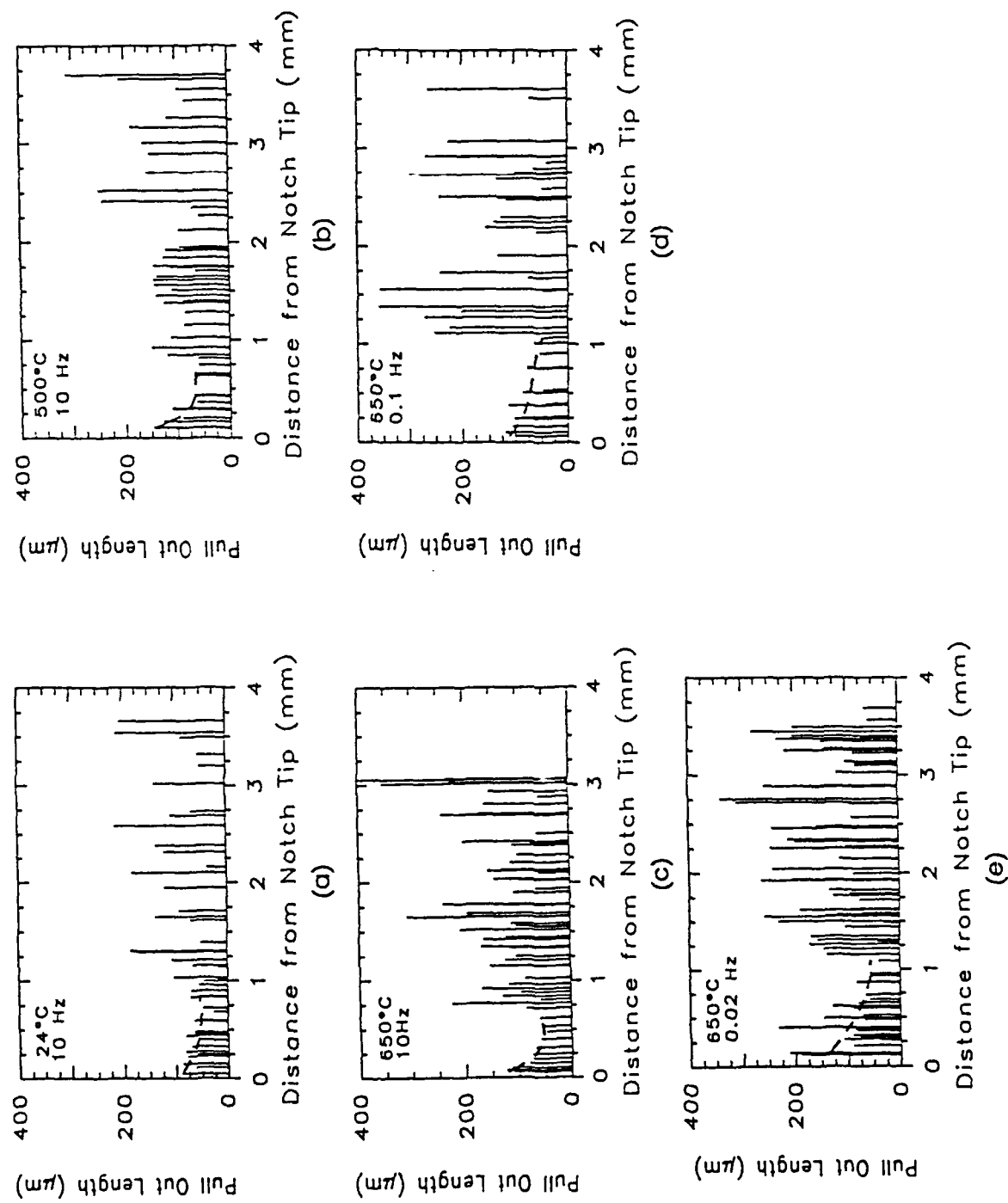


Fig. 5-8 Distributions of the fiber pullout length for various test conditions. The dashed line is a regression fitting of data corresponding to be the crack growth retardation stage. (a) 24 °C/10 Hz; (b) 500 °C/10 Hz; (c) 650°C/0.02 Hz; (d) 650 °C/0.1 Hz; (e) 650 °C/10 Hz.

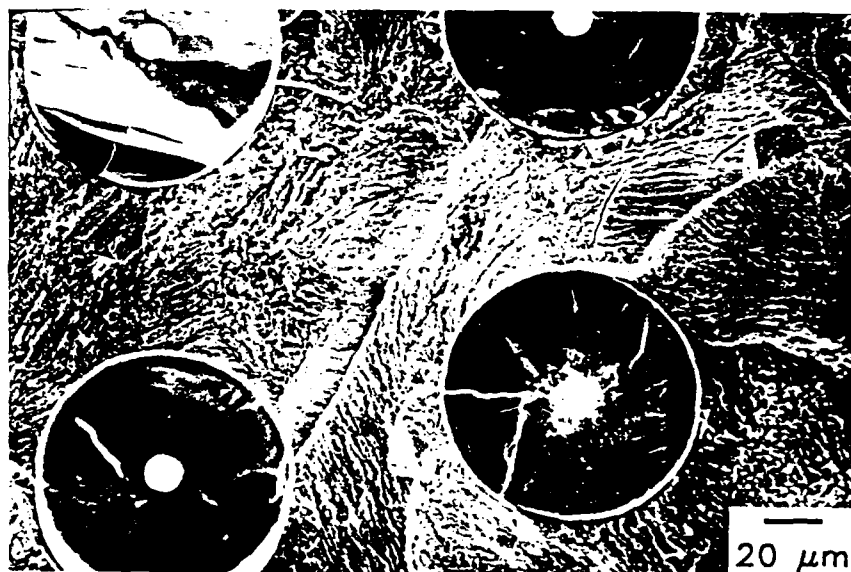


Fig. 5-9(a) Typical matrix transgranular fracture features due to the high frequency tests is transgranular.

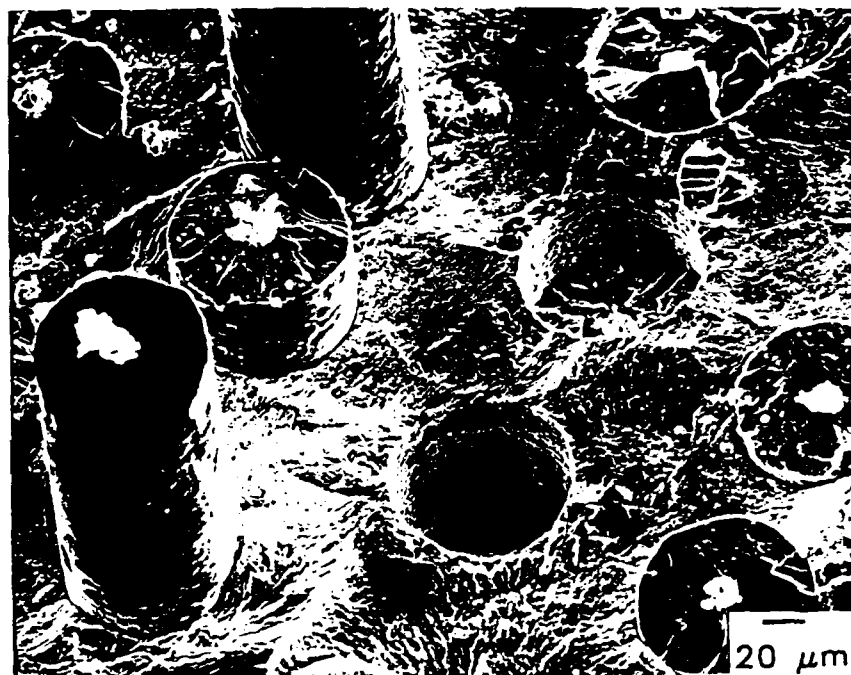


Fig. 5-9(b) Typical matrix features due to the low frequency loadings (650 °C/0.02 Hz). The fracture mode is a mixture of intergranular and transgranular.

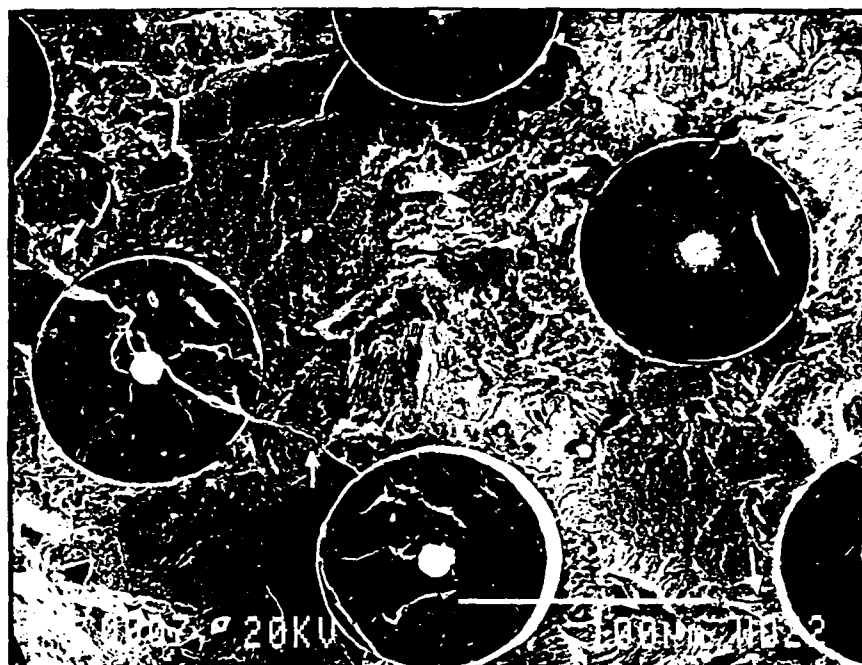


Fig. 5-10 Typical radial cracks in the interfacial region and severe oxidation damage of the fiber coating layers in the low frequency tests (650 °C/0.02 Hz).

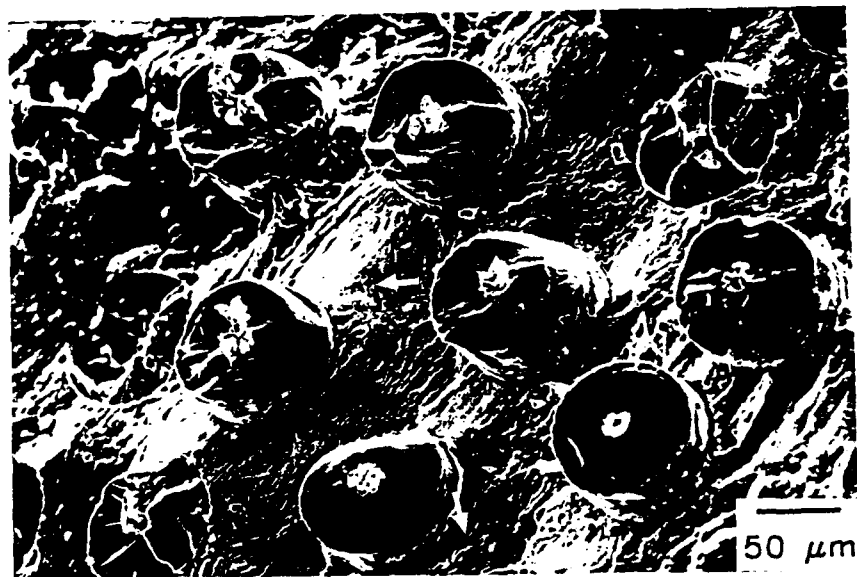


Fig. 5-11 Local viscoplastic flow around fiber regions indicating matrix stress relaxation.

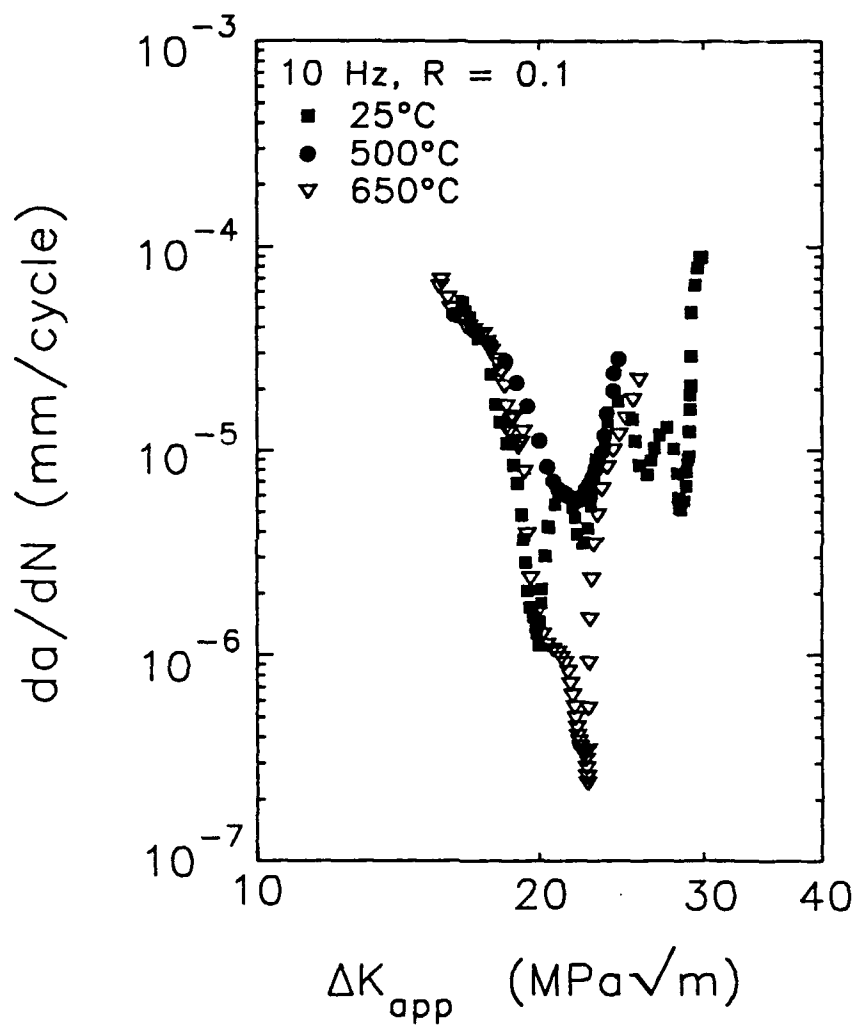


Fig. 5-12(a) Fatigue crack growth rate, da/dN , in the composite versus the nominal applied stress intensity factor range, ΔK_{app} , for various temperatures.

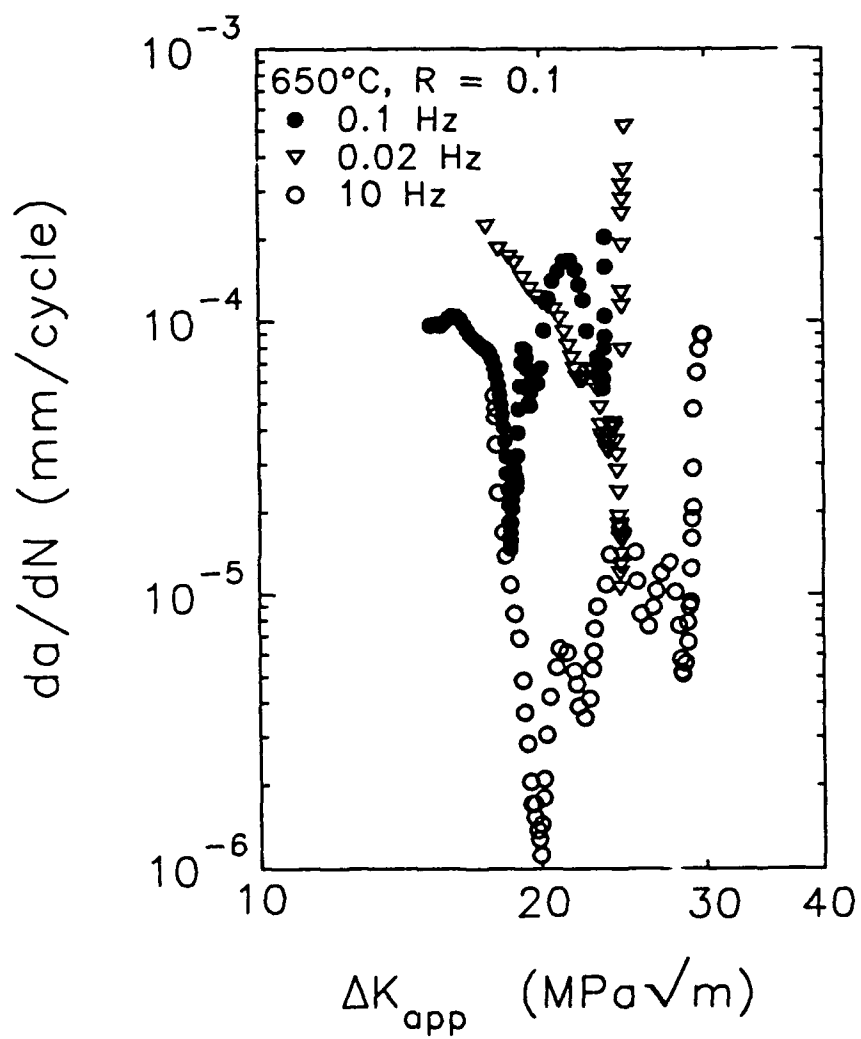


Fig. 5-12(b) Fatigue crack growth rate, da/dN , in the composite versus the nominal applied stress intensity factor range, ΔK_{app} , for various loading frequencies.

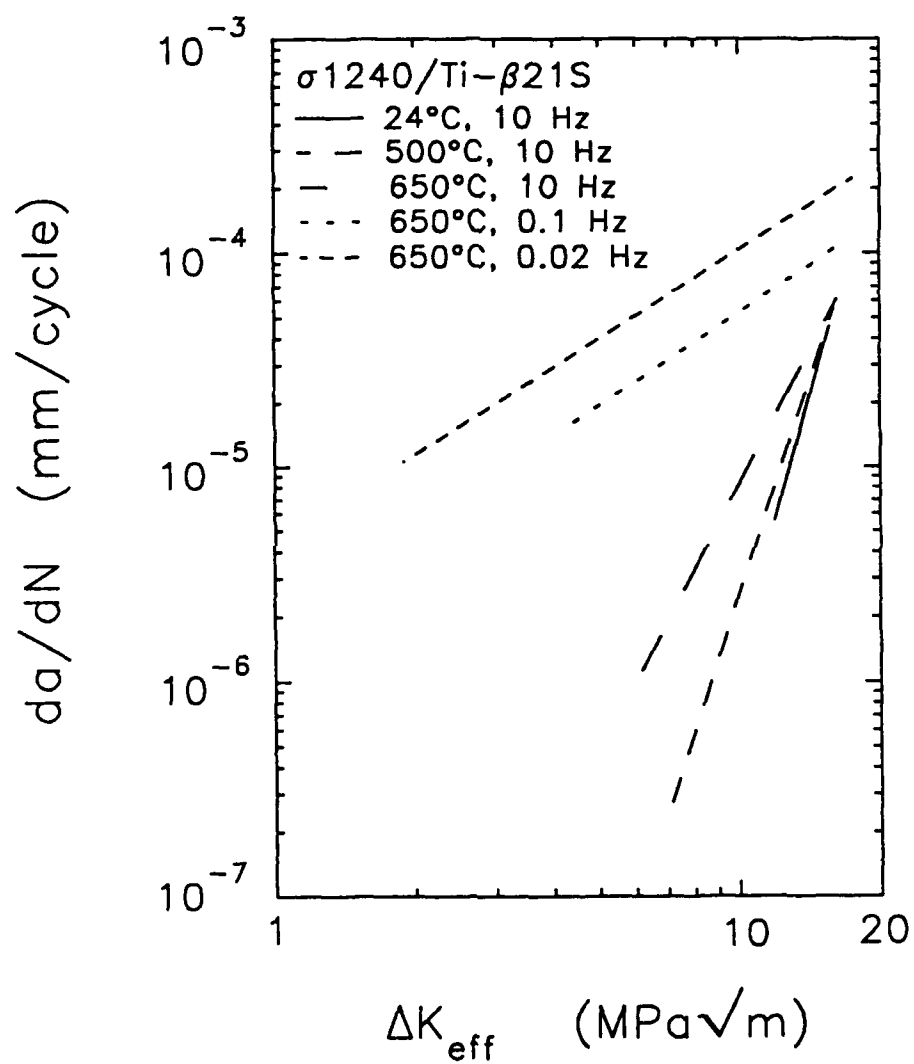


Fig. 5-12(c) Fatigue crack growth rate, da/dN , in the composite versus the effective applied stress intensity factor range, ΔK_{eff} , for the crack growth retardation stage only.

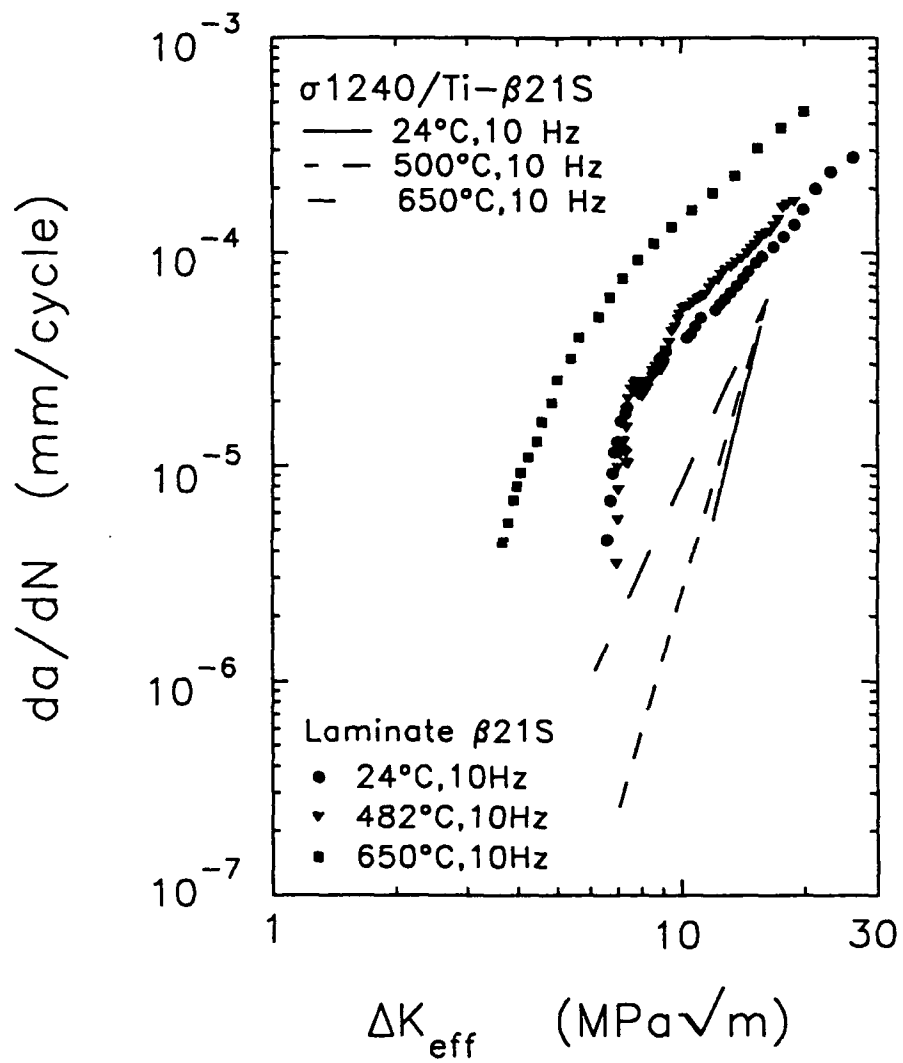


Fig. 5-13 Comparison between the fatigue crack growth rates in the composite and the laminate matrix material.